UNIVERSITY OF CALIFORNIA, SAN DIEGO

Beyond the Scalar Higgs, in Lattice Quantum Field Theory

A dissertation submitted in partial satisfaction of the
requirements for the degree
Doctor of Philosophy

in

Physics with Specialization in Computational Science

by

Christopher Robert Schroeder

Committee in charge:

Professor Julius Kuti, Chair
Professor Randolph E. Bank
Professor Benjamin Grinstein
Professor Michael Holst
Professor Vivek Sharma

2009

The dissertation of Christopher Robert Schroeder is approved, and it is acceptable in quality and form for publication on microfilm and electronically:

_____

_____

_____

_____

_____
Chair

University of California, San Diego

2009

TABLE OF CONTENTS

LIST OF FIGURES

LIST OF TABLES

ACKNOWLEDGEMENTS

First and foremost I acknowledge Professor Julius Kuti for leading the way as my research adviser, chairing my committee, and providing financial support through the grant DOE-FG03-97ER40546 on several occasions. I also acknowledge our collaborators for their essential contributions to my studies and to the outcomes of our projects.

I acknowledge the time which the members of my committee have generously given to assist in my advancement and graduation as well as the faculty, staff, and students of the UCSD Department of Physics and Office of Graduate Studies for facilitating my studies.

Last but certainly not least, I acknowledge the Department of Energy Computational Science Graduate Fellowship and the Krell Institue which has administered it for tremendous financial and intellectual support.

Chapter 2, in full, is a reprint of the material as it appears in Proceedings of Science: Lattice 2007. Zoltan Fodor, Kieran Holland, Julius Kuti, Daniel Nogradi and Chris Schroeder, PoS LATTICE2007, 056, 2007. The dissertation author was a principal investigator and co-author of this paper.

Chapter 3, in full, is a reprint of the material as it appears in Proceedings of Science: Lattice 2008. Zoltan Fodor, Kieran Holland, Julius Kuti, Daniel Nogradi, and Chris Schroeder, PoS LATTICE2008, 066, 2008. The dissertation author was a principal investigator and co-author of this paper.

Chapter 4, in full, is currently being prepared for submission for publication in Proceedings of Science: Lattice 2009. The dissertation author was a principal investigator and co-author of this paper.

VITA

2009	Ph. D. in Physics, University of California, San Diego
2009	Graduate Research Assistant, University of California, San Diego
2005-2009	DOE Computational Science Graduate Fellow, University of California, San Diego
2004-2005	Graduate Teaching Assistant, University of California, San Diego
2003-2004	Graduate Research Fellow, University of California, San Diego
2002	B. S. in Physics, Carnegie Mellon University

PUBLICATIONS

Z. Fodor, K. Holland, J. Kuti, D. Nogradi and C. Schroeder, "Chiral symmetry breaking in nearly conformal gauge theories", in preparation [arXiv:0911.2463].

Z. Fodor, K. Holland, J. Kuti, D. Nogradi and C. Schroeder, "Calculating the running coupling in strong electroweak models", PoS **LATTICE2009**, 058 (2009).

Z. Fodor, K. Holland, J. Kuti, D. Nogradi and C. Schroeder, "Chiral properties of SU(3) sextet fermions", in preparation [arXiv:0908.2466].

Z. Fodor, K. Holland, J. Kuti, D. Nogradi and C. Schroeder, "Nearly conformal gauge theories in finite volume", Phys. Lett. B **681**, 353 (2009).

Z. Fodor, K. Holland, J. Kuti, D. Nogradi and C. Schroeder, "Topology and higher dimensional representations", JHEP **0908**, 084 (2009).

Z. Fodor, K. Holland, J. Kuti, D. Nogradi and C. Schroeder, "Probing technicolor theories with staggered fermions", PoS **LATTICE2008**, 066 (2008).

Z. Fodor, K. Holland, J. Kuti, D. Nogradi and C. Schroeder, "Nearly conformal electroweak sector with chiral fermions", PoS **LATTICE2008**, 058 (2008).

Z. Fodor, K. Holland, J. Kuti, D. Nogradi and C. Schroeder, "New Higgs physics from the lattice.", PoS **LATTICE2007**, 056 (2007).

ABSTRACT OF THE DISSERTATION

Beyond the Scalar Higgs, in Lattice Quantum Field Theory

by

Christopher Robert Schroeder

Doctor of Philosophy in Physics with Specialization in Computational Science

University of California, San Diego, 2009

Professor Julius Kuti, Chair

Since the development of the standard model over 40 years ago, one of the chief endeavors of particle physics has been to understand the Higgs sector of the theory. Still experimentally undetected despite great efforts, the Higgs sector remains a mystery, and ideas of what lies beyond have flourished. The aim of the research described here has been to explore non-perturbatively ideas of greatest interest which are within reach of current non-perturbative methods and resources and beyond the current reach of rigorous perturbative investigation. The first is the relationship between the Higgs boson mass and the energy scale of new phenomena expected to appear at higher energies due to a peculiar property of Higgs models known as triviality. The second is nearly conformal gauge theory and its role in the possible explanation of the Higgs as a composite state, again linking to new phenomena at higher energies, namely extended technicolor. The imminent advent of the Large Hadron Collider makes the discovery and understanding of new physics at higher energies a tangible possibility. In the likely event that new phenomena are strongly coupled, non-perturbative methods will be crucial to interpreting the results and producing the next generation of theories.

Chapter 1

The Higgs Mechanism

The unified theory of the electromagnetic and weak interactions is one of the great achievements of physics. The Higgs mechanism of spontaneous symmetry breaking is a core component. The purpose of this chapter is to introduce triviality and nearly conformal gauge theory in the framework of Higgs physics. Much of this chapter is based on Peskin and Schroeder's *An Introduction to Quantum Field Theory* [1], Novaes' *Standard Model: An Introduction* [2] and Lane's *Two Lectures on Technicolor* [3].

1.1 Gauge Boson Masses

Early electroweak physics experiments demanded that the standard model of electroweak interactions possess both a high-energy phase with an unbroken gauge symmetry $SU(2)_L \otimes U(1)_Y$ and a low-energy phase where this symmetry is spontaneously broken down to the $U(1)$ of electromagnetism and the weak interaction is mediated by massive gauge bosons. Complicating matters (in hindsight, perhaps, simplifying them), weak gauge boson masses are prohibited in the high-energy phase since they are in direct conflict with unbroken gauge symmetry. The solution found was, essentially, to invent terms which would function as mass terms at low energies but evaporate in the high-energy phase. This feat was accomplished by the introduction of a new field endowed with the novel feature of a symmetric potential with non-zero minima, i.e. a vacuum expectation value (or vev). Thus

the phenomenally successful standard model of electroweak interactions was developed, in large part, with the Higgs mechanism at its core. Observation further demanded that the new field be a scalar in the spinor representation of $SU(2)_L$ and assigned a charge of $+1/2$ under $U(1)_Y$; hence its covariant derivative

$$D_\mu \phi = \left(\partial_\mu - igA^a_\mu \tau^a - i\frac{1}{2} g' B_\mu \right) \phi \tag{1.1}$$

with scalar field ϕ, couplings g and g', $SU(2)_L$ gauge boson A^a_μ, and $U(1)_Y$ gauge boson B_μ. If the potential for the scalar is constructed to yield the vev

$$\langle \phi \rangle = \frac{1}{\sqrt{2}} \begin{pmatrix} 0 \\ v \end{pmatrix}, \tag{1.2}$$

then the term $(D_\mu \phi)^2$ yields acceptable mass terms for the gauge bosons

$$\frac{1}{2} \begin{pmatrix} 0 & v \end{pmatrix} \left(gA^a_\mu \tau^a + \frac{1}{2} g' B_\mu \right) \left(gA^{b\mu} \tau^b + \frac{1}{2} g' B^\mu \right) \begin{pmatrix} 0 \\ v \end{pmatrix}. \tag{1.3}$$

Substituting $\tau^a = \sigma^a/2$ and writing out the matrix product reveals

$$\frac{1}{2} \frac{g^2 v^2}{4} \left((A^1_\mu)^2 + (A^2_\mu)^2 \right) + \frac{1}{2} \frac{v^2}{4} \left(gA^3_\mu - g' B_\mu \right)^2. \tag{1.4}$$

Thus, in the broken phase of the theory, there are three massive vector bosons,

$$W^\pm_\mu = \frac{1}{\sqrt{2}} (A^1_\mu \mp iA^2_\mu), \qquad Z^0_\mu = \frac{1}{\sqrt{g^2 + g'^2}} (gA^3_\mu - g' B_\mu) \tag{1.5}$$

with masses $m_W = gv/2$ and $m_Z = \sqrt{g^2 + g'^2} v/2$, along with the massless electromagnetic vector potential,

$$A_\mu = \frac{1}{\sqrt{g^2 + g'^2}} (g' A^3_\mu + gB_\mu). \tag{1.6}$$

1.2 Fermion masses

Of course, the standard model must also properly describe fermions. The covariant derivatives containing the fermion-gauge couplings must take the form

$$D_\mu = \partial_\mu - igA^a_\mu T^a - ig' Y B_\mu \tag{1.7}$$

for $SU(2)$ representation corresponding to T and $U(1)$ charge Y. In terms of the vector boson fields, this is

$$\begin{aligned} D_\mu &= \partial_\mu - i\frac{g}{\sqrt{2}}\left(W_\mu^+ T^+ + W_\mu^- T^-\right) - i\frac{1}{\sqrt{g^2+g'^2}} Z_\mu (g^2 T^3 - g'^2 Y) \\ &\quad -i\frac{gg'}{\sqrt{g^2+g'^2}} A_\mu (T^3 + Y), \end{aligned} \tag{1.8}$$

with $T^\pm = T^1 \pm iT^2$. The identification of the electromagnetic interaction is completed using the Gell-Mann–Nishijima relation [4],

$$Q = T^3 + Y, \tag{1.9}$$

and defining the electron charge as

$$e = \frac{gg'}{\sqrt{g^2+g'^2}}. \tag{1.10}$$

It is conventional to introduce the weak mixing angle defined by

$$\sin\theta_w = \frac{g'}{\sqrt{g^2+g'^2}}; \tag{1.11}$$

the covariant derivative can then be written

$$D_\mu = \partial_\mu - i\frac{g}{\sqrt{2}}\left(W_\mu^+ T^+ + W_\mu^- T^-\right) - i\frac{g}{\cos\theta_w} Z_\mu (T^3 - \sin^2\theta_w Q) - ieA_\mu Q \tag{1.12}$$

It is important to note that, since $g = e/\sin\theta_w$ and $m_Z = m_W/\cos\theta_w$, only three independent parameters remain, m_W, θ_w, and e. Experimentally, the W boson couples only to left-handed states, so right-handed fermions must be singlets under $SU(2)$ while left-handed fermions must be doublets. Hypercharges are then uniquely determined from corresponding electric charges.

Like the masses for the gauge bosons, masses for the fermions are prohibited in the electroweak symmetric phase of the theory because explicit mass terms break the symmetry. Serendipitously, the Higgs field comes to the rescue again. For example, the electron mass term can be generated as follows. The term

$$\Delta\mathcal{L}_e = -\lambda_e \bar{E}_L \cdot \phi e_R + h.c. \tag{1.13}$$

with left-handed $SU(2)$ doublet E_L, right-handed singlet e_R, and Yukawa coupling λ_e (*h.c.* is short for hermitian conjugate), is gauge invariant as long as the Higgs field is a neutral $SU(2)$ spinor. Inserting the vev yields the electron mass term,

$$\Delta\mathcal{L}_e = -\frac{1}{\sqrt{2}}\lambda_e v \bar{e}_L e_R + h.c., \tag{1.14}$$

with $m_e = \lambda_e v/\sqrt{2}$. Masses for the other fermions can be generated similarly. A key point is that while these Yukawa couplings allow for the large range in lepton masses, from the electron at 0.511 MeV to the top quark at 173 GeV, the theory provides no rationale for this. It is also noteworthy that the quark mass eigenstates are related to their gauge eigenstates through the non-trivial Cabibbo-Kobayashi-Maskawa (CKM) matrix, which allows for weak-interaction transitions between quark generations.

1.3 The Higgs sector

Certainly, introducing the Higgs field and coupling it to the gauge bosons and fermions has consequences beyond the desired mass terms. These consequences comprise the Higgs sector. Subsection 1.3.1 is a brief description of the Higgs sector for a fundamental scalar Higgs, while subsection 1.3.2 introduces another possibility, that the Higgs is a composite particle produced by new physics referred to generally as technicolor.

1.3.1 The Elementary Higgs Model

The standard choice for the Higgs Lagrangian is

$$\mathcal{L} = |D_\mu \phi|^2 + \mu^2 \phi^\dagger \phi - \lambda \left(\phi^\dagger \phi\right)^2 \tag{1.15}$$

with vev

$$v = \sqrt{\frac{\mu^2}{\lambda}}. \tag{1.16}$$

Expanding ϕ around the vev as

$$\phi(x) = \frac{1}{\sqrt{2}} \begin{pmatrix} 0 \\ v + h(x) \end{pmatrix} \tag{1.17}$$

yields the potential energy and interactions of the Higgs boson, h. The potential takes the form

$$\mathcal{L}_V = -\mu^2 h^2 - \lambda v h^3 - \frac{1}{4}\lambda h^4, \tag{1.18}$$

i.e., a scalar particle with a quartic potential and a mass

$$m_h = \sqrt{2}\mu = \sqrt{2\lambda}v. \tag{1.19}$$

Expanding the covariant derivative yields the kinetic term for the Higgs,

$$\frac{1}{2}(\partial_\mu h)^2, \tag{1.20}$$

as well as couplings to the weak bosons,

$$\left(m_W^2 W^{\mu+} W_\mu^- + \frac{1}{2} m_Z^2 Z^\mu Z_\mu\right)\left(1 + \frac{h}{v}\right)^2. \tag{1.21}$$

Likewise, the terms used to generate fermion masses produce Higgs-fermion interactions such as

$$-m_e \bar{E}_L \left(1 + \frac{h}{v}\right) e_R. \tag{1.22}$$

A fundamental scalar is only one possibility for constructing the Higgs Mechanism. While significant experimental evidence for the electroweak standard model has been found, the Higgs sector remains largely unexplored. Evidence for or against the fundamental scalar model has been difficult to obtain for decades. In the meantime, several theoretical concerns with this model have been raised.

The description of electroweak symmetry breaking relies on input parameters and does not address dynamics. The model provides no reason for electroweak symmetry breaking and no explanation for the observed energy scale of 1 TeV or the vev of 246 GeV. There is a striking hierarchy between the electroweak scale and the Grand Unified Theory (GUT) scale of 10^{16} GeV, where the strong and electroweak interactions appear to converge through renormalization. In elementary Higgs models, the hierarchy is put in by hand, with no explanation; but that is not all. The Higgs mass is quadratically unstable against radiative corrections [5]; therefore a renormalized Higgs mass on the electroweak scale of order 1 TeV would require the mass on the more natural GUT scale to be tuned to a precision of

order 10^{-32}. That is, the separation of scales inherent in elementary scalar models is not only unexplained but also unnatural.

There is no explanation of the large range of fermion masses or flavor. In addition to the hierarchy of scales of gauge symmetry breaking, there is a substantial hierarchy of scales present in the fermion masses, or equivalently in the Yukawa couplings. Again, in elementary Higgs models, this scale separation is dialed in without rationale. Nor is any meaning given to flavor – from the number of quark and lepton generations to the observed patterns of flavor changing; it, too, is simply an input. Flavor-symmetry breaking Yukawa couplings of Higgs bosons to fermions are arbitrary free parameters.

Elementary Higgs models are trivial. In such a model, with an energy cutoff Λ , the self-coupling of the Higgs boson at an energy scale μ is given, to a good approximation, by

$$\lambda(\mu) \approx \frac{\lambda(\Lambda)}{1 + \frac{24}{16\pi^2}\lambda(\Lambda)\log\left(\frac{\Lambda}{\mu}\right)}. \tag{1.23}$$

The coupling vanishes for all μ as the cutoff Λ is removed to infinity; that is, the renormalized theory is free and physically meaningless. Yukawa and gauge couplings are ignored here but are not expected to alter the result qualitatively. The standard interpretation of triviality is that the model is merely an effective approximation at low energies, and an underlying, non-trivial model will distinguish itself at higher energies. In this interpretation, the Higgs mass, vev, and coupling are constrained by the scale at which the low-energy approximation breaks down. Exploration of these so-called triviality bounds is the subject of Chapter 2.

1.3.2 Technicolor

In response to these concerns, a dynamical approach to electroweak symmetry breaking, technicolor, was introduced and extended to include flavor symmetry breaking. The motivating premise is that every fundamental energy scale ought to have a dynamical origin. Just as renormalization of the strong coupling in QCD triggers chiral symmetry breaking at the scale $\Lambda_{QCD} = 200$ MeV, a new strong interaction, technicolor, could give rise dynamically to the electroweak scale. In

technicolor, there is a new set of fermions, techniquarks, belonging to a complex representation of a new gauge group – technicolor, $SU(N_{TC})$ – whose coupling α_{TC} becomes strong at a scale Λ_{TC} of order 100 GeV, in close analogy to QCD. When α_{TC} becomes strong, the techniquark chiral symmetry is spontaneously broken, Goldstone bosons and a techniquark condensate appear, and the Higgs mechanism is enacted if the proper couplings exist between techniquarks and the electroweak gauge fields. In particular, the crucial ratio of $M_W/M_Z = \cos\theta_w$ is produced, without a fundamental scalar.

Since technicolor is an asymptotically free theory like QCD, it immediately eliminates the concerns over naturalness, hierarchy, and triviality. The ground-state technihadron masses are naturally of order Λ_{TC}, and there are no large mass renormalizations and hence no need for fine tuning. Exponential separation of scales is inherent, since Λ_{TC} is produced from the logarithmic running of α_{TC}, and asymptotically free theories are known to be non-trivial. To quote Lane, "No other scenario for the physics of the TeV scale solves these problems so neatly. Period." [3]. On the other hand, basic technicolor fails to address the questions of flavor physics, neglects to generate quark and lepton masses, and produces unnecessary additional Goldstone bosons – technipions, π_T – which must be heavy enough to have thus far escaped detection. Extended technicolor (ETC) was developed to address all of these issues [6].

In extended technicolor, ordinary $SU(3)$ color and $SU(N_{TC})$ technicolor are embedded into the ETC gauge group, G_{ETC}, along with flavor symmetries. By design, flavor gauge symmetries are broken, leaving color and technicolor intact, at an energy scale well above the TC scale of 0.1-1.0 TeV,

$$\Lambda_{ETC} \sim M_{ETC}/g_{ETC} \gg \Lambda_{TC} \approx \frac{1}{2}\,\text{TeV}. \tag{1.24}$$

M_{ETC} is the mass scale of the flavor gauge boson and g_{ETC} is the ETC gauge coupling. All global flavor symmetries must be broken explicitly to avoid producing any light pseudo-Goldstone particles. Coupling quarks and leptons to techniquarks gives rise to mass terms that, at the scale M_{ETC}, take the form

$$m_q(M_{ETC}) \sim m_l(M_{ETC}) \sim \frac{g_{ETC}^2}{M_{ETC}^2}\langle \bar{T}_L T_R \rangle_{ETC}. \tag{1.25}$$

The bilinear condensate at this scale is related through renormalization to the condensate at the TC scale by

$$\langle \bar{T}_L T_R \rangle_{ETC} = \langle \bar{T}_L T_R \rangle_{TC} \exp\left(\int_{\Lambda_{TC}}^{M_{ETC}} \frac{d\mu}{\mu} \gamma_m(\mu) \right). \tag{1.26}$$

An estimate for the latter is obtained by scaling up QCD:

$$\langle \bar{T}_L T_R \rangle_{TC} \approx 4\pi F_T^3, \tag{1.27}$$

while the anomalous dimension, γ_m, is calculable in perturbation theory,

$$\gamma_m(\mu) = \frac{3C_2(R)}{2\pi} \alpha_{TC}(\mu) + O(\alpha_{TC}^2), \tag{1.28}$$

where $C_2(R)$ is the quadratic Casimir of the techniquark representation R. For the fundamental representation, $C_2(N_{TC}) = (N_{TC}^2 - 1)/2N_{TC}$. Technipion masses of the form

$$M_{\pi_T}^2(M_{ETC}) \sim \frac{1}{F_T^2} \frac{g_{ETC}^2}{M_{ETC}^2} \langle \bar{T}_L T_R \bar{T}_R T_L \rangle_{ETC} \tag{1.29}$$

are generated similarly.

In any technicolor model, there is a spectrum of technimesons comparable to that of QCD: spin-zero technipions, spin-one isovector technirhos and isoscalar techniomegas, etc. In minimal technicolor, with a single doublet, $T = (T_U, T_D)$, three technipions are produced and are eaten by the weak gauge bosons. The lightest remaining technihadron is the ρ_T with decay channel $\rho_T \to W_L W_L$, i.e. longitudinal weak bosons. In this case, very high-energy collisions would be necessary to discover technicolor, beyond the scope of the LHC but perhaps within reach of the 200 TeV Very Large Hadron Collider (or the 2 TeV Superconducting Super Collider). However, in models with more techniquark doublets, signatures of technicolor are expected to be accessible at the LHC and perhaps even at the Tevatron.

Extended technicolor addresses the most pressing concerns regarding elementary Higgs models, but comes with challenges of its own. Key concerns are disagreements with experimental constraints on flavor-changing neutral currents (FCNC's), the precision electroweak measurements, and the large mass of the top quark. As described below, the FCNC and precision electroweak conflicts arise

from the assumption that the dynamics of extended technicolor are very similar to those of QCD, only at higher energies. This assumption is very possibly wrong. In particular, if the ETC gauge coupling runs very slowly, or walks, over a large range of energies above the electroweak scale, then the disagreements may be greatly reduced. This walking behavior could arise from proximity to a low-energy fixed point in parameter space; i.e., ETC could be a nearly conformal theory. Walking technicolor is perhaps the most natural way to explain the large separation of energy scales which the standard model seems to require.

Flavor-changing neutral currents occur in extended technicolor through the same interactions which generate fermion masses, through reactions of the form $q \to T \to q'$ and $q \to T \to T' \to q'$. Kaon physics has shown that reactions of this nature are strongly suppressed. Essentially, this means that the ETC scale must be at least 1,000 TeV. However, assuming QCD-like scaling, such a high scale for ETC breaking would result in quark, lepton, and technipion masses orders of magnitude too small. A walking coupling allows the model to accommodate both the suppression of the FCNC and proper masses for the fermions and technihadrons.

The basic electroweak parameters, $\alpha(M_W)$, M_W, and $\sin\theta_w$, have been measured with sufficiently high precision to place some experimental constraints on the Higgs sector. The oblique parameter S, which measures the M_W-M_Z splitting due to weak-isospin effects, is the most notable. Again assuming QCD-like scaling, extended technicolor predicts a value of order one for the S parameter, while the experimental limit is order 0.1. There is no calculation of the S parameter from extended technicolor without assuming QCD-like dynamics; this calculation is one of the primary goals of current lattice efforts.

The large value of the top quark mass, in particular in relation to the mass of the bottom quark, poses a problem which it seems extended technicolor can not solve without some fine tuning. The large mass demands a low ETC scale or an enhancement from walking which is too much to ask. Further, the large ratio of top to bottom mass requires large weak isospin violation which is very difficult to accommodate. The solution to this problem may lie in extensions to walking technicolor, such as topcolor-assisted technicolor [7].

Chapters 3 and 4 describe non-perturbative investigations into the subject of nearly conformal gauge theory in the context of technicolor. To date, the main objective of these investigations has been to locate the lower edge of the conformal window in theories with QCD-like $SU(3)$ gauge interaction and a relatively large number of fermions in the fundamental representation. Long-term goals include demonstrating a walking gauge coupling if possible, calculating the electroweak precision S parameter in a nearly conformal theory, and understanding the dynamics of this class of theories beyond serious limitations in perturbation theory. Additionally, studies of fermions in higher representations, in particular the two-index symmetric and adjoint, have been planned and begun. As described in Chapter 3, these are considered interesting possibilities due to the fact that higher representations may allow for walking with fewer flavors, which in perturbation theory reduces tensions with electroweak parameters.

Chapter 2

New Higgs Physics from the Lattice

Abstract

We report the first results from our comprehensive lattice tool set to explore non-perturbative aspects of Higgs physics in the Standard Model. We demonstrate in Higgs-Yukawa models that Higgs mass lower bounds and upper bounds can be determined in lattice simulations when triviality requires the necessity of a finite cutoff to maintain non-zero interactions. The vacuum instability problem is investigated and the lattice approach is compared with the traditional renormalization group procedure which sets similar goals to correlate lower and upper Higgs mass bounds with the scale of new physics. A novel feature of our lattice simulations is the use of Ginsparg-Wilson fermions to represent the effects of Top quark loops in Higgs dynamics. The need for chiral lattice fermions is discussed and the approach is extended to full Top-Higgs-QCD dynamics. We also report results from our large N_F analysis of Top-Higgs Yukawa models to gain analytic insight and to verify our new lattice tool set which is deployed in the simulations. The role of non-perturbative lattice studies to investigate heavy Higgs particle scenarios is illustrated in extensions of the Standard Model.

2.1 Introduction

The search for the Higgs has become a major issue in particle physics as the LHC is nearing its completion. The Standard Model (SM) cannot be considered complete given that the Higgs is as-yet unobserved and it is not clear how electroweak symmetry is broken in nature. If the Higgs is seen, its properties could tell us about physics beyond the Standard Model, such as the energy scale of a more fundamental theory. The current lower bound for the Higgs mass from direct searches is 114.4 GeV [8]. The Higgs mass can also be inferred indirectly by fitting the Standard Model to a host of electroweak precision measurements. The best perturbative fit gives $m_H = 76^{+33}_{-24}$ GeV, so the data certainly seem to prefer the Higgs to be light [9]. However, the global fitting procedure, which favors a surprisingly low Higgs mass, has its own intrinsic issues, perhaps a hint that deviations from the Standard Model are already present [10]. Larger Higgs masses together with new physics threshold effects at the TeV scale will require new extended analysis [11, 12] where non-perturbative effects may come into play.

Based on the assumption that the Standard Model is only valid up to some energy scale, lower and upper bounds on the Higgs mass were established before without relying on input from electroweak precision measurements. Bounds on the Higgs mass are valuable for two reasons. Firstly, they cut down the parameter space where one searches for a Standard Model Higgs. Secondly, if the Higgs is found, measuring its mass and knowing the bounds it must obey would indicate the maximum energy scale up to which the Standard Model can work. In phenomenology, the origin of the lower bound is thought to be the vacuum instability the Top quark loop would generate, if the Higgs mass were too light. The upper bound in phenomenological analysis is simply calculated by not allowing the running Higgs coupling $\lambda(t)$ to become strong at the cutoff scale Λ which represents new physics before $\lambda(t)$ would run into the fictitious Landau pole. These ideas on lower and upper Higgs mass bounds have been applied to the Standard Model for almost 30 years and have been increasingly refined.

The bounds given by the state-of-the-art calculations were reviewed in [13] and shown in Figure 2.1, based on the original work in [14] and [15]. There are

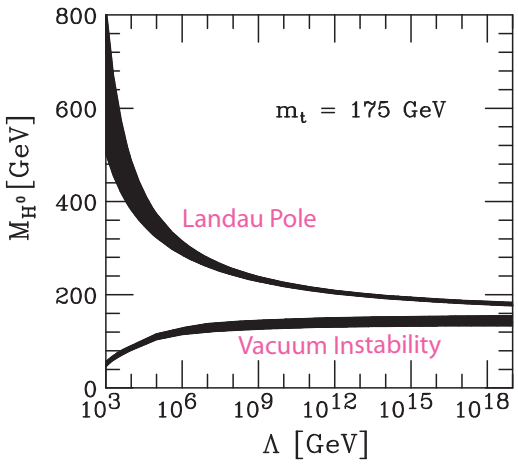

Figure 2.1: Upper and lower bounds for the Higgs mass as a function of the scale of new physics beyond the Standard Model, from [13].

several things one can learn from this plot. The Standard Model apparently cannot generate a Higgs boson heavier than 1 TeV without strong Higgs self-interactions and a low threshold for new physics in the TeV range, a scenario not consistent with the perturbative loop expansion of the electroweak precision analysis. What non-perturbative modifications on the TeV scale would support a heavy Higgs particle, consistent with electroweak precision data, is one of the motivations for our lattice studies [11, 12]. The lower bound is interesting for today's phenomenology, given the current experimental limits. If the Higgs mass is around 100 GeV, this would intersect with the lower bound in Figure 2.1 somewhere between 10 and 100 TeV, beyond which apparently new physics should enter.

One major goal of our lattice Higgs project is to understand the role of vacuum instability and the Landau pole in an exact non-perturbative setting when the intrinsic cutoff in the Higgs sector is not removable and low in the TeV range. Another goal is to explore the role of non-perturbative Higgs physics from the lattice in extensions of the perturbative SM analysis, including the possibility of a heavy Higgs particle within the Higgs reach of the LHC.

The outline of this paper is as follows. In section 2 we will report results from the large N_F analysis of the Top-Higgs Yukawa model of a single real scalar field coupled to N_F fermions. The influence of the non-removable intrinsic cutoff (triviality) on the exact renormalization group (RG) flow is exhibited. The vac-

uum instability problem of the model is discussed on the lattice in section 3 and compared with the traditional renormalization group procedure of the Standard Model (earlier versions of this work on vacuum instability have been discussed in [16] and [17]). In section 4 we present the Wilsonian view on the renormalization group as applied to the vacuum instability and Higgs lower bound problems. The first lattice simulation results on the Higgs mass lower bound, using chiral lattice fermions in Top-Higgs Yukawa models, are reported in section 5.

Using the higher derivative (Lee-Wick) extension of the Higgs sector [18, 19, 20], we will illustrate in section 6 how non-perturbative lattice studies might help to investigate heavy Higgs particle scenarios in the 500-800 GeV Higgs mass range relevant for future LHC physics. Constraints from electroweak precision data on the heavy Higgs particle are briefly discussed.

2.2 Top-Higgs Yukawa model in large $\mathbf{N_F}$ limit

For pedagogical purposes, we first consider a Higgs-Yukawa model of a single real scalar field coupled to N_F massless fermions. The saddle point approximation in the large N_F limit becomes exact and this will allow us to demonstrate that the theory is trivial. We will also calculate the flow of the renormalized couplings as a function of the energy scale to identify problems with the vacuum instability scenario when the intrinsic cutoff is non-removable. Similar behavior is expected at finite N_F which requires non-perturbative lattice simulations.

2.2.1 Renormalization scheme

Let us start with the bare Lagrangian of the Higgs-Yukawa theory in Euclidean space-time, which is

$$\mathcal{L} = \frac{1}{2}m_0^2\phi_0^2 + \frac{1}{24}\lambda_0\phi_0^4 + \frac{1}{2}\left(\partial_\mu\phi_0\right)^2 + \bar{\psi}_0^a\left(\gamma_\mu\partial_\mu + y_0\phi_0\right)\psi_0^a, \tag{2.1}$$

where $a = 1, ..., N_F$ sums over the degenerate fermion flavors and the subscript 0 denotes bare quantities. We rewrite this as

$$\begin{aligned}\mathcal{L} &= \frac{1}{2}m_0^2 Z_\phi \phi^2 + \frac{1}{24}\lambda_0 Z_\phi^2 \phi^4 + \frac{1}{2}Z_\phi \left(\partial_\mu \phi\right)^2 + Z_\psi \bar{\psi}^a \left(\gamma_\mu \partial_\mu + y_0 \sqrt{Z_\phi}\phi\right)\psi^a \\ &= \frac{1}{2}(m^2 + \delta m^2)\phi^2 + \frac{1}{24}(\lambda + \delta\lambda)\phi^4 + \frac{1}{2}(1 + \delta z_\phi)\left(\partial_\mu \phi\right)^2 \\ &\quad + (1 + \delta z_\psi)\bar{\psi}^a \gamma_\mu \partial_\mu \psi^a + \bar{\psi}^a (y + \delta y)\phi \psi^a, \end{aligned} \tag{2.2}$$

where we have introduced the wavefunction renormalization factors $Z_\phi = 1 + \delta z_\phi$, $Z_\psi = 1 + \delta z_\psi$ and renormalized parameters with their corresponding counterterms. The connections between the bare and renormalized parameters are

$$m_0^2 Z_\phi = m^2 + \delta m^2, \quad \lambda_0 Z_\phi^2 = \lambda + \delta\lambda, \quad Z_\psi \sqrt{Z_\phi} y_0 = y + \delta y. \tag{2.3}$$

In the limit where N_F becomes large, all Feynman diagrams with Higgs loops are suppressed relative to those with fermion loops. Hence, two of the counterterms vanish, $\delta y = 0$, $\delta z_\psi = 0$, as there are no radiative corrections to the fermion propagator or to the Higgs-fermion coupling. Let us specify the renormalization conditions which determine the remaining counterterms.

In the large N_F limit, the renormalized Coleman-Weinberg effective potential [21] is

$$U_{\text{eff}} = \frac{1}{2}m^2\phi^2 + \frac{1}{24}\lambda\phi^4 + \frac{1}{2}\delta m^2 \phi^2 + \frac{1}{24}\delta\lambda\phi^4 - 2N_F \int_k \ln[1 + y^2\phi^2/k^2] \tag{2.4}$$

containing the tree-level contributions from the renormalized parameters and their counterterms, and the infinite sum of all diagrams with one fermion loop and an even number of external ϕ legs. The factor N_F comes from all the possible fermions which can appear in the single loop and we use the notation $\frac{1}{(2\pi)^4}\int d^4k \to \int_k$ for loop integrals. The vacuum expectation value $\phi = v$ is where U_{eff} has an absolute minimum i.e. $U'_{\text{eff}}(v) = 0$. In the Higgs phase of the theory, $v \neq 0$. At tree-level, this gives the relation

$$m^2 + \frac{1}{6}\lambda v^2 = 0, \tag{2.5}$$

coming from the first two terms in Equation (2.4). Our first renormalization condition is that we want to maintain the tree-level relation in Equation (2.5) exactly,

giving

$$\delta m^2 + \frac{1}{6}\delta\lambda v^2 - 4N_F y^2 \int_k \frac{1}{k^2 + y^2 v^2} = 0. \tag{2.6}$$

The counterterms exactly cancel all the finite and infinite contributions of the radiative diagrams. The same relation can also be determined by demanding that the tadpole diagram is exactly cancelled by the counterterms.

In the Higgs phase, we define the Higgs fluctuation around the vev as $\phi = \varphi + v$. At tree-level, the mass of the Higgs fluctuation i.e. $U''_{\text{eff}}(v)$ is

$$m_H^2 = m^2 + \frac{1}{2}\lambda v^2 = \frac{1}{3}\lambda v^2. \tag{2.7}$$

In the large N_F limit, the inverse propagator of the Higgs fluctuation is

$$\begin{aligned} G^{-1}_{\varphi\varphi}(p^2) &= p^2 + m^2 + \frac{1}{2}\lambda v^2 + p^2\delta z_\phi + \delta m^2 + \frac{1}{2}\delta\lambda v^2 - \Sigma(p^2) \\ \Sigma(p^2) &= -4N_F y^2 \int_k \frac{y^2 v^2 - k.(k-p)}{(k^2 + y^2 v^2)((k-p)^2 + y^2 v^2)}, \end{aligned} \tag{2.8}$$

where all Higgs-loop diagrams are suppressed relative to the single fermion-loop diagram. We impose the condition that

$$G^{-1}_{\varphi\varphi}(p^2 \to 0) = p^2 + m_H^2, \tag{2.9}$$

which separates into two renormalization conditions:

$$\delta m^2 + \frac{1}{2}\delta\lambda v^2 - \Sigma(p^2 = 0) = 0 \tag{2.10}$$

and

$$\delta z_\phi - \left.\frac{d\Sigma(p^2)}{dp^2}\right|_{p^2=0} = 0. \tag{2.11}$$

The renormalization condition Equation (2.10) maintains the tree-level relation in Equation (2.7) exactly. Again, the counterterms precisely cancel all the finite and infinite radiative contributions. We should point out that the Higgs mass defined as the zero-momentum piece of $G^{-1}_{\varphi\varphi}$ is identical to that defined via the curvature $U''_{\text{eff}}(v)$. This is not the same as the true physical mass given by the pole of the propagator, and these masses can be related to one another in perturbation theory.

The renormalization conditions Equations (2.6) and (2.10) can easily be solved. Because we wish to demonstrate triviality in this theory, we use some

finite cutoff in the momentum integrals and examine what occurs as this cutoff is removed. We will use a simple hard-momentum cutoff $|k| \leq \Lambda$. Exactly the same conclusions would be reached using instead e.g. Pauli-Villars regularization. The non-zero counterterms after the loop integration are

$$\begin{aligned}
\delta m^2 &= \frac{N_F y^2}{2\pi^2}\left[\frac{1}{2}\Lambda^2 + \frac{y^4 v^4}{2(\Lambda^2 + y^2 v^2)} - \frac{1}{2}y^2 v^2\right] , \\
\delta\lambda &= -\frac{3N_F y^4}{\pi^2}\left[\frac{y^2 v^2}{2(\Lambda^2 + y^2 v^2)} - \frac{1}{2} - \frac{1}{2}\ln\left(\frac{y^2 v^2}{\Lambda^2 + y^2 v^2}\right)\right] , \\
\delta z_\phi &= -\frac{N_F y^2}{2\pi^2}\left[\frac{1}{4}\ln\left(\frac{y^2 v^2 + \Lambda^2}{y^2 v^2}\right) + \frac{-5\Lambda^4 - 3\Lambda^2 y^2 v^2}{12(\Lambda^2 + y^2 v^2)^2}\right] .
\end{aligned} \tag{2.12}$$

As we said earlier, in the large N_F limit, the fermion inverse propagator receives no radiative correction,

$$G^{-1}_{\psi\psi}(p) = p_\mu \gamma_\mu + yv, \tag{2.13}$$

so we identify the fermion mass as $m_t = yv$ (looking ahead to the Top quark), which we substitute into all of the above equations.

2.2.2 Triviality

Let us first consider the regime $m_t/\Lambda \ll 1$, where the cutoff is much larger than the physical scale. In this limit, we get

$$Z_\phi = \left[1 + \frac{N_F y_0^2}{8\pi^2}\left(\ln\left[\frac{\Lambda^2}{m_t^2}\right] - \frac{5}{3}\right)\right]^{-1} . \tag{2.14}$$

For any finite bare Yukawa coupling y_0, the Higgs wavefunction renormalization factor Z_ϕ vanishes logarithmically as the cutoff is removed, $m_t/\Lambda \to 0$. This same logarithmic behavior, for any choice of bare couplings, will appear in all of the renormalized couplings, leading to the triviality scenario: a finite cutoff must be kept to maintain non-zero interactions. Explicitly, the renormalized Yukawa coupling is

$$y^2 = y_0^2 Z_\phi = y_0^2\left[1 + \frac{N_F y_0^2}{8\pi^2}\left(\ln\left[\frac{\Lambda^2}{m_t^2}\right] - \frac{5}{3}\right)\right]^{-1} \to \left[\frac{N_F}{8\pi^2}\ln\frac{\Lambda^2}{m_t^2}\right]^{-1} , \quad \text{as } \frac{m_t}{\Lambda} \to 0. \tag{2.15}$$

For the renormalized Higgs coupling, we have

$$\begin{aligned}\lambda &= \lambda_0 Z_\phi^2 - \delta\lambda = \lambda_0 Z_\phi^2 + \frac{3N_F y^4}{\pi^2}\left[\frac{m_t^2}{2(\Lambda^2+m_t^2)} - \frac{1}{2} - \frac{1}{2}\ln\left(\frac{m_t^2}{\Lambda^2+m_t^2}\right)\right] \\ &\to Z_\phi^2\left[\lambda_0 + \frac{3N_F y_0^4}{\pi^2}\left(-\frac{1}{2} - \frac{1}{2}\ln\frac{m_t^2}{\Lambda^2}\right)\right] \to 12\left[\frac{N_F}{8\pi^2}\ln\frac{\Lambda^2}{m_t^2}\right]^{-1}, \\ &\quad \text{as } \frac{m_t}{\Lambda} \to 0.\end{aligned} \tag{2.16}$$

The slow logarithmic vanishing of y and λ allows to have a relatively large separation of cutoff and physical scales and still maintain significant interactions. However, the standard renormalization procedure of removing the cutoff completely gives a non-interacting theory. Although completely unphysical, we can also consider the limit $m_t/\Lambda \gg 1$, where the cutoff is much below the physical scale. From Equation (2.12), we see this gives $\delta\lambda = 0,\ \delta z_\phi = 0$, and hence $Z_\phi \to 1$. In this limit, the connection between bare and renormalized parameters is simply $\lambda = \lambda_0,\ y = y_0$. This result is not surprising: deep in the cutoff regime, we simply have the bare theory, with no separation into renormalized parameters and their counterterms. This will be relevant when we discuss whether the vacuum can become unstable.

2.2.3 Renormalization group flow

The physical properties of the theory are fixed as soon as one chooses a complete set of bare parameters. As the cutoff is varied, the renormalized couplings flow in order to maintain exactly the renormalization conditions we have imposed. Using the explicit cutoff dependence of y and λ, we can calculate this Callan-Symanzik flow. In the limit $m_t/\Lambda \ll 1$, from Equations (2.15) and (2.16), we have

$$\begin{aligned}\Lambda\frac{dy^2}{d\Lambda} &= -y_0^2 Z_\phi^2 \frac{N_F y_0^2}{4\pi^2} = -\frac{N_F y^4}{4\pi^2}\ , \\ \Lambda\frac{d\lambda}{d\Lambda} &= \frac{1}{16\pi^2}\left[-8N_F\lambda y^2 + 48N_F y^4\right]\ .\end{aligned} \tag{2.17}$$

The same β functions would be obtained in the large N_F limit for the running y and λ couplings in scale dependent RG flows using e.g. dimensional regularization,

where no cutoff would explicitly appear. (Since increasing Λ corresponds to decreasing mass scale μ, the β functions in Equation (2.17) have opposite signs). It is important to note that the two RG schemes have very different physical meanings: Equation (2.17) describes the response to changing the cutoff whereas the scale dependent RG flow compensates for the arbitrary choice of the renormalization scale at finite cutoff. When the cutoff is far above the physical scales, the finite cutoff effects are negligible and we expect to reproduce the unique cutoff-independent β functions. However, as the cutoff is reduced and m_t/Λ increases, this cannot continue to hold indefinitely, as the renormalized couplings must eventually flow to the bare ones, as explained above.

Let us demonstrate an explicit example of the Callan-Symanzik RG flow in the presence of a finite cutoff. In the large N_F limit, $m_t = yv = y_0 v_0$. The bare vev is determined by the minimum of the bare effective potential

$$U_{\text{eff},0} = \frac{1}{2} m_0^2 \phi_0^2 + \frac{1}{24} \lambda_0 \phi_0^4 - 2N_F \int_k \ln \left[1 + y_0^2 \phi_0^2 / k^2 \right]. \tag{2.18}$$

Using a hard-momentum cutoff, this gives

$$m_0^2 + \frac{1}{6} \lambda_0 v_0^2 - \frac{N_F y_0^2}{2\pi^2} \left[\frac{1}{2} \Lambda^2 + \frac{1}{2} y_0^2 v_0^2 \ln \left(\frac{y_0^2 v_0^2}{\Lambda^2 + y_0^2 v_0^2} \right) \right] = 0. \tag{2.19}$$

We express all dimensionful quantities in units of the cutoff Λ. We pick some fixed values for λ_0 and y_0. Varying the value of m_0^2/Λ^2 changes the solution v_0/Λ of Equation (2.19) and hence the ratio m_t/Λ. As we said, choosing the values of the bare parameters completely determines everything in the theory. For example, to attain a very small value of m_t/Λ requires m_0^2/Λ^2 to be tuned quite precisely. Using Equation (2.19), the critical surface, where $v_0/\Lambda = 0$, is the transition line

$$\frac{m_0^2}{\Lambda^2} - \frac{N_F y_0^2}{4\pi^2} = 0. \tag{2.20}$$

Using Equations (2.3) and (2.12), all of the counterterms and renormalized parameters can be expressed in terms of λ_0, y_0, m_0^2 and v_0. Solving this set of simultaneous equations is a simple numerical exercise. We make an arbitrary choice $\lambda_0 = 0.1, y_0 = 0.7$ which would correspond to the physical Higgs below its lower bound in phenomenological considerations. Varying the value of m_0^2/Λ^2, we explore numerically the range $10^{-13} < m_t/\Lambda < 10^2$. The results in a limited range

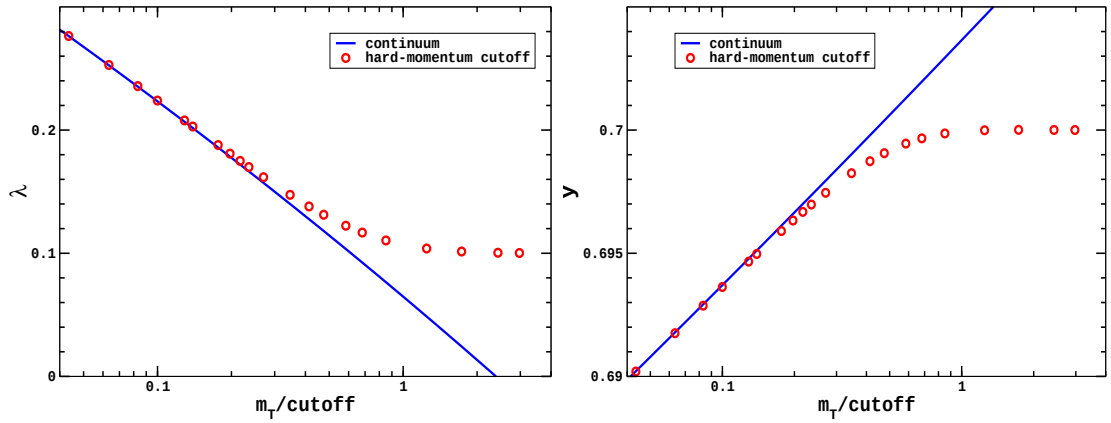

Figure 2.2: The exact RG flow of the renormalized couplings λ and y with the full cutoff dependence. The corresponding bare couplings are $\lambda_0 = 0.1$ and $y_0 = 0.7$. For large cutoff, the exact flow agrees with the continuum RG flow, where the cutoff dependence is omitted. For small cutoff, the exact RG flows to the bare couplings λ_0 and y_0, but the continuum RG misleadingly predicts that λ turns negative.

are plotted in Figure 2.2. When the cutoff is high, the exact RG flow is exactly the same as if the cutoff had been completely removed and follows precisely the continuum form of Equation (2.17). However, as the cutoff is reduced, the exact RG flow eventually breaks away from the continuum form and reaches a plateau at the value of the bare coupling.

The continuum RG in the above example predicts that λ turns negative at some energy scale as the flow continues. This was used in the past as an indication that the ground state of the theory turns unstable at that scale which would determine the energy scale of new physics necessary to sustain a particular value of the physical Higgs mass (vacuum instability bound). As shown above, the true RG flow with the full cutoff dependence saturates at λ_0 and does not turn negative under the necessary $\lambda_0 > 0$ stability requirement of the model. This makes the phenomenological RG method and the apparent vacuum instability quite suspect in the presence of the non-removable finite cutoff which is required by triviality of the renormalized couplings.

The absence of vacuum instability will be demonstrated directly in the next section using the Higgs effective potential. In sections 4 and 5 we will propose a

lattice strategy to determine the Higgs mass lower bound in the presence of an intrinsic cutoff without relying on the continuum RG flow. In this new strategy even the $\lambda_0 > 0$ condition might be relaxed by adding new irrelevant operators, like the $\frac{\lambda_6}{\Lambda^2}\phi^6$ term, to keep the stability of the cutoff theory intact.

2.3 The effective potential and vacuum instability

First, we will present here the RG improved one-loop calculation of the effective potential with unstable vacuum when the cutoff is ignored. Next we show the absence of vacuum instability when the cutoff is correctly enforced.

2.3.1 Continuum 1-loop effective potential

For the Higgs-Yukawa model with N_F fermions of Section 2, the 1-loop renormalized effective potential is

$$\begin{aligned} U_{\text{eff}} &= \frac{1}{2}m^2\phi^2 + \frac{1}{24}\lambda\phi^4 + \frac{1}{2}\delta m^2\phi^2 + \frac{1}{24}\delta\lambda\phi^4 - 2N_F\int_k \ln[1 + y^2\phi^2/k^2] \\ &+ \frac{1}{2}\int_k \left(\ln[k^2 + V''(\phi)] - \ln[k^2 + V''(0)]\right), \\ V &= \frac{1}{2}m^2\phi^2 + \frac{1}{24}\lambda\phi^4, \end{aligned} \tag{2.21}$$

where the Higgs-loop contributions are also included now. For consistency, we impose exactly the same renormalization conditions Equations (2.10) and (2.11) used in Section 2, including all the Higgs-loop radiative corrections. Because δy and δz_ψ are non-zero (we no longer impose the large N_F limit), we specify the two additional renormalization conditions. The fermion inverse propagator is

$$\begin{aligned} G^{-1}_{\psi\psi}(p) &= p_\mu\gamma_\mu + yv + \delta z_\psi p_\mu\gamma_\mu + \delta yv - \Sigma_F(p), \\ \Sigma_F(p) &= y^2\int_k \frac{-k_\mu\gamma_\mu + yv}{(k^2 + y^2v^2)((k-p)^2 + m_H^2)}, \end{aligned} \tag{2.22}$$

the radiative correction coming from a single Higgs-loop diagram, and we require that

$$G^{-1}_{\psi\psi}(p \to 0) = p_\mu\gamma_\mu + yv. \tag{2.23}$$

This gives two renormalization conditions,

$$\begin{aligned} &\delta y v - \Sigma_F(p \to 0) = 0 \ , \\ &\delta z_\psi - \left. \frac{d\Sigma_F}{d(p_\mu \gamma_\mu)} \right|_{p \to 0} . \end{aligned} \tag{2.24}$$

Again, the counterterms completely remove all the finite and infinite parts of the radiative corrections. We regulate the momentum integrals using e.g. a hard-momentum cutoff. The counterterms and the renormalized effective potential are calculated exactly using a finite cutoff. We then take the naive limit $\phi/\Lambda \to 0$ to remove all cutoff dependence. This ignores the fact that a finite and possibly low cutoff is required to maintain $\lambda, y \neq 0$ (a crucial point why the instability does not occur in the presence of finite cutoff).

The continuum form of the 1-loop renormalized effective potential is given by

$$\begin{aligned} U_{\text{eff}} &= \frac{1}{2}m^2\phi^2 + \frac{1}{24}\lambda\phi^4 - \frac{N_F y^4}{16\pi^2}\left[-\frac{3}{2}\phi^4 + 2v^2\phi^2 + \phi^4 \ln\frac{\phi^2}{v^2}\right] \\ &+ \frac{1}{16\pi^2}\left[\frac{1}{16}(\lambda^2\phi^4 - 2\lambda\phi^2 m_H^2)\ln\frac{m^2 + \lambda\phi^2/2}{m_H^2}\right. \\ &\left. + \frac{1}{16}m_H^4 \ln\frac{m^2 + \lambda\phi^2/2}{m^2} - \frac{3}{32}\lambda^2\phi^4 + \frac{7}{16}\lambda\phi^2 m_H^2\right], \end{aligned} \tag{2.25}$$

where $m_H^2 = \lambda v^2/3$. Due to our choice of renormalization conditions, the tree-level vev $v = \sqrt{3m_H^2/\lambda}$ is not shifted: one can check explicitly that U_{eff} in Equation (2.25) has its minimum at $\phi = v$. The large N_F limit can be recovered by omitting the Higgs-loop terms.

2.3.2 RG improved effective potential and vacuum instability

The stability of the ground state is determined by the behavior of U_{eff} for large ϕ. We see from Equation (2.25) that the dominant terms in this regime are of the form $\lambda^2\phi^4 \ln(\phi^2/v^2)$ and $-N_F y^4 \phi^4 \ln(\phi^2/v^2)$. The negative fermion term brings up the possibility that the vev v is unstable. Hence stability is determined by the relative values of λ^2 and y^4, which are related to m_H and m_t. If the fermionic term

dominates at large ϕ, the minimum at v is only a local one and will decay. If we believe that the vacuum is absolutely stable, then new degrees of freedom must enter at the scale where $U_{\text{eff}}(\phi)$ first becomes unstable. For given values of m_H and m_t, this predicts the emergence of new physics. Turning this around, let us fix m_t and ask that no new stabilizing degrees of freedom are needed for $\phi \leq E$. Then we obtain a lower bound $m_H(E)$: if the Higgs is lighter than this, U_{eff} is already unstable for ϕ below E because the fermion term dominates even earlier.

Improved vacuum instability can be shown via the running renormalized couplings in RG setting. We can define a set of renormalization conditions in the continuum, for example in the $\overline{MS}$ scheme, where the couplings flow with the renormalization scale μ. The 1-loop RG equations for the Higgs-Yukawa model are

$$\begin{aligned} \mu\frac{dy}{d\mu} &= \frac{1}{8\pi^2}(3+2N_F)y^4, \\ \mu\frac{d\lambda}{d\mu} &= \frac{1}{16\pi^2}(3\lambda^2+8N_F\lambda y^2-48N_F y^4). \end{aligned} \tag{2.26}$$

We can set the initial conditions $\lambda(\mu=v)=3m_H^2/v^2$ and $y(\mu=v)=m_t/v$. If m_t is sufficiently heavy relative to m_H, the Yukawa coupling dominates the RG flow and $d\lambda/d\mu < 0$. The renormalized Higgs coupling eventually becomes negative at some $\mu = E$. If the instability occurs at very large ϕ/v, large logarithmic terms $\ln(\phi/v)$ in U_{eff} might spoil the perturbative expansion. This can be reduced using renormalization group improvement to resum the leading large logarithms. The dominant terms of U_{eff} at large ϕ then become $\lambda(\mu)\phi^4(\mu)$. Hence $\lambda(E)=0$ indicates that the ground state is just about to become unstable.

2.3.3 The constraint effective potential on the lattice

We can calculate the exact effective potential non-perturbatively, using lattice simulations. This was first shown in the pure Higgs theory by Kuti and Shen [22]. There is some finite lattice spacing a on the lattice which restricts the momenta $|p_\mu| \leq \pi/a$ replacing the sharp momentum cutoff used in section 2. For a

Higgs-Yukawa theory with N_F fermions, the Euclidean lattice partition function is

$$Z = \prod_x \int d\phi_0(x) [\mathrm{Det}(D[\phi_0])]^{N_F} \exp(-S[\phi_0]), = \prod_x \int d\phi_0(x) \exp(-S_{\mathrm{eff}}[\phi_0])$$
$$S = \sum_x \frac{1}{2} m_0^2 \phi_0^2(x) + \frac{1}{24} \lambda_0 \phi_0^4(x) + \frac{1}{2} (\partial_\mu \phi_0(x))^2,$$
$$(D[\phi_0])_{xy} = \gamma_\mu \partial_{\mu,xy} + y_0 \phi_0(x) \delta_{xy}, \tag{2.27}$$

where the partial derivatives are replaced by finite lattice differences. If the integrand is positive-definite, it can be interpreted as a probability density and importance sampling (i.e. Monte Carlo integration) can be used to calculate expectation values, e.g. $\langle \phi_0 \rangle$, non-perturbatively with the exact distribution $[\mathrm{Det}(D)]^{N_F} \exp(-S)$. All dimensionful quantities are calculated in units of the lattice spacing a. There is a phase diagram in the bare-coupling space m_0^2, λ_0, y_0. The Higgs phase and the symmetric phase are separated by a second order transition, where the vev, va, and the masses $m_H a$ and $m_t a$, vanish. Since the vev and masses are non-zero in physical units, the transition corresponds to the continuum limit $a \to 0$. To make the cutoff $\Lambda = \pi/a$ large, the bare couplings must be tuned to be close to the transition line. If we calculate via simulations that e.g. $av = \langle a\phi \rangle \approx 0.05$ for some choice of bare couplings, we can use $v = 246$ GeV to convert this into a cutoff $\Lambda \approx 15$ TeV, as well as determine m_H and m_t in physical units.

In a finite space-time volume Ω, we will use the constraint effective potential [22, 23]. For a pure scalar field theory, this is

$$\exp(-\Omega U_\Omega(\Phi)) = \prod_x \int d\phi(x) \delta \left(\Phi - \frac{1}{\Omega} \sum_x \phi(x) \right) \exp(-S[\phi]). \tag{2.28}$$

The delta function enforces the constraint that the scalar field ϕ fluctuates around a fixed average Φ. The constraint effective potential $U_\Omega(\Phi)$ has a very physical interpretation. If the constraint is not imposed, the probability that the system generates a configuration where the average field takes the value Φ is

$$P(\Phi) = \frac{1}{Z} \exp(-\Omega U_\Omega(\Phi)), \quad Z = \int d\Phi' \exp(-\Omega U_\Omega(\Phi')). \tag{2.29}$$

This is in very close analogy to the probability distribution for the magnetization in a spin system. The scalar expectation value $v = \langle \phi \rangle$ is the value of Φ for which

U_Ω has an absolute minimum. In a finite volume, the constraint effective potential is non-convex and can have multiple local minima [24]. The standard effective potential $U_{\text{eff}}(\Phi)$ is always convex, even in a finite volume, as the Maxwell construction connects the various minima. The two effective potentials are identical in the infinite-volume limit, $\lim_{\Omega\to\infty} U_\Omega(\Phi) = U_{\text{eff}}(\Phi)$, and the constraint effective potential recovers the convexity property. In a finite volume, it is more useful to work with the constraint effective potential, where multiple minima can be observed and the transition between the Higgs and symmetric phases is clear. It is also more natural, as the probability distribution $P(\Phi)$ can be directly observed in lattice simulations. For the rest of this paper, we drop the subscript Ω.

2.3.4 Hybrid Monte Carlo algorithm and the effective potential

One way to extract the effective potential from lattice simulations is to generate the ensemble of configurations, calculate the average scalar field Φ for each configuration and hence the probability distribution $P(\Phi)$. The effective potential is extracted by numerically fitting $U_{\text{eff}}(\Phi)$ to $P(\Phi)$ using Equation (2.29). This gives the effective potential for all Φ from one simulation, but with limited accuracy. An alternative method is calculate the derivative of the effective potential. For the Higgs-Yukawa model with N_F degenerate fermions, the derivative is

$$\frac{dU_{\text{eff}}}{d\Phi} = m^2\Phi + \frac{1}{6}\lambda\langle\phi^3\rangle_\Phi - N_F y\langle\bar{\psi}\psi\rangle_\Phi, \quad \langle\bar{\psi}\psi\rangle_\Phi = \langle \text{Tr}(D[\phi]^{-1})\rangle_\Phi. \tag{2.30}$$

The expectation values $\langle ... \rangle_\Phi$ mean that, in the lattice simulations, the scalar field fluctuates around some fixed average value Φ. This method determines the effective potential with greater accuracy than fitting the distribution $P(\Phi)$, but the drawback is that a separate lattice simulation has to be run for every value of Φ. This is the method we use in our investigation of the vacuum instability.

In this section we use staggered fermions [25, 26], one flavor of which corresponds to four fermion flavors in the continuum. With one staggered fermion, the determinant $\text{Det}(D)$ is real but can be negative due to ϕ fluctuations. Then the partition function integrand is not positive-definite and Monte Carlo integra-

tion cannot be applied. To overcome this problem, we simulate two staggered fermions, corresponding to eight continuum flavors, as $[\mathrm{Det}(D)]^2$ guarantees a positive-definite density.We used staggered fermions only in the very early phase of our simulations. The complicated taste structure of staggered fermions with the related rooting issues and the lack of full chiral symmetry motivated the switch to chiral overlap fermions which are used now exclusively in our Higgs project. Staggered results for the effective potential, which are used here mainly for simplicity and pedagogy, have been replaced by simulations with chiral overlap fermions.

Configurations are generated using the Hybrid Monte Carlo algorithm [27], where a fictitious time t and momenta $\pi(x,t)$ are introduced. New configurations are generated from the equations of motion

$$\begin{aligned} \dot{\phi}(x,t) &= \pi(x,t) \ , \\ \dot{\pi}(x,t) &= -\left[\frac{\partial S_{\text{eff}}}{\partial \phi(x,t)} - \frac{1}{\Omega}\sum_y \frac{\partial S_{\text{eff}}}{\partial \phi(y,t)}\right], \end{aligned} \tag{2.31}$$

where the effective action S_{eff} is given in Equation (2.27). The second term in $\dot{\pi}(x,t)$ is included to enforce the constraints

$$\frac{1}{\Omega}\sum_y \phi(y,t) = \Phi, \quad \sum_y \pi(y,t) = 0. \tag{2.32}$$

We work with fixed lattice volumes of size $8^3 \times 16$. The scalar field has periodic boundary conditions, the fermionic field is periodic in the short directions and antiperiodic in the long direction. We use the standard leapfrog method to solve the equations of motion, where the step-size Δt is adjusted to achieve acceptance rates well above 90%, and each trajectory length satisfies $N_t \Delta t \geq 1$. For each simulation, we generate at least 10^4 configurations and check that correlations between the configurations are small.

The basic quantities of the theory are the bare fields and couplings. A particular choice of bare couplings puts us somewhere in the phase diagram and all physical quantities are now fixed. A separate constrained simulation is run for each value of Φ_0 to calculate the effective potential derivative. The expectation values we measure on the lattice are bare ones, so the simulations give the bare

equivalent of Equation (2.30), namely

$$\frac{dU_{\text{eff}}}{d\Phi_0} = m_0^2\Phi_0 + \frac{1}{6}\lambda_0\langle\phi_0^3\rangle_{\Phi_0} - N_F y_0\langle\bar{\psi}_0\psi_0\rangle_{\Phi_0}, \quad \langle\bar{\psi}_0\psi_0\rangle_{\Phi_0} = \langle \text{Tr}(D[\phi_0]^{-1})\rangle_{\Phi_0}, \tag{2.33}$$

which is converted using the relationship between the bare and renormalized fields,

$$\Phi = \frac{\Phi_0}{\sqrt{Z_\phi}}, \quad \frac{dU_{\text{eff}}}{d\Phi} = \sqrt{Z_\phi}\frac{dU_{\text{eff}}}{d\Phi_0}. \tag{2.34}$$

We measure the wave function renormalization factor Z_ϕ in separate unconstrained simulations.

We want to follow the behavior of U_{eff} as we approach the continuum limit, the critical surface in the bare-coupling space. We make an arbitrary choice $y_0 = 0.5$ and $\lambda_0 = 0.1$. The distance from the continuum limit is determined by the remaining bare coupling m_0^2. We obtained results for three choices $m_0^2 = 0.1, 0.25$ and 0.29. Typical non-perturbative measurements of the derivative $dU_{\text{eff}}/d\Phi$ are shown in Figure 2.3. All dimensionful quantities are in lattice units, e.g. $a \cdot \Phi$. What do we expect to see? In the Higgs phase of the theory, U_{eff} should have a local maximum at the origin and a local minimum for some non-zero $a \cdot \Phi$. If the vacuum is stable, the local minimum is in fact an absolute one. Let us first look at the results for $m_0^2 = 0.1$, shown in Figure 2.3. The simulations show that $dU_{\text{eff}}/d\Phi$ vanishes at the origin and at $a \cdot \Phi \approx 2.0$; these are the extrema. The derivative is negative between these points, so the origin is indeed a local maximum. For $a \cdot \Phi > 2$, the derivative is always positive and the local minimum appears to be an absolute one. If the vacuum is unstable, $dU_{\text{eff}}/d\Phi$ should turn negative at large $a \cdot \Phi$, for which the simulations show no evidence. In these units, the lattice cutoff is $\Lambda = \pi/a$ and the ratio of cutoff to scalar expectation value is $\Lambda/v \approx 1.5$. This is far from the continuum limit.

We vary the bare mass to get closer to the critical surface and the continuum limit for bare masses $m_0^2 = 0.25$ and 0.29 respectively. The simulations show the same qualitative behavior for U_{eff}: the origin is a local maximum, there is an absolute minimum for some non-zero $a\Phi$ and no sign of an instability in the potential. The minimum occurs at $a\Phi \approx 0.81$ and 0.47 respectively, for which $\Lambda/v \approx 3.9$ and 6.7, pushing towards the continuum limit.

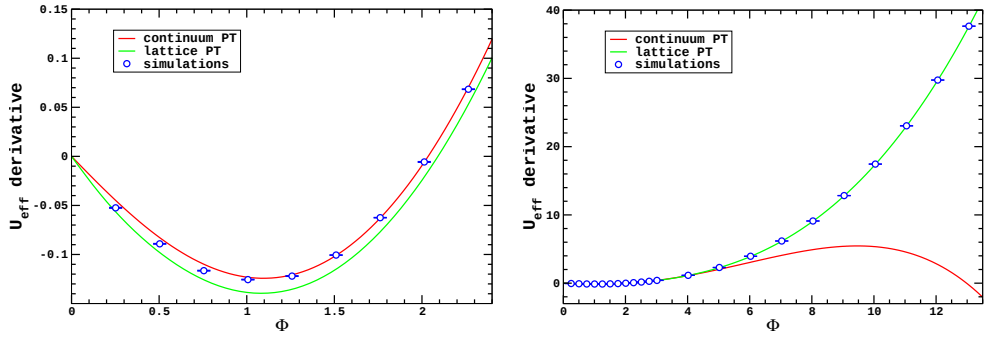

Figure 2.3: The derivative of the effective potential $dU_{\rm eff}/d\Phi$ for the bare couplings $y_0 = 0.5, \lambda_0 = 0.1, m_0^2 = 0.1$, for which the vev is $av = 2.035(1)$. The left side plot is a close-up of the behavior near the origin. The circles are the results of the simulations and the curves are given by continuum and lattice renormalized perturbation theory.

Table 2.1: The wave function renormalization factor, the renormalized scalar expectation value and the Higgs and Top masses, obtained from unconstrained lattice simulations. The bare couplings are those used for the lattice measurements of the effective potential $U_{\rm eff}$. The estimated errors are in parentheses.

y_0	λ_0	m_0^2	Z_ϕ	$av = \langle a\phi \rangle$	am_H	am_t
0.5	0.1	0.1	0.987(1)	2.035(1)	0.521(5)	0.9977(5)
		0.25	0.9705(8)	0.811(1)	0.297(4)	0.3906(7)
		0.29	0.9676(7)	0.4685(6)	0.248(3)	0.2230(3)

The first check of these calculations is to run separate unconstrained simulations with the same bare couplings, where $\sum_x \phi(x)$ is allowed to fluctuate freely, and to measure independently $v = \langle \phi \rangle$. This expectation value should be identical to the value of Φ where $U_{\rm eff}$ has an absolute minimum, as determined by the constrained simulations. In the unconstrained simulations, the second term for $\dot{\pi}(x,t)$ in Equation (2.31) is omitted. The results of the unconstrained simulations are given in Table 2.1. There is indeed perfect agreement between the measurements of $\langle a\phi \rangle$ and the location of the $U_{\rm eff}$ minimum obtained from the constrained simulations. The continuum perturbation theory calculation of $U_{\rm eff}$ is also shown in Figure 2.3. We only display the large N_F result: not surprisingly, for $N_F = 8$, the Higgs-loop contributions are negligible and can be omitted. We see excellent agreement with the non-perturbative simulations for $\Phi \lesssim v$, as shown in the left

side plot. However, the behavior as Φ increases is completely different, as shown in the right side plot. Continuum perturbation theory breaks away from the simulation results and predicts that the vacuum becomes unstable, with $dU_{\text{eff}}/d\Phi$ turning negative. The exact non-perturbative calculation shows no indication of this.

What can we conclude from the comparison? Continuum perturbation theory works well for Φ less than and even close to the lattice cutoff $\Lambda = \pi/a$, as shown by the very good agreement with the exact lattice calculations. This is the most that one could have expected. The instability is predicted at Φ well above the cutoff, which is completely unphysical and where one cannot expect the continuum calculation to apply. The exact effective potential, with the full cutoff dependence, is absolutely stable. The standard interpretation of the instability in the continuum U_{eff} would be to say new physics appears at this energy scale to stabilize the ground state. But the actual cutoff of the field theory is far below this scale, especially as we get closer to the continuum limit. The instability only appears when the finite cutoff effects are ignored — there is no need for new physics. One can ask, is it possible to arrange both the standard ground state and the instability to occur well below the regulator cutoff? If so, the instability would be a genuine low-energy prediction. The answer is no in the Top-Higgs Yukawa model, if only the standard terms are included in the lattice Lagrangian. In this case the only freedom one has is the choice of the bare couplings, and nowhere in the coupling-space is a genuine instability seen. If higher dimensional operators are included, the $\lambda_0 > 0$ condition perhaps could be relaxed by adding new irrelevant operators, like the $\frac{\lambda_6}{\Lambda^2}\phi^6$ term, to keep the stability of the cutoff theory intact. This scenario requires further investigation.

It can be shown in renormalized lattice perturbation theory that the breakdown of continuum perturbation theory is due solely to the finite cutoff. A finite cutoff is used in the lattice momentum integrals for the radiative corrections and the counterterms of U_{eff}, but otherwise the procedure is the same as in the continuum. In Figure 2.3 we see excellent agreement between simulations, and lattice and continuum renormalized perturbation theory for $\Phi/v \lesssim 1$. As Φ increases, lattice perturbation theory *exactly* tracks the non-perturbative result, showing a perfectly

stable ground state. The continuum calculation breaks down, not because of large couplings, but because of the neglected finite cutoff.

2.4 Wilsonian renormalization group and vacuum instability

Most of the original work on the consistency of quantum field theory considered only idealized theories, supposedly fundamental to describe physics at arbitrarily high energies. Although in the previous section on vacuum instability and the related Higgs lower bound problem we found a non-removable intrinsic cutoff, the analysis was based on the traditional renormalization procedure. The Wilsonian viewpoint of the renormalization group provides a broader and more complete perspective on the discussion.

2.4.1 Wilson's running Lagrangian

In the 1970s Wilson developed a new, intuitive way of looking at the renormalization of quantum field theories based on the flow of effective Lagrangians as generated by renormalization group transformations [28]. This is based on the realization that physics as we know it seems to be described by effective quantum field theories, which are useful only up to the energy scale Λ_0 where new and yet unknown physics is reached. Some smooth intrinsic regularization is introduced (inherited from new UV physics) at Λ_0 which in Euclidean space restricts the length p^2 of all four–momenta. Physics below the cutoff scale Λ_0 is described by a very general 'bare' Lagrangian $\mathcal{L}(\Lambda_0)$ with an infinite series of local terms, constrained only by symmetries. For any choice of the coupling constants in the local terms of the bare Lagrangian, the Euclidean path integral of the partition function has to be finite and well defined. The most fundamental constraint on the bare Lagrangian is the existence and stability of the functional integral which defines the Euclidean partition function. If the viewpoint of 'naturalness' is adopted, all the coupling constants of the higher dimensional operators are chosen to be of order one in units

of Λ_0. Using Wilson's exact renormalization group we can consider smoothly lowering the regularization scale to some value Λ_R say, of order the energy scale E far below Λ_0. To keep physics unchanged, the coupling constants must change with the regularization scale. Hence we have a running, or effective Lagrangian $\mathcal{L}(\Lambda)$, which flows with Λ and remains stable at every stage of the procedure in the sense of a convergent Euclidean path integral. Since we can use the Lagrangian $\mathcal{L}(\Lambda_R)$ to calculate low energy physics at the scale E, it is not the coupling constants at Λ_0 that are important, but those at the scale Λ_R. The bare couplings have to be close to a critical surface if $m_{ph}/\Lambda_0 \ll 1$ for the low energy physical masses m_{ph} of the theory.

An effective field theory is renormalizable if we can calculate all the S–matrix elements for processes with energy scale E, up to small errors which vanish as powers of E/Λ_0, once we have determined a finite number of coupling constants at some renormalization scale $\Lambda_R \sim E$. These coupling constants are called relevant; all others are irrelevant. Whatever values we choose for Λ_0 (as long as it is large enough) and the irrelevant bare couplings $\eta(\Lambda_0)$ (as long as they are natural enough), for a particular choice of the relevant operator set $\lambda(\Lambda_R)$, the irrelevant operator set $\eta(\Lambda_R)$ will be of the order of some power of (Λ_0/Λ_R). In other words, for any point on the submanifold of relevant couplings at Λ_R there is a flow towards it from a wide variety of initial Lagrangians at Λ_0, all of these being equivalent as far as the values of S–matrix elements for processes with energies of order $E \sim \Lambda_R$ are concerned. This more general aspect of renormalizability is the concept of universality. An effective quantum theory thus gives us a much more general notion of renormalizability than we had in conventional quantum field theory: the regularization need no longer be removed, and the irrelevant bare couplings need not be zero. It is useful now to adopt the Wilsonian view on the running effective Lagrangian to the Top-Higgs Yukawa model we investigated in the previous section.

2.4.2 Top-Higgs Yukawa model, vacuum instability, and running Lagrangian

Adapting the notion of the the running Wilson Lagrangian for the Top-Higgs Yukawa model, there are only two marginally irrelevant couplings, $\lambda(t)$ and $y(t)$, in addition to the relevant Higgs mass operator. It is important to note that the couplings for increasing $t = \log(\Lambda_0/\Lambda)$ flow from bare λ_0 and y_0 toward their low energy renormalized values as a function of the energy scale. For example, in the large N_F limit and for large t values, neglecting the irrelevant couplings, the flows are expected to look approximately the same as described by Equation (2.17). The Yukawa coupling $y(t)$ will monotonically decrease from its bare value y_0 towards zero, at the logarithmic rate of Equation (2.15) for large t. The Higgs coupling will start from its bare value $\lambda(0) = \lambda_0$ and either it will monotonically decrease, or after some initial rising it will turn around and continue to decrease monotonically towards zero, at the logarithmic rate of Equation (2.16) for large t. In the Wilsonian picture, all RG trajectories flow from the general coupling constant space of cutoff Lagrangians $\mathcal{L}(\Lambda_0)_{Top-Higgs}$ towards the trajectory specified by (2.15) and (2.16) with small but calculable corrections from irrelevant operators in the large t limit.

In the Wilsonian view of the running Lagrangian, the cutoff dependent Higgs mass lower bound can be determined in the space of the bare cutoff Lagrangians $\mathcal{L}(\Lambda_0)_{Top-Higgs}$ from the smallest allowed value of $\lambda(\Lambda_R)$ for a fixed $\Lambda_0/\Lambda_R \ll 1$ ratio where a natural choice for Λ_R is the weak boson mass m_Z, or the vacuum expectation value v. This calculation is, of course, very hard to implement operationally with a large number of bare couplings. The important stability condition is the only constraint (with, or without naturalness) on the space of cutoff Lagrangians. For example, the choice of $\lambda_0 < 0$ a priori should not be excluded at the cutoff scale Λ_0, but it requires the presence of some positive higher dimensional operator, like $\lambda_0^{(6)}/\Lambda^2 \cdot \phi^6$, with $\lambda_0^{(6)} > 0$, to provide stability. Whether the Higgs mass lower bound will be necessarily associated with the limit $\lambda_0 \to 0$, or the $\lambda_0 < 0$ region also needs to be explored remains an unresolved and interesting question.

In phenomenological applications an attempt is always made to simplify Wilson's framework of dealing with the full space of running Lagrangians. Invoking the $\Lambda_R/\Lambda_0 \to 0$ limit, only the running of the relevant and marginally irrelevant couplings is calculated and the effects of irrelevant operators are ignored. In addition, in the application of RG equations to the vacuum instability problem, the simplified equations on $\lambda(t)$ and $y(t)$ are running backward from the m_Z scale towards the cutoff Λ_0. This interchange of the natural Wilsonian UV $\to$ IR flow with the IR $\to$ UV integration of relevant couplings only is a nontrivial proposition because the Wilsonian RG flow is not known to be reversible, and to set all the irrelevant couplings to zero at the scale $\Lambda_R = m_Z$ would require an unknown extension of the space of cutoff Lagrangians $\mathcal{L}(\Lambda_0)_{Top-Higgs}$, if it exists at all.

In most of the phenomenological RG applications this is not a problem. We believe, however, that the RG treatment of the vacuum instability problem requires special care. What corresponds to the unstable U_{eff} in Figure 2.3 is the running $\lambda(t)$ which at some scale t_0, far below the cutoff scale, turns negative as the RG is running backward, from $t = \log\Lambda_0/m_Z$ towards the cutoff scale $t = 1$. It is a signal that higher dimensional operators must play a role to provide a continued stability to the theory on all scales. It is unlikely that a positive λ_0 on the cutoff scale can support this picture, forcing the running $\lambda(t)$ to turn positive again and produce an effective potential which will turn back positive again after a second minimum which might be lower than the original one where the spontaneously broken theory was built (decay of the false vacuum). It is more likely that this scenario, if it exists at all, will require the $\lambda_0 < 0$ extension of the space of bare Lagrangians. This is an extension which remains largely unexplored and we are just beginning to investigate it.

2.4.3 Phenomenology from 2-loop continuum RG

Vacuum instability was first raised in [29] and it has since been increasingly refined in application to the Standard Model [30, 31, 32, 33, 34, 35, 36, 37, 38, 39, 40, 41, 15, 42, 43]. The state-of-the-art calculation determines the effective potential to one-loop order, with RG improvement applied up to two-loop order

to the running couplings.

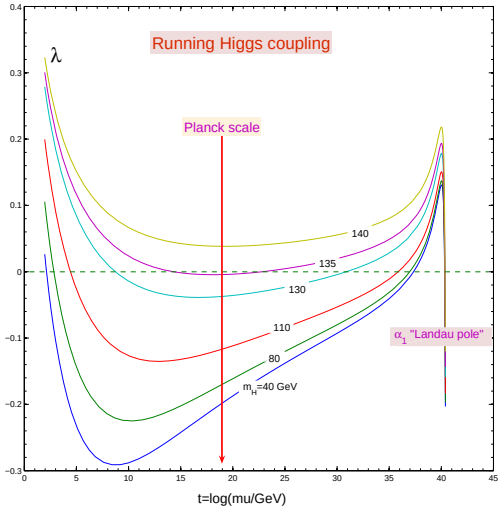

Figure 2.4: The running Higgs coupling is plotted for different choices of the Higgs mass from our numerical solution of the five coupled 2-loop RG equations for the $\lambda, y, g_1, g_2, g_3$ couplings. For input, $m_t = 175$ GeV was used with the experimental values of the g_1, g_2, g_3 gauge couplings. The 1-loop matching of the couplings and the starting scale of the RG was chosen at m_Z.

Results from [15] exhibit the unstable Standard Model effective potential for $m_H = 52$ GeV and $m_t = 175$ GeV, where the instability appears at $\phi = 1$ TeV. The lower bound shown in Figure 2.1 is also taken from [15]. The finite width of the lower bound is an estimate of the uncertainty of the theoretical calculation, including the effect of unconsidered higher-order contributions. The strict lower bound for the Higgs mass can be further refined if one allows the ground state to be unstable, but demands that the time required to tunnel away from the local minimum at $v = 246$ GeV is longer than the lifetime of the universe [44, 45, 46, 47, 48].

It is clear that the current experimental limits on m_H bring the lower bound into play. For example, a Higgs boson with a mass of 100 GeV should indicate a breakdown of the Standard Model around 50 TeV. However, a Higgs mass in the range 160 – 180 GeV apparently allows the Standard Model to be valid all the way up to the Planck scale. The occurrence of the vacuum instability mostly relies on the relative magnitudes of λ^2 and y^4 while both renormalized couplings

can remain small and all three gauge couplings of the SM are included. The perturbative RG approach, if cutoff effects can be safely ignored, seems to be on solid footing. However, cutoff effects played an important role in Top-Higgs Yukawa models where only the Higgs coupling λ and Yukawa coupling y drive the dynamics. In this approximation we have shown that vacuum instability cannot be induced with the SM Higgs potential in the cutoff Lagrangian (the possible role of higher dimensional operators to induce vacuum instability remains unclear, as we noted earlier). However, in the phenomenological application, all five couplings are running and it is important to ask: for the cutoff Λ at or below the Planck scale M_P, should we expect Top quark induced vacuum instability with the SM cutoff Lagrangian without adding new operators? Do we expect a qualitatively different picture when compared to the Top-Higgs Yukawa model? From Figure 2.4 we find that the running λ turns negative below the Planck scale for Higgs mass values lower than 135 GeV and remains negative when M_P is reached. Further lowering the Higgs mass lowers the scale where λ turns negative. It remains unclear how these RG flows would be effected by holding $\lambda_0 > 0$ in the SM Higgs Lagrangian at some cutoff scale Λ. How some higher dimensional operators might provide a well-defined cutoff theory for the choice $\lambda_0 < 0$ will require further investigation.

2.5 Higgs mass lower bound from the lattice

We would like to outline and implement the first step of a robust strategy to calculate the lower Higgs mass bound as a function of the lattice momentum cutoff. The question about breaking Euclidean invariance with the lattice cutoff will eventually have to be addressed also.

2.5.1 Yukawa couplings of the Top and Bottom quarks

The third, heaviest generation of quarks consists of the left-handed $SU(2)$ top-bottom doublet $Q_{\rm L} = \binom{t_L}{b_L}$ and the corresponding right-handed $SU(2)$ singlets $t_{\rm R}$, $b_{\rm R}$. The complex $SU(2)$ doublet Higgs field $\Phi(x)$ with $U(1)$ hypercharge $Y = 1$ is $\Phi = \binom{\phi^+}{\phi^0}$ where the suffixes +,0 characterize the electric charge +1, 0 of the

components. Since ϕ^+ and ϕ^0 are complex, we can introduce four real components, $\Phi = \binom{\phi_1+i\phi_2}{i\phi_3+\phi_4}$ and the Higgs potential will have O(4) symmetry, with broken custodial O(3) symmetry, if the Yukawa couplings y_t and y_b, defined below, are different. The Higgs potential in the complex doublet notation has the form,

$$V(\Phi) = \frac{1}{2}m^2\Phi^\dagger\Phi + \frac{\lambda}{24}(\Phi^\dagger\Phi)^2. \tag{2.35}$$

The Higgs field acquires a vacuum expectation value responsible for the spontaneous electroweak symmetry breaking with $\langle\phi_4\rangle = v$ and the first three components vanishing. The vacuum expectation value v can be related to the Higgs coupling constant by $v = \sqrt{3/\lambda}m_H$ with the relation between the Higgs mass m_H and m given by Equation (2.7).

Of the four Higgs components three represent Goldstone degrees of freedom, which at finite weak gauge coupling become the longitudinal degrees of freedom of the massive weak gauge bosons with mass $m_W = vg_2/2$. The fourth component corresponds to the physical Higgs boson field. We do not use the Higgs mechanism in the limit of zero weak gauge couplings and keep all four Higgs field components where the ϕ_1, ϕ_2, ϕ_3 fluctuations represent Goldstone particles with the symmetry breaking in the ϕ_4 direction. In the SM Lagrangian all four Higgs components are treated on equal footing where $\mathcal{L}_{\text{Yukawa}}$ describes the interactions of the $SU(2)_L$ doublet Higgs field with the quark fields

$$\mathcal{L}_{\text{Yukawa}} = y_t \cdot \overline{Q}_{\text{L}}\Phi^c t_R + y_b \cdot \overline{Q}_{\text{L}}\Phi b_R + \text{h.c.} \tag{2.36}$$

$\Phi^c = i\tau_2\Phi^*$ is the charge conjugate of Φ, τ_2 the second Pauli matrix, y_t, y_b are the top and bottom Yukawa couplings, respectively. When they are equal, the O(3) custodial symmetry of the Higgs potential is preserved after symmetry breaking. For unequal couplings, only the $SU(2)_L$ symmetry of the Lagrangian is maintained. It is easy to write out the Yukawa couplings in components:

$$\begin{aligned} \mathcal{L}_{\text{Yukawa}} \;=\; & y_t\{\bar{t}_L(\phi_4 - i\phi_3)t_R + \bar{b}_L(i\phi_2 - \phi_1)t_R\} + \\ & y_b\{\bar{t}_L(\phi_1 + i\phi_2)b_R + \bar{b}_L(i\phi_3 + \phi_4)b_R\} \;+\; h.c. \end{aligned} \tag{2.37}$$

All masses are proportional to v as they are induced by spontaneous symmetry breaking.

2.5.2 One-component Top-Higgs Yukawa model

We have used lattice simulations to study the Higgs-Yukawa model with a single real scalar field coupled to the Top quark with three colors using chiral overlap fermions. This theory has only a Higgs particle and no Goldstone bosons, and the Top quark color indices correspond to three degenerate fermions. We will not be able to calculate a lower bound directly relevant to phenomenology. Our purpose here is to explain in a simpler model how this non-perturbative calculation can be applied to a more realistic approximation of the Standard Model.

The Yukawa interaction Lagrangian in Equation (2.38) has a straightforward chiral lattice implementation in the overlap formulation where the chiral left-handed and right-handed fermion components are precisely defined. The simulation of the full doublet with the heavy Top and much lighter b quark would be very difficult on the lattice with two very different mass scales for m_t and m_b after spontaneous symmetry breaking.

One could choose for a pilot study the degenerate case $y_t = y_b$ which has a recent lattice implementation [49, 50]. In this limit, there are three massless Goldstone particles contributing to Top-Higgs dynamics. When the weak gauge couplings are turned on, the massless Goldstone modes become the longitudinal components of the massive weak gauge bosons via the Higgs-Kibble mechanism. The limitation of the four-component model with degenerate quark doublet is the artificially enhanced fermion feedback into Higgs dynamics.

Although the degenerate model of the Top and Bottom quarks is easy to accommodate in our Higgs lattice toolbox, we chose the single component Higgs Yukawa model for our pilot study with only the Top quark included. When the weak gauge couplings are turned on, one can choose unitary gauge to eliminate the three Goldstone components. In this gauge, ignoring the weak gauge coupling effects to leading order, one is left with diagonal Top and Bottom quark Yukawa couplings where the b quark is decoupled in the $y_b = 0$ limit. This is not a full justification for keeping the single Higgs field only, and the price to pay is the absence of feedback from the Goldstone modes into Higgs dynamics. Since the primary purpose of the initial phase of our Higgs project is to develop a comprehensive

Higgs lattice toolbox and test its various uses, the limited one-component Higgs field dynamics will provide very useful information. The next logical step will be to restore the four components of the Higgs field which requires the b quark, and break the mass degeneracy moving toward the $y_b \ll y_t$ limit.

2.5.3 Phase diagram with chiral overlap fermions

Lattice Yukawa models with staggered and Wilson fermions were studied before [51, 52, 53]. In this work, we adopted the overlap fermion operator to represent the chiral Yukawa coupling between the Top quark fermion field and the Higgs field. Although this is the most demanding choice for dynamical fermion simulations, staggered and Wilson fermions are not suitable for our goals. We discussed some difficulties with staggered fermions in section 3. The difficulties with Wilson fermions are worse. It turns out to be impossible to tune to the critical surface of the Top-Higgs lattice Yukawa model with Wilson fermions while keeping the Wilson doublers on the cutoff scale. This is different from QCD applications of Wilson fermions.

Our massless overlap Dirac operator is defined as $a \cdot D = 1 + \gamma_5 \mathrm{sign}(\mathrm{H_w})$ with $H_w = \gamma_5 D_w$ where D_w is the usual Wilson-Dirac matrix with a negative mass which for $a = 1$ has the form

$$(D_w)_{yx} = 3\delta_{xy} - \frac{1}{2}\sum_{\mu}\Big((1+\gamma_\mu)U_\mu(x-y)\delta_{x,y+\mu} + (1-\gamma_\mu)U^\dagger_\mu(x)\delta_{x,y-\mu}\Big) \ . \quad (2.38)$$

Using the modified $\hat{\gamma}_5 = \gamma_5(1 - aD)$ gamma matrix, we define two projection operators, $P_\pm = \frac{1}{2}(1 \pm \gamma_5), \widehat{P}_\pm = \frac{1}{2}(1 \pm \hat{\gamma}_5)$, and chiral fermion components, $\bar{\psi}_{L,R} = \bar{\psi}P_\pm, \psi_{R,L} = \widehat{P}_\pm\psi$. The scalar and pseudoscalar densities are given by $S(x) = \bar{\psi}_L\psi_R + \bar{\psi}_R\psi_L = \bar{\psi}(1 - \frac{a}{2}D)\psi$ and $P(x) = \bar{\psi}_L\psi_R - \bar{\psi}_R\psi_L = \bar{\psi}\gamma_5(1 - \frac{a}{2}D)\psi$.
The Top-Higgs Yukawa model with overlap fermions is defined by the Lagrangian

$$\begin{aligned}\mathcal{L} \ &= \frac{1}{2}m_0^2\phi_0^2 + \frac{1}{24}\lambda_0\phi_0^4 + \frac{1}{2}\left(\partial_\mu\phi_0\right)^2 + \\ &\quad \bar{\psi}_0^a\big[D + y_0 \cdot \phi_0(1 - \frac{a}{2}\cdot D)\big]\psi_0^a \ , \end{aligned} \quad (2.39)$$

where the bare overlap fermion field ψ_0 and the overlap Dirac operator D were introduced earlier. Derivatives are represented by finite lattice differences in Equa-

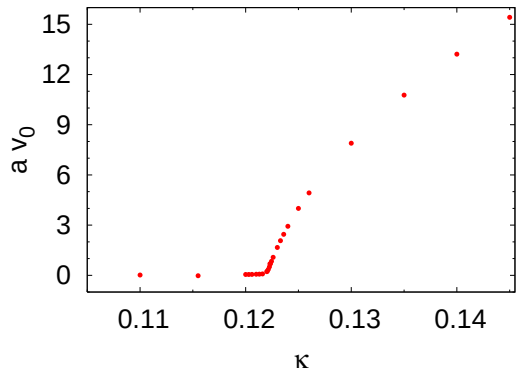

Figure 2.5: The vacuum expectation value of the lattice field ϕ_0 is plotted in lattice spacing units a as a function of the hopping parameter for fixed values of $\tilde{\lambda}_0 = 10^{-4}$, $\tilde{y}_0 = 0.35$ with 3 colors of the Top quark. The lattice size is $12^3 \times 24$ for the plotted data. The complete phase diagram can be mapped out by varying $\tilde{\lambda}_0$ and $\tilde{y}_0$ to determine $\kappa_c(\tilde{\lambda}_0, \tilde{y}_0)$.

tion (2.39) and summation over a=1,2,3 for Top color is understood. The gauge link matrices are set to the unit matrix in Equation (2.38).

The starting point for simulations is the phase diagram of the theory in the bare coupling space of m_0^2, λ_0, and y_0. The actual location of the critical surface is determined from the condition $av_0 = 0$ in a large set of non-perturbative lattice simulations. This is shown in Figure 2.5 where the critical critical hopping parameter for a particular choice of bare couplings is calculated. The Higgs part of the lattice Lagrangian is parametrized in the simulations as

$$\mathcal{L} = -2\kappa \sum_{\mu} \tilde{\phi}_0(x)\tilde{\phi}_0(x+\mu) + \tilde{\phi}_0^2(x) + \tilde{\lambda}_0(\tilde{\phi}_0^2(x) - 1)^2 \ ,$$

with $\phi_0 = \sqrt{2\kappa}\tilde{\phi}_0$, and rescaled notation $\tilde{y}_0 = y_0\sqrt{2\kappa}$ for the Yukawa coupling. The odd number of colors of the single fermion required the application of the Rational Hybrid Monte Carlo (RHMC) algorithm for chiral overlap fermion. The first new code we developed was based on [54, 55]. This is the code which is mostly used in our Top-Higgs-QCD simulations. We also developed a special FFT version of the RHMC algorithm which exploited the special structure of the Yukawa coupling in the overlap Dirac operator of the Top-Higgs model. In the FFT code, Fourier acceleration is used in the evolution of the molecular dynamics trajectories which

significantly reduced the autocorrelation time between independent configurations. The details of our RHMC algorithms will be described elsewhere.

2.5.4 Comparison of large N_F and Monte-Carlo results

The algorithm was thoroughly tested in the large N_F expansion of the model where we simulated a sequence of N_F fermions, each with 3 colors, which can also be interpreted as the Top quark with $3N_F$ colors. The $N_F \to \infty$ limit of the vacuum expectation value v and the Top mass m_t were calculated in rescaled λ_0/N_F and $y_0/\sqrt{N_F}$ variables for the finite volumes of the simulations, for fixed value of m_0^2. For a particular choice of the rescaled couplings, v and m_t are plotted in Figure 2.6 as a function of $1/N_F$.

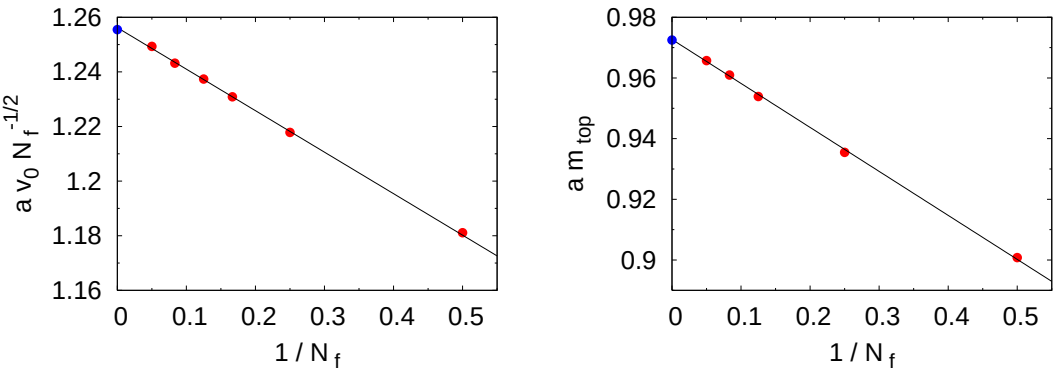

Figure 2.6: The vacuum expectation value v of the scaled Higgs filed is plotted on the left as a function of $1/N_F$ for $3N_F$ fermion degrees of freedom. The blue dot marks the $1/N_F \to 0$ limit. The right side plot shows the Top mass as a function of $1/N_F$ with the blue dot marking the calculated $1/N_F \to 0$ limit. The lattice size was $12^3 \times 24$ for every simulation point.

The largest number of fermions was $3N_F = 60$ in the sequence. The solid line indicates the scaled asymptotic value of v and m_t. The finite N_F data were numerically fitted with an added $1/N_F$ correction term which allows numerical extrapolation to the $1/N_F \to 0$ limit with perfect agreement. For example, in the *vev* test of Figure 2.6 the fitted curve is $1.2562(4) - 0.152(2)/N_F$ and the large N_F calculation gives 1.2555(7) asymptotically, in excellent agreement with the simulations. The sequence of simulations were done with bare parameters

$y_0\sqrt{N_F} = 0.7184$, $\lambda_0 \cdot N_F = 10^{-3}$, and $m_0^2 = 0.0637$. For the same sequence, the Top quark pole mass m_t was fitted on the right side of Figure 2.6 as $0.9727(5) - 0.145(2)/N_F$. The inverse propagator mass asymptotically is 0.9025 which converts to pole mass $m_t = 0.9725$ at the finite lattice spacing a of the simulations by the formula $am_t = \ln\frac{2+am}{2-am}$, in perfect agreement between simulations and the large N_F prediction. The complete agreement between the analytic large N_F prediction and the Monte-Carlo results provides a very strong cross-check for the correctness of our simulation algorithm and the analytic framework.

2.5.5 First results on Higgs mass lower bound

After thorough validation of our algorithm, we turned to a preliminary determination of the Higgs mass lower bound in the single component Top-Higgs Yukawa model. The heavy Top quark will constrain the lightest possible Higgs for any given cutoff in the single component Top-Higgs Yukawa model. The starting point for simulations is the phase diagram of the theory in the bare coupling space of m_0^2, λ_0 and y_0. For every choice of the bare parameter set, the vacuum expectation value v and the Higgs and Top masses take some values in lattice cutoff units. Keeping both the cutoff and the Top mass fixed in physical vev units, we explore all allowed bare couplings and find the lightest Higgs the theory can sustain. Repeating this procedure at various distances from the critical surface determines how the Higgs lower bound varies with the cutoff. For the Euclidean path integral to exist, we have to require $\lambda_0 \geq 0$ in the model. We could also consider a more general Higgs action where the constraint $\lambda_0 \geq 0$ is relaxed when positive terms like ϕ_0^6 are added in the higher-dimensional bare coupling constant space of the bare Lagrangian. For now we do not include such terms which are part of our ongoing investigations.

Figure 2.7 displays our preliminary results which are not far from what is expected from the application of the renormalization group. Lattice artifacts will require additional interpretation in the low momentum cutoff range of the simulations.

Adding the QCD gauge coupling

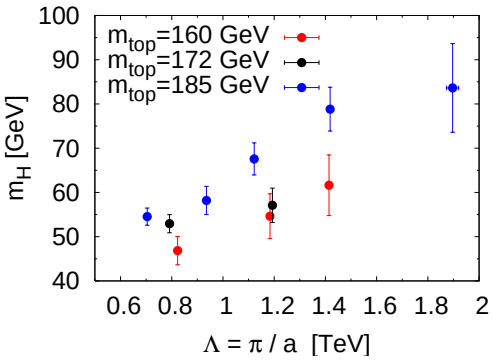

Figure 2.7: The lowest Higgs mass is plotted as a function of the lattice momentum cutoff for three different values of the Top mass. All simulation data are converted to physical units using $v = 246$ GeV.

Our algorithm and simulation code has been extended to the Top-Higgs-QCD code of three coupling constants. The only change is to include the SU(3) matrix link variables in the Wilson operator of Equation (2.38) in our construction of the chiral overlap operator. The numerical determination of the phase diagram and the Higgs mass lower bound in the extended model with λ, y, g_3 couplings (Top-Higgs-QCD model) is part of our ongoing Higgs project.

2.6 Higgs mass upper bound and the heavy Higgs particle

In this section we will review earlier results on the Higgs mass upper bound from lattice calculations and illustrate with the higher derivative (Lee-Wick) extension how a heavy particle might be exhibited without contradictions with electroweak precision data.

2.6.1 Higgs sector as an effective field theory

In the Wilsonian view of section 4, the Standard Model is expected to have some yet unknown UV completion above a certain energy threshold Λ_0. This

threshold could be as high as $\Lambda_0 = M_{\rm Planck}$, or as low as $\Lambda_0 = 1$ TeV. Below scale Λ_0 the SM is described by the familiar degrees of freedom for the known particles, including fermions and gauge bosons, in addition to the four-component Higgs field. For illustration, we will choose $\Lambda_0 = M_{\rm Planck}$ first in the description of the Higgs sector without gauge and Yukawa couplings. Generalization to the full Standard Model does not add to the purpose of the discussion here. Lowering the cutoff into the TeV range will be part of the discussion. If the Higgs sector is treated as an effective theory, the regulator is chosen for us as an intrinsic part of the theory. Euclidean four–momenta are smoothly cut off when their lengths exceed some scale Λ_0. In this way all momentum integrals are made manifestly convergent, and no infinities are encountered. The simplest choice is an exponential cutoff function in the propagators,

$$K_\Lambda(p) = \exp\left[-\frac{p^2}{\Lambda_0^2}\right] , \tag{2.40}$$

which can be built into the Lagrangian $\mathcal{L}(\Lambda_0)$ for non-perturbative calculations. A mass term could have been added to p^2 in Eq. (2.40) but we simplified the notation for this qualitative discussion. The general O(4) Higgs Lagrangian at scale $\Lambda_0 = M_{\rm Planck}$ is given by

$$\begin{aligned} \mathcal{L}_{Higgs} &= \frac{1}{2}\partial_\mu\phi^a\partial^\mu\phi^a + \frac{1}{2}\mu_0^2\phi^a\phi^a + \frac{\lambda_0}{4!}(\phi^a\phi^a)^2 + \frac{c_6}{M_{\rm Planck}^2}\,\Box\phi^a\,\Box\phi^a \\ &+ \frac{\lambda_6}{M_{\rm Planck}^2}(\phi^a\phi^a)^3 + \frac{c_8}{M_{\rm Planck}^4}\,\Box\partial_\mu\phi^a\,\Box\partial^\mu\phi^a + \ldots , \end{aligned} \tag{2.41}$$

where summation is implied over $a = 1, 2, 3, 4$. Only a few higher dimensional operators are included for illustration and the exponential cutoff is implicitly understood in the functional integral built on the Lagrangian of Eq. (2.41).

2.6.2 Higgs mass upper bound from the lattice

The highest allowed Higgs mass from the Lagrangian of Eq. (2.41) was investigated before, using lattice cutoff with c_6, λ_6, c_8 and all other higher dimensional couplings set to zero. Corrections from the higher dimensional operators are expected to be small, of the order of powers of $m_H/M_{\rm Planck}$ unless the cou-

plings c_6, λ_6, c_8, or any of the other higher dimensional couplings are pushed toward asymptotically large values. It is a limit which is considered artificial and far outside naturalness bounds.

Convincing evidence for the Higgs upper bound and its numerical value comes from lattice calculations [56, 57] where the derivatives are replaced by finite lattice differences giving up Euclidean invariance on the Planck scale. The advantage of the lattice approach is that the full λ_0 range can be scanned from 0 to ∞. This is important if the Higgs self-interaction is a marginally (logarithmically) irrelevant operator in the triviality scenario. In the limit of infinite cutoff, the largest allowed Higgs mass would be driven to zero (triviality of the renormalized Higgs coupling), but with the cutoff at the Planck scale we will get a definitive nonvanishing upper bound which is saturated at $\lambda_0 = \infty$ in the lattice approximation. The renormalized Higgs coupling at low energy can be defined as the ratio $\lambda_R = 3m_H^2/v^2$ where $v = 246$ GeV is the vev of the Higgs field (the fourth component of the O(4) field), and m_R is a renormalized Higgs propagator mass which is related in two-loop perturbation theory to the physical Higgs mass by the relation $m_H = m_R[1 + \frac{1}{8192\pi^2}\lambda_R^2]$. Based on non-perturbative lattice studies, we expect that the largest Higgs mass is obtained in the $\lambda_0 \to \infty$ limit. For any choice of λ_0 in the O(N) Higgs model we have

$$m_R = M_{\rm Planck} \cdot C(\lambda_0) \cdot (\beta_1 \lambda_R)^{-\frac{\beta_2}{\beta_1}} \exp\Big(-\frac{1}{\beta_1 \lambda_R}\Big)\Big\{1 + \mathcal{O}(\lambda_R)\Big\}, \tag{2.42}$$

with $\beta_1 = \frac{1}{3}(N+8)\frac{1}{16\pi^2}$ and $\beta_2 = -\frac{1}{3}(3N+14)\frac{1}{(16\pi^2)^2}$. The relevant choice is N=4 for the Standard Model. The non-universal amplitude $C(\lambda_0)$ is determined from matching to lattice calculations in the range $2\pi \le \Lambda/m_H \le 100$ [56, 57], leading to the upper bound $m_H = 145$ GeV in the $\lambda_0 = \infty$ limit, if the cutoff is at the Planck scale. In principle, the lattice cutoff could be replaced by the exponential cutoff function of the continuum theory. It would be required to replace the momentum square in Eq. (2.40) by its lattice version and take the inverse lattice spacing much larger than Λ_0. A new amplitude would emerge which could change the numerical value of the upper bound without breaking Euclidean invariance at finite cutoff. This is particularly useful when the cutoff is brought close to the low energy physical scale. In the discussion of the higher derivative extension of the

Higgs sector we will show how to insert a heavy continuum cutoff scale in the theory which was turned into a practical calculation before [18, 19]. This suggests that the insertion of the exponential cutoff scale might be feasible in practical calculations. What remains the most interesting question for LHC physics is the lowering the cutoff from the Planck scale into the TeV range. This will be illustrated next in the higher derivative extension of the Higgs sector with the scale of new physics in the TeV range.

2.6.3 Higher derivative (Lee-Wick) Higgs sector

An interesting extension of the Standard Model Higgs sector was proposed earlier by the addition of higher derivative operators using ideas originally discussed by Lee and Wick [18, 19, 58, 59]. Recently a complete Standard Model was constructed on similar principles [20]. Both constructions eliminate fine tuning in the Higgs sector and require ghost particles on the TeV scale represented by *complex pole pairs* in propagators with unusual physical properties. The analysis of the heavy Higgs particle from [18, 19] will be followed in our discussion.

In the minimal Standard Model with $SU(2)_L \times U(1)_Y$ gauge symmetry the Higgs sector is described by a complex scalar doublet Φ with quartic self-interaction as we discussed in section 5. The Higgs potential $V(\Phi^\dagger\Phi)$, as defined in Equation 2.35, is $SU(2)_L \times U(1)_Y$ invariant. It also has a global $O(4) \approx SU(2)_L \times SU(2)_R$ symmetry, larger than required by the $SU(2)_L \times U(1)_Y$ gauge symmetry. Before the weak gauge couplings are switched on, it is convenient to represent the Higgs doublet with four real components ϕ^a which transform in the vector representation of $O(4)$.

We will include new higher derivative terms in the kinetic part of the $O(4)$ Higgs Lagrangian,

$$\mathcal{L}_H = \frac{1}{2}\partial_\mu\phi^a\partial^\mu\phi^a - \frac{\cos(2\Theta)}{M^2}\,\Box\phi^a\,\Box\phi^a + \frac{1}{2M^4}\,\Box\partial_\mu\phi^a\,\Box\partial^\mu\phi^a - V(\phi^a\phi^a)\ , \quad (2.43)$$

where summation is implied over $a = 1, 2, 3, 4$. Also, in this subsection and the next, we use the Minkowski metric and a familiar, convenient form of the Higgs potential, $V(\phi^a\phi^a) = -\frac{1}{2}\mu^2\phi^a\phi^a + \lambda(\phi^a\phi^a)^2$. The higher derivative terms of the

Lagrangian in Eq. (2.43) lead to complex conjugate ghost pairs in the spectrum of the Hamilton operator. The complex conjugate pairs of energy eigenvalues of the Hamilton operator and the related complex pole pairs in the propagator of the scalar field ghost particles are parametrized by $\mathcal{M} = Me^{\pm i\Theta}$. The absolute value M of the complex ghost mass $\mathcal{M}$ will be set on the TeV scale. The Higgs Lagrangian $\mathcal{L}_H$ in Equation (2.43) describes a finite field theory without divergences, or fine tuning. It has a particularly simple form with the special choice $\Theta = \pi/4$ of the complex ghost phase,

$$\mathcal{L}_H = \frac{1}{2}\partial_\mu\phi^a\partial^\mu\phi^a + \frac{1}{2M^4}\,\Box\partial_\mu\phi^a\,\Box\partial^\mu\phi^a - V(\phi^a\phi^a)\ . \tag{2.44}$$

The $\Theta \to 0$ limit in Eq. (2.43) requires special attention. In this limit, the ghost particle becomes real and to avoid a double real pole in the propagator with problematic behavior, the choice $\Theta = 0$ requires to drop the $\frac{1}{2M^4}\,\Box\partial_\mu\phi^a\,\Box\partial^\mu\phi^a$ derivative term in the Lagrangian,

$$\mathcal{L}_H = \frac{1}{2}\partial_\mu\phi^a\partial^\mu\phi^a - \frac{1}{2M^2}\,\Box\phi^a\,\Box\phi^a - V(\phi^a\phi^a)\ , \tag{2.45}$$

the starting point of [20].

2.6.4 Gauge and Yukawa couplings

Gauging the Lagrangian (2.44) remained unpublished before [60]. For completeness, we present the main results. The construction of the higher derivative U(1) gauge Lagrangian mirrors Eq. (2.44) for the special choice $\Theta = \pi/4$,

$$\mathcal{L}_{\rm B} = -\frac{1}{4}F_{\mu\nu}F^{\mu\nu} - \frac{1}{4M^4}\Box F_{\mu\nu}\Box F^{\mu\nu}\ , \tag{2.46}$$

with U(1) gauge field B_μ and $F_{\mu\nu} = \partial_\mu B_\nu - \partial_\nu B_\mu$. In addition to the massless gauge vector boson, the higher derivative term in Eq. (2.46) will insert a ghost particle in the spectrum of the Hamiltonian with a complex conjugate pole pair parametrized by $\mathcal{M} = Me^{\pm i\Theta}$. For a general complex phase Θ an additional term will appear in the Lagrangian, in close analogy with the construction of Eq. (2.43).

The higher derivative Yang-Mills gauge Lagrangian for the $SU(2)_W$ weak gauge field W_μ will follow a similar construction adding the dimension eight ghost

term,

$$\mathcal{L}_{\rm W} = -\frac{1}{4}G^a_{\mu\nu}G^{a\mu\nu} - \frac{1}{4M^4}D^2G^a_{\mu\nu}D^2G^{a\mu\nu}\ , \tag{2.47}$$

where the notation $G^a_{\mu\nu} = \partial_\mu W^a_\nu - \partial_\nu W^a_\mu + g f^{abc} W^b_\mu W^c_\nu$ is used with the covariant derivative $D^{ab}_\mu = \delta^{ab}\partial_\mu + g f^{abc} W^c_\mu$. Higher derivative Lagrangians, similar to Eq. (2.47), were first introduced by Slavnov to regulate Yang-Mills theories [61].

Labeling the components of the complex $SU(2)_L$ Higgs-doublet field as $\Phi = \binom{\Phi^+}{\Phi^0}$ the gauged Higgs sector is described by the Lagrangian $\mathcal{L} = \mathcal{L}_W + \mathcal{L}_B + \mathcal{L}_{Higgs}$ with the Higgs Lagrangian

$$\mathcal{L}_{Higgs} = (D_\mu\Phi)^\dagger D^\mu\Phi + \frac{1}{2M^4}(D_\mu D^\dagger D\Phi)^\dagger(D_\mu D^\dagger D\Phi) - V(\Phi^\dagger\Phi) \tag{2.48}$$

where the Higgs potential is $V(\Phi^\dagger\Phi) = -\frac{1}{2}\mu^2\Phi^\dagger\Phi + \lambda(\Phi^\dagger\Phi)^2$ and the gauge-covariant derivative is $D_\mu\Phi = \left(\partial_\mu + i\frac{g}{2}\sigma\cdot W_\mu + i\frac{g'}{2}B_\mu\right)\Phi$. The higher derivative term in the fermion Lagrangian will take the form

$$\mathcal{L}_{fermion} = i\overline{\Psi}\not{D}\,\Psi + \frac{i}{2M^4}\overline{\Psi}\ \not{D}^2\not{D}\not{D}^2\ \Psi. \tag{2.49}$$

Next we will briefly summarize two important features of the higher derivative Higgs sector with the ghost mass scale in the TeV range. The RG running of the Higgs coupling freezes asymptotically and a much heavier Higgs particle is allowed in extended Higgs dynamics.

2.6.5 Running Higgs coupling in the higher derivative Higgs sector

This can be illustrated by calculating the scale dependent one-loop β-function within renormalized perturbation theory in the broken phase of the higher derivative O(N) Higgs sector [62, 63]. In addition to N-1 massless Goldstone modes, there is a massive Higgs excitation and a massive complex conjugate ghost pair appears in all N channels, as a consequence of the new derivative term in the Lagrangian. On a low energy scale μ, when $t = \log(\mu/v)$ is negative, the β-function is dominated by the Goldstone modes whose one-loop contribution is $\frac{N-1}{2\pi^2}\lambda^2(t)$. Above the Higgs mass threshold the massive Higgs loop contribution sets in and

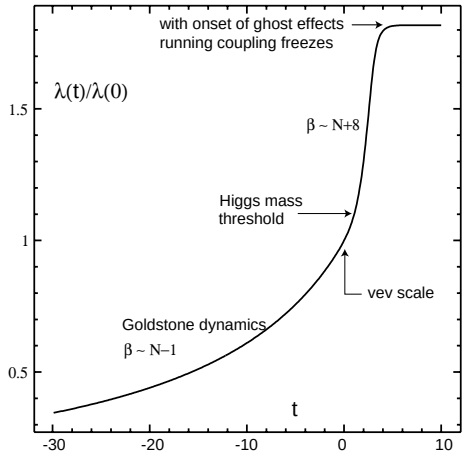

Figure 2.8: Running Higgs coupling in the higher Higgs sector.

the β-function becomes $\frac{N+8}{2\pi^2}\lambda^2(t)$ which is the familiar one-loop form in the minimal mass independent subtraction scheme of the standard O(N) model. As t increases, the complex ghost loop becomes increasingly important and well beyond the ghost scale M, for $t \gg \log(M/vev)$, the beta-function will asymptotically vanish. The running coupling constant $\lambda(t)$ first will grow as t increases, but eventually it will freeze at some asymptotic value $\lambda(\infty)$ as shown in Fig. 2.8. Ghost loops in the higher derivative Higgs model cancel the loops effects from the low-energy SM particles in the UV region and this 'anti-screening' effect opens up the possibility for such theories to be more strongly interacting than the standard Higgs sector.

2.6.6 Scattering amplitudes

The Higgs particle is defined as the resonance pole in the s-channel Goldstone scattering amplitude. The Goldstone amplitude can be calculated in the higher derivative Higgs sector of the O(N) Lagrangian in the large N approximation. In addition, the Higgs particle can be investigated directly in lattice simulations of the higher derivative model, just like in the standard Higgs sector.

In Figure 2.9 we plotted from [62, 64] the cross section as a function of the $\sqrt{s}$ center of mass energy in ghost mass units. The location of the complex Goldstone ghost pair in the scattering amplitude of the first Riemann sheet is determined by the choice of the phase angle $\Theta = \pi/4$ in the Lagrangian of

Equation (2.43). The peak in the cross section corresponds to the complex Higgs resonance pole on the second sheet of the scattering amplitude.

Also plotted in Figure 2.9 is the scattering phase shift as a function of $\sqrt{s}$. The phase shift has a sharp rise at the Higgs pole; however the cross section and the shape of the phase shift do not describe a standard Breit-Wigner shape in the presence of the ghosts and higher derivative Higgs dynamics. It is 'unusual' that the phase shift decreases as the energy gets through the real part of the ghost mass signaling acausal behavior in the scattering amplitude. It had been argued by Lee that this acausal behavior would only occur on microscopic scales, typical of the Compton wave length of ghosts, and it will not lead to macroscopic acausal observations. In the large N plots of Figure 2.9, the bare parameters were

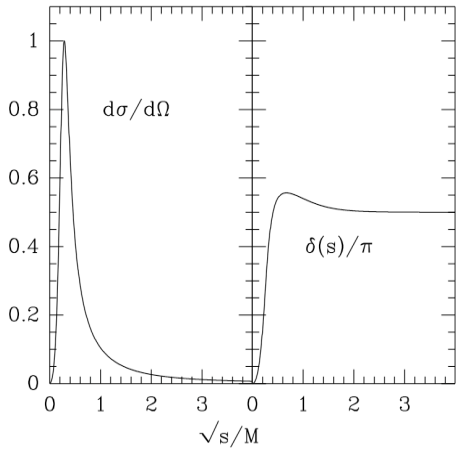

Figure 2.9: The Goldstone Goldstone scattering cross section and phase shift is plotted against the center of mass energy in large-N expansion for the Pauli-Villars higher derivative $O(N)$ theory. The input vev value is $v = 0.07$ in M units. The peak corresponds to the Higgs resonance, which is at $m_H = 0.28$ in M units. The scattering cross section is completely smooth across the so-called ghost pole locations.

tuned to $m_H = 1$ TeV for the Higgs mass with the ghost threshold located at 3.6 TeV. Lattice simulations confirmed similar strongly interacting heavy Higgs physics scenarios [62, 63].

2.6.7 Heavy Higgs particle and the ρ-parameter

We discussed in the introduction that a heavy Higgs particle, beyond the 200 GeV range, is not consistent with electroweak precision data in the perturbative sense. Concerns were raised earlier that the heavy Higgs particle of the higher derivative Higgs sector will contribute to the electroweak ρ-parameter beyond experimentally allowed limits [65]. Straightforward application of perturbative loop

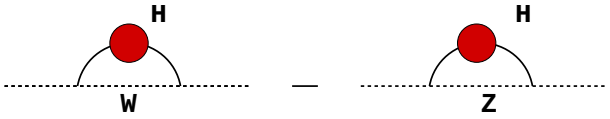

Figure 2.10: Higgs contribution to electroweak vacuum polarization operator.

integrals support this concern. However, with new physics on the TeV scale (represented by ghost particles) the loop integrals are considerably different. A crude estimate can be made by evaluating the contribution of the vacuum polarization tensors Π_W^H, Π_Z^H to the ρ-parameter,

$$\begin{aligned} \rho - 1|_{\text{Higgs}} &= \frac{\Pi_W^H}{M_{W,tree}^2} - \frac{\Pi_Z^H}{M_{Z,tree}^2} \\ &= -\frac{3}{4}g'^2 \int_{k^2<\Lambda^2} \frac{d^4k}{(2\pi)^4} \frac{\Sigma_H(k^2)}{(k^2+M_{W,tree}^2)(k^2+M_{Z,tree}^2)(k^2+\Sigma_H(k^2))} \ , \end{aligned}$$

with a sharp momentum cutoff in the TeV range and using the tree level Higgs self-energy operator $\Sigma_H(k^2)$. The reduction is quite large in comparison with the 1-loop perturbative formula. Replacing the cutoff integral by the Pauli-Villars regulator, which is appropriate for the higher derivative theory, we get similar reduction. The effects of the non-perturbative Higgs dynamics represented by a complicated $\Sigma_H(k^2)$ operator would have to be determined by non-perturbative simulations. If these reduction effects are not sufficient, one might need to add another Higgs doublet to the extended Higgs sector in the spirit of recent suggestions [66]. To exhibit a heavy Higgs particle as a broad resonance, with strong interaction and with acceptable ρ-parameter, remains an interesting challenge for lattice Higgs physics and model building.

Acknowledgements

J.K. is grateful for interesting discussions with J. Espinosa and D. N. would like to acknowledge helpful discussions with C. Hoelbling and K. Szabo. This research was supported by the DOE under grants DOE-FG03-97ER40546, DE-FG02-97ER25308, by the NSF under grant 0704171, by DFG under grant FO 502/1, and by the EU under grant I3HP.

Chapter 2, in full, is a reprint of the material as it appears in Proceedings of Science: Lattice 2007. Zoltan Fodor, Kieran Holland, Julius Kuti, Daniel Nogradi and Chris Schroeder, PoS LATTICE2007, 056, 2007. The dissertation author was a principal investigator and co-author of this paper.

Chapter 3

Probing Technicolor Theories with Staggered Fermions

Abstract

One exciting possibility of new physics beyond the Standard Model is that the fundamental Higgs sector is replaced by a strongly-interacting gauge theory, known as technicolor. A viable theory must break chiral symmetry dynamically, like in QCD, to generate Goldstone bosons which become the longitudinal components of the $W^{\pm}$ and Z. By measuring the eigenvalues of the Dirac operator, one can determine if chiral symmetry is in fact spontaneously broken. We simulate $SU(3)$ gauge theory with $n_s = 2$ and 3 staggered flavors in the fundamental representation, corresponding to $N_f = 8$ and 12 flavors in the continuum limit. Although our first findings show that both theories are consistent with dynamically broken chiral symmetry and QCD-like behavior, flavor breaking effects in the spectrum may require further clarifications before final conclusions can be drawn. We also compare various improved staggered actions, to suppress this potentially large flavor breaking.

3.1 Introduction

The LHC will probe the mechanism of electroweak symmetry breaking. A very attractive alternative to the standard Higgs mechanism, with fundamental scalars, involves new strongly-interacting gauge theories, known as technicolor [67, 68]. Such models avoid difficulties of theories with scalars, such as triviality and fine-tuning. Chiral symmetry must be spontaneously broken in a technicolor theory, to provide the technipions which generate the $W^{\pm}$ and Z masses and break electroweak symmetry. Although this duplication of QCD is appealing, precise electroweak measurements have made it difficult to find a viable candidate theory. It is also necessary to enlarge the theory (extended technicolor) to generate quark masses, without generating large flavor-changing neutral currents, which is challenging.

Technicolor theories have lately enjoyed a resurgence, due to the exploration of various techniquark representations [69]. Feasible candidates have fewer new flavors, reducing tension with electroweak constraints. If a theory is almost conformal, it is possible this generates additional energy scales, which could help in building the extended technicolor sector. There are estimates of which theories are conformal for various representations, shown in Fig. 3.1. For $SU(N)$ gauge theory, if the number of techniquark flavors is less than some critical number, conformal and chiral symmetries are broken and the theory is QCD-like. For future model-building, it is crucial to go beyond these estimates and determine precisely where the conformal windows are. There have been a number of recent lattice simulations of technicolor theories, attempting to locate the conformal windows for various representations [70, 71, 72, 73, 74].

3.2 Dirac eigenvalues and chiral symmetry

The connection between the eigenvalues λ of the Dirac operator and chiral symmetry breaking is succinctly given in the Banks-Casher relation [75],

$$\Sigma = -\langle\bar{\Psi}\Psi\rangle = \lim_{\lambda\to 0}\lim_{m\to 0}\lim_{V\to\infty}\frac{\pi\rho(\lambda)}{V}. \tag{3.1}$$

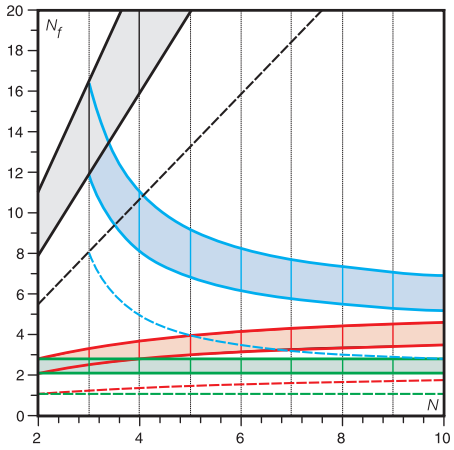

Figure 3.1: The conformal window for $SU(N)$ gauge theories with N_f techniquarks in various representations, from [69]. The shaded regions are the windows, for fundamental (gray), 2-index antisymmetric (blue), 2-index symmetric (red) and adjoint (green) representations.

To generate a non-zero density $\rho(0)$, the smallest eigenvalues must become densely packed as the volume increases, with an eigenvalue spacing $\Delta\lambda \approx 1/\rho(0) = \pi/(\Sigma V)$. This allows a crude estimate of the quark condensate Σ. One can do much better by exploring the ϵ-regime: If chiral symmetry is spontaneously broken, tune the volume and quark mass such that

$$\frac{1}{F_\pi} \ll L \ll \frac{1}{m_\pi}, \tag{3.2}$$

so that the pion is much lighter than the physical value, and finite-volume effects are dominant [76]. The chiral Lagrangian,

$$\mathcal{L} = \frac{F_\pi^2}{4}\mathrm{Tr}(\partial_\mu U \partial_\mu U^\dagger) + \frac{\Sigma}{2}\mathrm{Tr}[M(U+U^\dagger)], \quad U = \exp\left[\frac{i\pi^a T^a}{F_\pi}\right] \tag{3.3}$$

is dominated by the zero-momentum mode from the mass term and all kinetic terms are suppressed. In this limit, the distributions of the lowest eigenvalues are identical to those of random matrix theory (RMT), a theory of large matrices obeying certain symmetries [77]. To connect with RMT, the eigenvalues and quark mass are rescaled as $z = \lambda\Sigma V$ and $\mu = m\Sigma V$, and the eigenvalue distributions also depend on the topological charge ν and the number of quark flavors N_f. RMT is a very useful tool to calculate analytically all of the eigenvalue distributions.

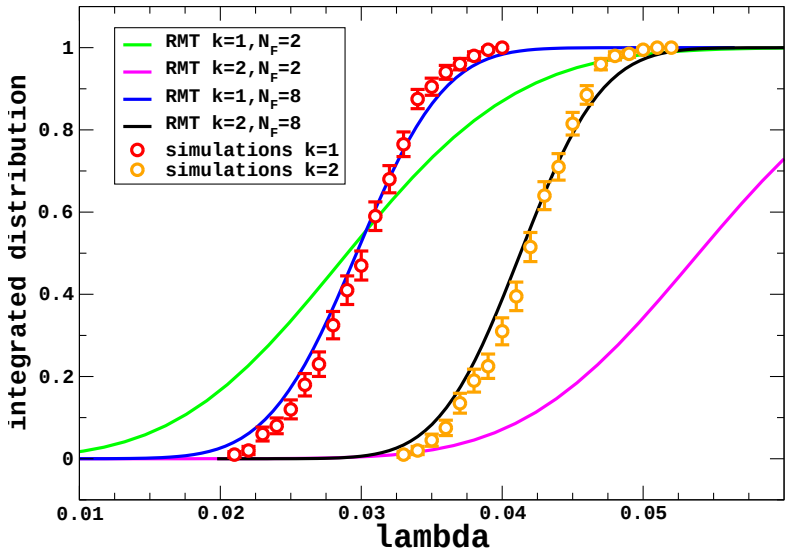

Figure 3.2: The integrated distribution of the two lowest eigenvalue quartets, from simulations of $n_s = 2$ Asqtad staggered flavors. This is compared to RMT with $N_f = 2$ and 8, corresponding to the strong and weak coupling limits.

The eigenvalue distributions in various topological sectors are measured via lattice simulations, and via comparison with RMT, the value of the condensate Σ can be extracted. This method has been successfully used in a number of lattice QCD studies, for example in dynamical overlap fermion simulations [78].

3.3 Simulations and analysis

For $SU(3)$ gauge theory with quarks in the fundamental representation, various methods suggest that the critical number of flavors separating conformal and QCD-like behavior is between 8 and 12. In order to study this interesting region, we simulate $n_s = 2$ and 3 staggered fermion flavors, corresponding to $N_f =$ 8 and 12 flavors in the continuum limit. (We do not take roots of the determinant of the staggered Dirac operator). We have also simulated $SU(3)$ gauge theory with $N_f = 2$ flavors in the 2-index symmetric representation, using dynamical overlap fermions, which is described in [79]. We use the Asqtad staggered action [80], which includes improvements to reduce the violations of flavor symmetry

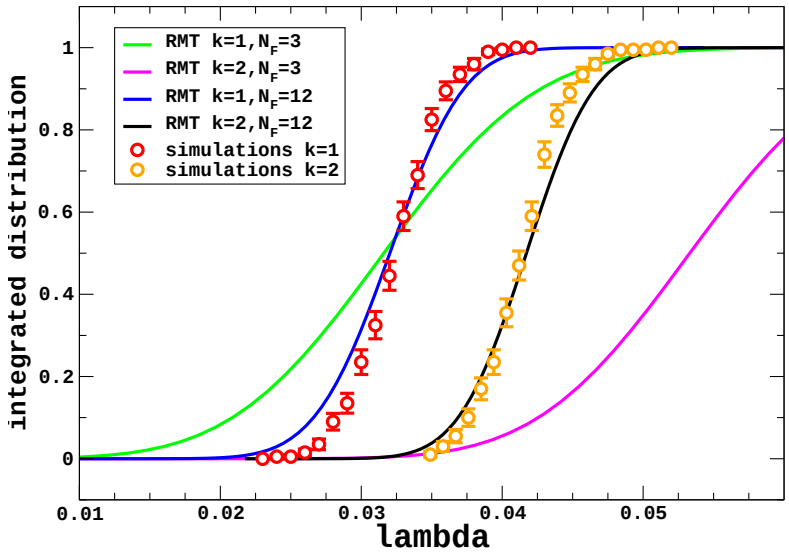

Figure 3.3: The integrated distribution of the two lowest eigenvalue quartets, from simulations of $n_s = 3$ Asqtad staggered flavors. This is compared to RMT with $N_f = 3$ and 12, corresponding to the strong and weak coupling limits.

("taste breaking") at finite lattice spacing. This action is very well tested and has been heavily used in large scale simulations of lattice QCD [81]. There have been detailed comparisons of staggered eigenvalues with the Asqtad action to RMT [82], but only in the quenched approximation.

Because $n_s = 2$ and 3 staggered flavors have not been simulated with this action before, a large scan of the parameter space of the bare couplings was required. Hence our first runs were on small volumes 10^4, where we also gained experience on the dependence of the Hybrid Monte Carlo algorithm [83] on the quark mass and the discretization of the trajectory length. Once we generated large thermalized ensembles, we calculated the lowest eigenvalues of the Dirac operator using the PRIMME package [84]. In the continuum limit, the staggered eigenvalues form degenerate quartets, with restored flavor symmetry. In Figs. 3.2 and 3.3, we show the integrated distributions of the two lowest eigenvalue quartet averages,

$$\int_0^\lambda p_k(\lambda')d\lambda', \quad k = 1, 2 \tag{3.4}$$

for ensembles with $n_s = 2$ and 3 staggered flavors respectively. Both simulations

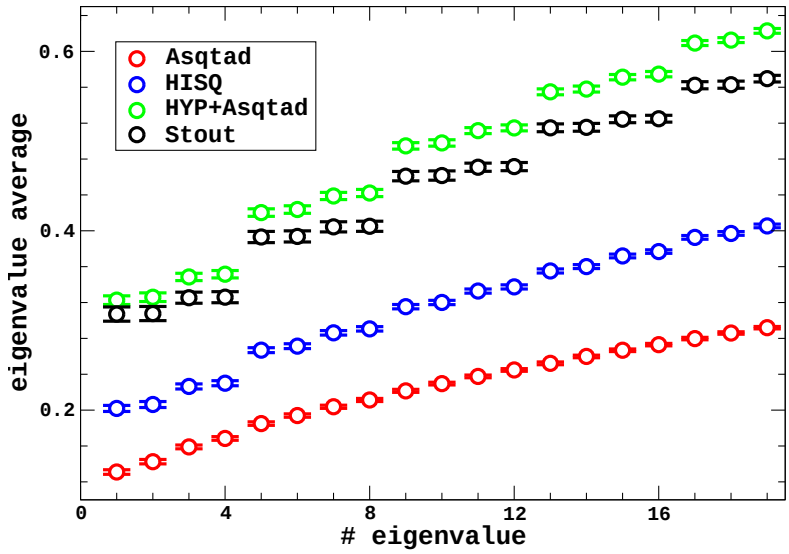

Figure 3.4: Comparison of different improvements of the staggered Dirac operator. The eigenvalues are calculated on the same ensemble of gauge configurations, which were generated using the Asqtad action.

have quark mass $ma = 0.01$, and the respective bare couplings are $\beta = 3.9$ and 1.9. All low eigenvalues have small chirality, with no indication of non-zero topology. We see that the quark mass is less than the average smallest eigenvalue, which is necessary to probe the behavior of the eigenvalue distributions in the chiral limit. To compare with RMT, we vary $\mu = m\Sigma V$ until we satisfy

$$\frac{\langle \lambda_1 \rangle_{\text{sim}}}{m} = \frac{\langle z \rangle_{\text{rmt}}}{\mu}, \tag{3.5}$$

where $\langle \lambda_1 \rangle_{\text{sim}}$ is the lowest quartet average from simulations and the RMT average $\langle z \rangle_{\text{rmt}}$ depends implicitly on μ and N_f. With this optimal value of μ, we can predict the distributions $p_k(\lambda')$ and compare to the simulations.

In both cases, we see quite good agreement between simulations and RMT with the corresponding number of flavors in the continuum limit i.e. $N_f = 8$ and 12. This is somewhat surprising. From the eigenvalues themselves, one can directly see that flavor breaking is significant, since degenerate quartets are not yet formed. A previous eigenvalue study used unimproved staggered quarks in dynamical fermion simulations [85]. They found excellent agreement with RMT but only if N_f had the same value as the number of staggered flavors n_s. We also find that, at strong

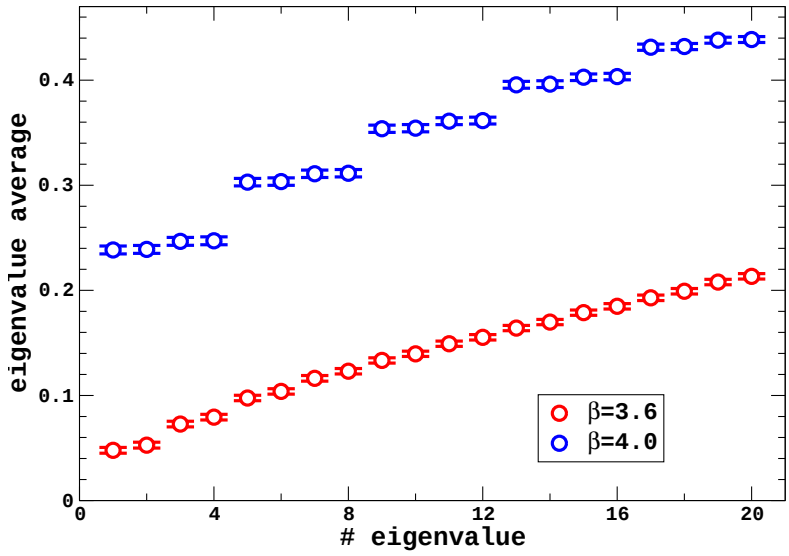

Figure 3.5: The lowest eigenvalues calculated on two ensembles with $n_s = 1$ staggered flavor, with stout smearing used both in the sea and valence quark. The lattice volume is 12^4.

coupling, RMT with the continuum value $N_f = 4n_s$ does not describe the data. On coarse lattices, the flavor breaking is very large and only one pion can be tuned to the ϵ-regime for each staggered flavor. One has to go to weak coupling and finer lattices, where flavor breaking decreases, to recover the correct number of light pions.

These results indicate that both the $N_f = 8$ and 12 flavor theories with fundamental quarks have a non-zero quark condensate Σ i.e. chiral symmetry is spontaneously broken. If this conclusion holds against further studies of flavor breaking effects, our $N_f = 8$ result will lend considerable support to the findings of [71, 73], but the $N_f = 12$ spectrum would be inconsistent with the statement of [71] that this theory is conformal.

3.4 Staggered improvement

Since flavor breaking can have a dramatic effect on the eigenvalues, we are investigating various improvements of the staggered action, to bring the simula-

tions closer to the continuum limit. In Fig. 3.4, we compare mixed actions, with gauge configurations generated using the Asqtad action, while the eigenvalues are those of various improved staggered Dirac operators. This figure is for $n_s = 1$ staggered flavor at $\beta = 6.8$ and volume 10^4. The appearance of eigenvalue quartets which are clearly separated is a clear indication of reduced flavor breaking. Both HYP-smearing [86] and stout-smearing [87] seem to bring significant improvement relative to the Asqtad operator, while HISQ fermions [88] do not show as clear an improvement.

We also show in Fig. 3.5 the effect of using stout-smearing both in the sea and valence quark. As we go to weaker coupling towards the continuum limit, the eigenvalue quartet structure emerges clearly. Comparison of the improved eigenvalues with RMT is ongoing.

3.5 Conclusions

Knowledge of the conformal window is essential to build viable candidates of strongly interacting physics beyond the Standard Model, and lattice simulations will play a crucial role. Our technique of studying the eigenvalue properties complements other lattice approaches, such as calculating the beta function of the renormalized coupling, looking for finite-temperature transitions, or extracting the mass spectrum. This will hopefully lead to consensus about the nature of these new theories. Our first study gives an indication that $SU(3)$ gauge theory with $N_f = 8$ and 12 flavors are both QCD-like, non-conformal theories. We are investigating various improvements to reduce flavor-breaking lattice artifacts and allow us to reach a stronger conclusion.

3.6 Acknowledgments

We thank Poul Damgaard for very helpful discussions, and Urs Heller who stressed the importance of reaching the quartet degeneracy limit. This research was supported by the DOE under grants DOE-FG03-97ER40546, DE-FG02-

97ER25308, by the NSF under grant 0704171, by the DFG under grant FO 502/1 and by SFB-TR/55.

Chapter 3, in full, is a reprint of the material as it appears in Proceedings of Science: Lattice 2008. Zoltan Fodor, Kieran Holland, Julius Kuti, Daniel Nogradi, and Chris Schroeder, PoS LATTICE2008, 066, 2008. The dissertation author was a principal investigator and co-author of this paper.

Chapter 4

Chiral Symmetry Breaking in Nearly Conformal Gauge Theories

Abstract

We present new results on chiral symmetry breaking in nearly conformal gauge theories with fermions in the fundamental representation of the SU(3) color gauge group. The number of fermion flavors is varied in an extended range below the conformal window with chiral symmetry breaking (χSB) for all flavors between $N_f = 4$ and $N_f = 12$. To identify χSB we apply several methods which include, within the framework of chiral perturbation theory, the analysis of the Goldstone spectrum in the p-regime and the spectrum of the fermion Dirac operator with eigenvalue distributions of random matrix theory in the ϵ-regime. Chiral condensate enhancement is observed with increasing N_f when the electroweak symmetry breaking scale F is held fixed in technicolor language. Important finite-volume consistency checks from the theoretical understanding of the $SU(N_f)$ rotator spectrum of the δ-regime are discussed. We also consider these gauge theories at $N_f = 16$ inside the conformal window. The importance of understanding finite volume, zero momentum gauge field dynamics inside the conformal window is pointed out. Staggered lattice fermions with supressed taste breaking are used throughout the simulations.

4.1 Introduction

Our goal in this work to identify chiral symmetry breaking (χSB) below the conformal window of strongly interacting gauge theories requires the application and testing of several methods in finite volumes. These include the analysis of the Goldstone spectrum in the p-regime and the spectrum of the fermion Dirac operator with eigenvalue distributions of Random Matrix Theory (RMT) in the ϵ-regime, within the framework of chiral perturbation theory (χPT). Some critical consistency checks from the theoretical understanding of the $SU(N_f)$ rotator spectrum of the δ-regime will be also discussed. We report new results with $N_f = 4, 8, 9, 12$ flavors with χSB below the conformal window for fermions in the fundamental representation of the SU(3) color gauge group. As N_f is increased, chiral condensate enhancement is observed when the electroweak symmetry breaking scale F is held fixed in technicolor language. We also discuss the theory inside the conformal window. The importance of understanding finite volume, zero momentum gauge field dynamics inside the conformal window is pointed out and illustrated at $N_f = 16$. Much of this work is an extension of our pre-conference publication [89] where we did not report our $N_f = 12$ results. In our forthcoming publication [90] more details will be provided on the analysis and results presented here.

It is an intriguing possibility that new physics beyond the Standard Model might take the form of some new strongly-interacting gauge theory building on the original technicolor idea [67, 68, 91]. This approach has lately been revived by new explorations of the multi-dimensional theory space of nearly conformal gauge theories [92, 93, 69, 94]. Model building of a strongly interacting electroweak sector requires the knowledge of the phase diagram of nearly conformal gauge theories as the number of colors N_c, number of fermion flavors N_f, and the fermion representation R of the technicolor group are varied in theory space. For fixed N_c and R the theory is in the chirally broken phase for low N_f, and asymptotic freedom is maintained with a negative β function. On the other hand, if N_f is large enough, the β function is positive for all couplings, and the theory is trivial. There is some range of N_f for which the β function might have a non-trivial zero, an infrared fixed point, where the theory is in fact conformal [95, 96]. This method

has been refined by estimating the critical value of N_f, above which spontaneous chiral symmetry breaking no longer occurs [97, 98, 99].

Interesting models require the theory to be very close to, but below, the conformal window, with a running coupling which is almost constant over a large energy range [100, 101, 102, 103, 104, 6]. The nonperturbative knowledge of the critical N_f^{crit} separating the two phases is essential and this has generated much interest and many new lattice studies [89, 105, 106, 107, 108, 109, 110, 72, 111, 71, 112, 113, 74, 114, 115, 116, 117, 118, 119, 120, 73, 70, 121, 122, 123, 124, 125, 126, 127, 128, 129, 130, 131]. To provide theoretical framework for the analysis of simulation results, we review first a series of tests expected to hold in the setting of χPT in finite volume and in the infinite volume limit.

4.2 Chiral symmetry breaking below the conformal window

We will identify in lattice simulations the chirally broken phases with $N_f = 4, 8, 9, 12$ flavors of staggered fermions in the fundamental SU(3) color representation using finite volume analysis. We deploy staggered fermions with exponential (stout) smearing [87] in the lattice action to reduce well-known cutoff effects with taste breaking in the Goldstone spectrum [132]. The presence of taste breaking requires a brief explanation of how we apply staggered χPT in our analysis. The important work of Lee, Sharpe, Aubin and Bernard [133, 134, 135] is closely followed in the discussion.

4.2.1 Staggered chiral perturbation theory

Starting with $N_f = 4$ [133], the spontaneous breakdown of $SU(4)_L \times SU(4)_R$ to vector $SU(4)$ gives rise to 15 Goldstone and pseudo-Goldstone modes, described by fields ϕ_i that can be organized into an $SU(4)$ matrix

$$\Sigma(x) = \exp\Big(i\frac{\phi}{\sqrt{2}F}\Big)\,, \qquad \phi = \sum_{a=1}^{15} \phi_a T_a\,. \tag{4.1}$$

F is the Goldstone decay constant in the chiral limit and the normalization $T_a = \{\xi_\mu, i\xi_{\mu 5}, i\xi_{\mu\nu}, \xi_5\}$ is used for the flavor generators. The leading-order chiral Lagrangian is given by

$$\mathcal{L}_\chi^{(4)} = \frac{F^2}{4}\mathsf{Tr}(\partial_\mu \Sigma \partial_\mu \Sigma^\dagger) - \frac{1}{2} B\, m_q\, F^2 \mathsf{Tr}(\Sigma + \Sigma^\dagger)\,, \tag{4.2}$$

with the fundamental parameters F and B measured on the technicolor scale $\Lambda_{\rm TC}$ which replaced $\Lambda_{\rm QCD}$ in the new theory. Expanding the chiral Lagrangian in powers of ϕ one finds 15 degenerate Goldstone pions with masses given by

$$M_\pi^2 = 2Bm_q\left[1 + O(m_q/\Lambda_{\rm TC})\right]\,. \tag{4.3}$$

The leading-order term is the tree-level result while the corrections come from loop diagrams and from higher-order terms in the chiral Lagrangian. The addition of $a^2\mathcal{L}_\chi^{(6)}$ breaks chiral symmetry and lifts the degeneracy of the Goldstone pions. Adding correction terms to Eq. (4.3) yields

$$M_\pi^2 = C(T_a)\cdot a^2\Lambda_{\rm TC}^4 + 2Bm_q\left[1 + O(m_q/\Lambda_{\rm TC}) + O(a^2\Lambda_{\rm TC}^2)\right] \tag{4.4}$$

where the representation dependent $C(T_a)$ is a constant of order unity. Contributions proportional to a^2 are due to $\mathcal{L}_\chi^{(6)}$ and lead to massive pseudo-Goldstone pions even in the $m_q \to 0$ chiral limit, except for the Goldstone pion with flavor ξ_5 which remains massless because the $U(1)_A$ symmetry is protected.

Lee and Sharpe observe that the part of $\mathcal{L}_\chi^{(6)}$ without derivatives, defining the potential $\mathcal{V}_\chi^{(6)}$, is invariant under flavor $SO(4)$ transformations and gives rise to the a^2 term in M_π^2. Terms in $\mathcal{L}_\chi^{(6)}$ involving derivatives break $SO(4)$ further down to the lattice symmetry group and give rise to non-leading terms proportional to $a^2 m$ and a^4. The taste breaking potential is given by

$$\begin{aligned}
-\mathcal{V}_\chi^{(6)} &= C_1\mathsf{Tr}(\xi_5\Sigma\xi_5\Sigma^\dagger) + \frac{C_2}{2}\left[\mathsf{Tr}(\Sigma^2) - \mathsf{Tr}(\xi_5\Sigma\xi_5\Sigma) + h.c.\right] \\
&+ \frac{C_3}{2}\sum_\nu\left[\mathsf{Tr}(\xi_\nu\Sigma\xi_\nu\Sigma) + h.c.\right] + \frac{C_4}{2}\sum_\nu\left[\mathsf{Tr}(\xi_{\nu 5}\Sigma\xi_{5\nu}\Sigma) + h.c.\right] \\
&+ \frac{C_5}{2}\sum_\nu\left[\mathsf{Tr}(\xi_\nu\Sigma\xi_\nu\Sigma^\dagger) - \mathsf{Tr}(\xi_{\nu 5}\Sigma\xi_{5\nu}\Sigma^\dagger)\right] \\
&+ C_6\sum_{\mu<\nu}\mathsf{Tr}(\xi_{\mu\nu}\Sigma\xi_{\nu\mu}\Sigma^\dagger).
\end{aligned} \tag{4.5}$$

The six unknown coefficients C_i are all of size $\Lambda_{\rm TC}^6$.

In the continuum, the Goldstone pions form a 15-plet of flavor $SU(4)$ and are degenerate. On the lattice, states are classified by the symmetries of the transfer matrix, and the pseudo-Goldstone pions fall into 7 irreducible representations: four 3-dimensional representations with flavors ξ_i, ξ_{i5}, ξ_{ij} and ξ_{i4}, and three 1-dimensional representations with flavors ξ_4, ξ_{45} and ξ_5.

Close to both the chiral and continuum limits, the pseudo-Goldstone masses are given by

$$M_\pi(T_a)^2 = 2Bm_q + a^2\Delta(T_a) + O(a^2 m_q) + O(a^4)\,, \tag{4.6}$$

with $\Delta(T_a) \sim \Lambda_{\rm TC}^4$ arising from $\mathcal{V}_\chi^{(6)}$. Since $\mathcal{V}_\chi^{(6)}$ respects flavor $SO(4)$, the 15 Goldstone particles fall into $SO(4)$ representations:

$$\begin{aligned}
&\Delta(\xi_5) = 0,\\
&\Delta(\xi_\mu) = \frac{8}{F^2}(C_1 + C_2 + C_3 + 3C_4 + C_5 + 3C_6),\\
&\Delta(\xi_{\mu 5}) = \frac{8}{F^2}(C_1 + C_2 + 3C_3 + C_4 - C_5 + 3C_6),\\
&\Delta(\xi_{\mu\nu}) = \frac{8}{F^2}(2C_3 + 2C_4 + 4C_6).
\end{aligned} \tag{4.7}$$

In the chiral limit at finite lattice spacing, the lattice irreducible representations with flavors ξ_i and ξ_4 are degenerate, those with flavors ξ_{i5} and ξ_{45}, and those with flavors ξ_{ij} and ξ_{i4} are degenerate as well. No predictions can be made for the ordering, splittings, or even the *signs* of the mass shifts. Our simulations indicate that they are all positive with the exponentially smeared staggered action we use, making the existence of an Aoki phase [133] unlikely. The method of [133] has been generalized to the $N_f > 4$ case [134, 135] which we adopted in our calculations with help from Bernard and Sharpe. The procedure cannot be reviewed here but it will be used in the interpretation of our $N_f = 8$ simulations.

4.2.2 Finite volume analysis in the p-regime

Three different regimes can be selected in simulations to identify the chirally broken phase from finite volume spectra and correlators. For a lattice size $L_s^3 \times L_t$ in

euclidean space and in the limit $L_t \gg L_s$, the conditions $F_\pi L_s > 1$ and $M_\pi L_s > 1$ select the the p-regime, in analogy with low momentum counting [136, 137].

For arbitrary N_f, in the continuum and in infinite volume, the one-loop chiral corrections to M_π and F_π of the degenerate Goldstone pions are given by

$$M_\pi^2 = M^2\left[1 - \frac{M^2}{8\pi^2 N_f F^2} ln\left(\frac{\Lambda_3}{M}\right)\right], \tag{4.8}$$

$$F_\pi = F\left[1 + \frac{N_f M^2}{16\pi^2 F^2} ln\left(\frac{\Lambda_4}{M}\right)\right], \tag{4.9}$$

where $M^2 = 2B \cdot m_q$ and $F, B, \Lambda_3, \Lambda_4$ are four fundamental parameters of the chiral Lagrangian, and the small quark mass m_q explicitly breaks the symmetry [138]. The chiral parameters F, B appear in the leading part of the Lagrangian in Eq. (4.2), while Λ_3, Λ_4 enter in next order. There is the well-known GMOR relation $\Sigma_{cond} = BF^2$ in the $m_q \to 0$ limit for the chiral condensate per unit flavor [139]. It is important to note that the one-loop correction to the pion coupling constant F_π is enhanced by a factor N_f^2 compared to M_π^2. The chiral expansion for large N_f will break down for F_π much faster for a given M_π/F_π ratio. The NNLO terms have been recently calculated [140] showing potentially dangerous N_f^2 corrections to Eqs. (4.8,4.9).

The finite volume corrections to M_π and F_π are given in the p-regime by

$$M_\pi(L_s, \eta) = M_\pi\left[1 + \frac{1}{2N_f}\frac{M^2}{16\pi^2 F^2} \cdot \widetilde{g}_1(\lambda, \eta)\right], \tag{4.10}$$

$$F_\pi(L_s, \eta) = F_\pi\left[1 - \frac{N_f}{2}\frac{M^2}{16\pi^2 F^2} \cdot \widetilde{g}_1(\lambda, \eta)\right], \tag{4.11}$$

where $\widetilde{g}_1(\lambda, \eta)$ describes the finite volume corrections with $\lambda = M \cdot L_s$ and aspect ratio $\eta = L_t/L_s$. The form of $\widetilde{g}_1(\lambda, \eta)$ is a complicated infinite sum which contains Bessel functions and requires numerical evaluation [137]. Eqs. (4.8-4.11) provide the foundation of the p-regime fits in our simulations.

4.2.3 δ-regime and ϵ-regime

At fixed L_s and in cylindrical geometry $L_t/L_s \gg 1$, a crossover occurs from the p-regime to the δ-regime when $m_q \to 0$, as shown in Fig. 4.1. The dynamics is

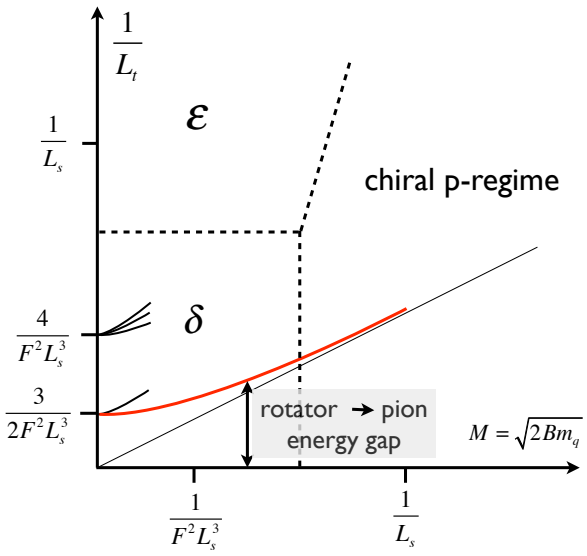

Figure 4.1: Schematic plot of the regions in which the three low energy chiral expansions are valid. The vertical axis shows the finite temperature scale (euclidean time in the path integral) which probes the rotator dynamics of the δ-regime and the ϵ-regime. The first two low lying rotator levels are also shown on the vertical axis for the simple case of $N_f = 2$. The fourfold degenerate lowest rotator excitation at $m_q = 0$ will split into an isotriplet state (lowest energy level), which evolves into the p-regime pion as m_q increases, and into an isosinglet state representing a multi-pion state in the p-regime. Higher rotator excitations have similar interpretations.

dominated by the rotator states of the chiral condensate in this limit [141] which is characterized by the conditions $FL_s > 1$ and $ML_s \ll 1$. The densely spaced rotator spectrum scales with gaps of the order $\sim 1/F^2L_s^3$, and at $m_q = 0$ the chiral symmetry is apparently restored. However, the rotator spectrum, even at $m_q = 0$ in the finite volume, will signal that the infinite system is in the chirally broken phase for the particular parameter set of the Lagrangian. This is often misunderstood in the interpretation of lattice simulations. Measuring finite energy levels with pion quantum numbers at fixed L_s in the $m_q \to 0$ limit is not a signal for chiral symmetry restoration of the infinite system [118].

If $L_t \sim L_s$ under the conditions $FL_s > 1$ and $ML_s \ll 1$, the system will be driven into the ϵ-regime which can be viewed as the high temperature limit of the δ-regime quantum rotator. Although the δ-regime and ϵ-regime have an overlapping region, there is an important difference in their dynamics. In the δ-

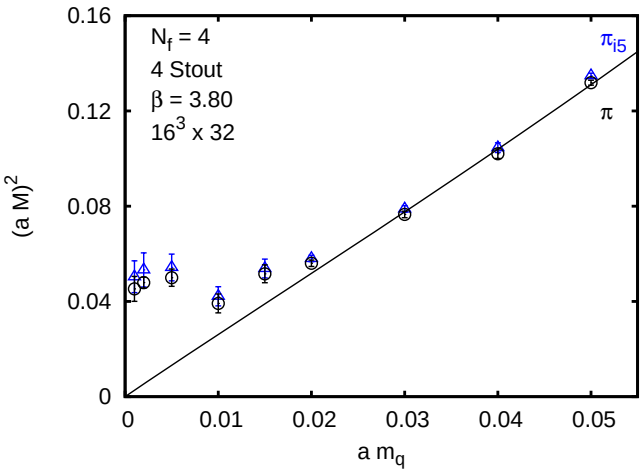

Figure 4.2: The crossover from the p-regime to the δ-regime is shown for the π and π_{i5} states at $N_f = 4$.

regime of the quantum rotator, the mode of the pion field $U(x)$ with zero spatial momentum dominates with time-dependent quantum dynamics. The ϵ-regime is dominated by the four-dimensional zero momentum mode of the chiral Lagrangian.

We report simulation results of all three regimes in the chirally broken phase of the technicolor models we investigate. The analysis of the three regimes complement each other and provide cross-checks for the correct identification of the phases. First, we will probe Eqs. (4.8-4.11) in the p-regime, and follow with the study of Dirac spectra and RMT eigenvalue distributions in the ϵ-regime. The spectrum in the δ-regime is used as a signal to monitor p-regime spectra as m_q decreases. Fig. 4.2 is an illustrative example of this crossover in our simulations. It is important to note that the energy levels in the chiral limit do not match the rotator spectrum at the small $F \cdot L_s$ values of the simulations. This squeezing with $F \cdot L_s$ not large enough for undistorted, finite volume, chiral behavior in the p-regime, ϵ-regime, and δ-regime, will be further discussed in our p-regime simulations presented next. We will also describe some methods to put this squeezing into a more quantitative context.

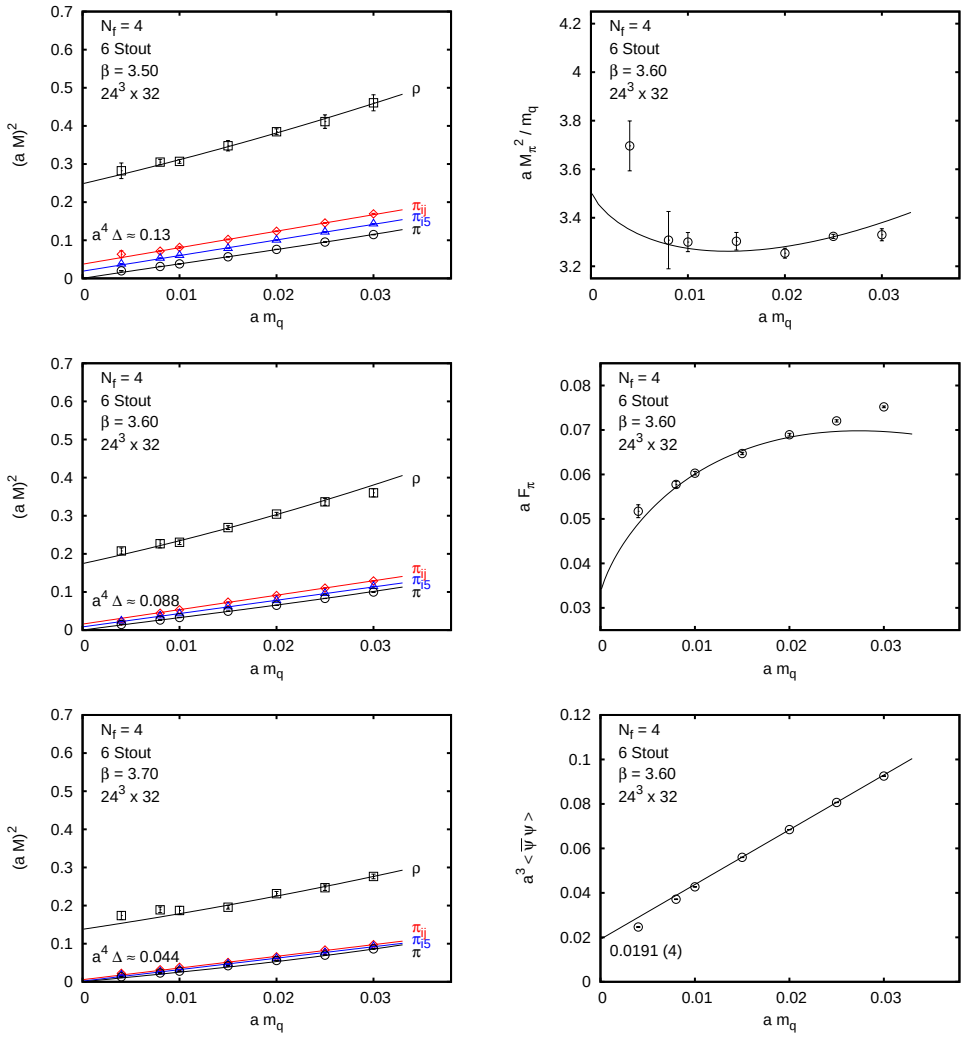

Figure 4.3: The Goldstone spectrum and chiral fits are shown for simulations with lattice size $24^3 \times 32$. The left column shows the pseudo-Goldstone spectrum with decreasing taste breaking as the gauge coupling is varied from $\beta = 3.5$ to $\beta = 3.7$. The middle value at $\beta = 3.6$ was chosen for chiral fits which are shown in the right column. The top right figure with fitting range $a \cdot m_q = 0.008 - 0.025$ shows the NLO chiral fit to M_π^2/m_q which approaches $2B$ in the chiral limit. Data points below $m_q = 0.008$ are not in the chiral p-regime and not used in the fitting procedure.The middle figure on the right is the NLO chiral fit to F_π in the range $a \cdot m_q = 0.008 - 0.02$. The bottom right figure is the linear fit to the chiral condensate with fitting range $a \cdot m_q = 0.015 - 0.025$. The physical fit parameters $B, F, \Lambda_3, \Lambda_4$ are discussed in the text.

4.3 P-regime Goldstone spectra at $N_f = 4$

In this section we describe in some detail the methods we use for successfully testing chiral symmetry breaking. Our tests in the p-regime have two major com-

ponents. The primary test is to identify the pseudo-Goldstone spectrum of the staggered formulation with evidence for recovery from taste symmetry breaking close to the continuum limit. The secondary test is to probe chiral loop corrections to the tree-level behavior of M_π^2 and F_π as the fermion mass $a \cdot m_q$ is varied at fixed gauge coupling β. The evidence we find for chiral symmetry breaking at $N_f = 4, 8, 9, 12$ is common to all flavors. Limitations and ambiguities identified at $N_f = 4$ for future improvements are expected to be more pronounced with increasing N_f. Results for each flavor we have simulated in the p-regime are presented in separate sections beginning here with general discussion and $N_f = 4$ results.

We have used the tree-level Symanzik-improved gauge action for all simulations. The conventional $\beta = 6/g^2$ lattice gauge coupling is defined as the overall factor in front of the three well-known terms of the lattice action. The link variables in the staggered fermion matrix were exponentially smeared with six stout steps at $N_f = 4$ and the RHMC algorithm was deployed in all runs. The results shown in Fig. 4.3 are from the p-regime of χSB with the conditions $M_\pi \cdot L_s \gg 1$ and $F_\pi \cdot L_s \sim 1$ when the chiral condensate begins to follow the expected behavior of infinite-volume chiral perturbation theory from Eqs. (4.8,4.9) in next-to-leading order (NLO) with calculable finite volume corrections from Eqs. (4.10,4.11) which are negligible at $L_s = 24$. We have empirical evidence that the M_π and F_π data points are free of finite volume corrections in practically the entire fitting range of the fermion masses we use at $L_s = 24$ so that the negligible corrections from Eqs. (4.10,4.11) can be ignored.

Within some finite volume limitations, which we will address, the $N_f = 4$ simulations work in the p-regime as expected. The left column of Fig. 4.3 shows that the pseudo-Goldstone spectrum clearly remains separated from the hadronic scale of the ρ-meson as β is varied. Moving towards the continuum limit with increasing β, we see the split pseudo-Goldstone spectrum collapsing into the degenerate continuum pion spectrum. The true Goldstone pion whose mass will vanish in the $a \cdot m_q = 0$ limit at fixed lattice spacing and two additional split states with small residual masses at $a \cdot m_q = 0$ are shown to illustrate the trend. $a^4\Delta$ is the measure of the small taste breaking in quadratic mass splitting as measured in

lattice units. The origin of the splittings and the quantum numbers were discussed in Section 4.2 as shown in Eq. (4.7). The spectrum is approximately parallel as the bare fermion mass $a \cdot m_q$ is varied at fixed lattice spacing and the gaps appear to be equally spaced to a good approximation, consistent with earlier observations in QCD where the C_4 term seems to dominate staggered taste breaking for two light flavors with equally spaced pseudo-Goldstone levels [133]. We selected $\beta = 3.6$ for testing χPT of finite volume Goldstone dynamics in the p-regime. This choice with small taste breaking is close to the continuum limit without excessive squeeze on the important product $F \cdot L_s$ which in an ideal simulation of the p-regime should be large (F is the chiral limit of F_π as $a \cdot m_q \to 0$ at fixed lattice spacing).

The simultaneous chiral fit of M_π^2/m_q and F_π based on Eqs. (4.8-4.11) is shown in Fig. 4.3 where chiral loops correct the tree-level values of $M_\pi^2/m_q = 2B$ and F_π. In the fitting range $a \cdot m_q = 0.008 - 0.025$ applied to M_π^2/m_q we observe small corrections to the tree-level value of $2B$ which keeps the fit well within the range of one-loop χPT. In the fitting range $a \cdot m_q = 0.008 - 0.02$ the F_π data are about a factor of two larger than F which indicates how the one-loop fit is being pushed to its limits. Without loop correction F_π would not change from its fitted value of $a \cdot F = 0.033(4)$ in the chiral limit at fixed lattice spacing. The fitted value of B is $a \cdot B = 1.76(7)$ in lattice units and $M_\rho/F = 13(1)$ in the chiral limit (the linear fit of $M_\rho = \mathrm{c} + \mathrm{d} \cdot \mathrm{m_q}$ is used at all N_f values to determine $M_\rho(\mathrm{m_q} = 0)$). The fitted value of $B/F = 53(6)$ indicates significant enhancement of the chiral condensate from its $N_f = 2$ value [128, 142]. In our simultaneous fits we get $\Lambda_3 = 0.37(5)$ and $\Lambda_4 = 0.51(1)$ which set the chiral couplings in the NLO chiral Lagrangian.

The chiral condensate $\langle\overline{\psi}\psi\rangle$ summed over all flavors is dominated by the linear term in m_q from UV contributions. The linear fit gives $\langle\overline{\psi}\psi\rangle = 0.0191(4)$ in the chiral limit which differs from the GMOR relation of $\langle\overline{\psi}\psi\rangle = 4F^2B$ by about a factor of two with $4F^2B = 0.008(2)$ fitted. There are several sources of this disagreement. The chiral log in $\langle\overline{\psi}\psi\rangle$ will bring further down the true fitted value in the chiral limit. Our volumes are not large enough yet to attempt a sensible chiral log fit to the condensate at small $a \cdot m_q$ values. Finite volume squeezing

effects distort the consistency of the results in our limited range of simulation volumes. The choice of fitting method to Eqs. (4.8,4.9) can also have some effect on the results. On the right-hand sides of the equations, the variable pair $(M,\ F)$ in the chiral logs can be replaced with the pair $(M_\pi,\ F_\pi)$ which is equivalent to a partial resummation [142]. This will be reported in our more detailed forthcoming journal publication [90].

Finite volume limitations when measured in F units have the biggest effect on our chiral analysis. The value $F \cdot L_s \approx 0.8$ is not expected to protect against significant finite-volume squeezing effects for even the largest spatial size $L_s = 24$ used in the chiral fits at $N_f = 4$. Larger than optimal NLO corrections in the chiral fits of F_π and finite-volume squeezing effects are closely related concerns. Simulations on larger lattices would increase $F \cdot L_s$ and allow us to drop back in $a \cdot m_q$ into a more comfortable range with smaller NLO chiral corrections for F_π.

Finite volume corrections to the rotator spectrum in the δ-regime set some quantitative measure of squeezing effects on the chiral analysis. The connection is made by observing that the pion spectrum in the p-regime can be viewed at fixed spatial volume L_s^3 as the adiabatic evolution from the energy levels of the rotator spectrum of the δ-regime as illustrated schematically in Fig. 4.2 for the lowest $N_f = 2$ rotator levels. The rotator spectrum for $N_f = 2$ is given by $E_l = \frac{1}{2\Theta} l(l+2)$, with $l = 0, 1, 2, ...$, where the moment of inertia is calculated in NLO [143, 144] as $\Theta = F^2 L_s^3 (1 + \frac{C(N_f=2)}{F^2 L_s^2} + O(\frac{1}{F^4 \cdot L_s^4}))$. The value of $C(N_f = 2)$ is known to be 0.45 and is expected to grow with N_f. At $F \cdot L_s \approx 0.8$ the correction is 70% for $N_f = 2$ and probably considerably larger for $N_f = 4$. The leading-order rotator gap for arbitrary N_f is given by $E_1 - E_0 = \frac{N_f^2 - 1}{N_f F^2 L_s^3}$ but the coefficient $C(N_f)$ is an important missing piece in the analysis. Were we to continue the p-regime Goldstone spectrum at $N_f = 4$, $L_s = 24$, and $\beta = 3.6$ to the δ-regime adiabatically, the small value of $F \cdot L_s$ would not allow us to get a reliable estimate of F based on the chiral rotator spectrum with the collapse of the adiabatic approximation. This is a quantitative warning sign of the need for considerably larger spatial volume for robust p-regime results to determine F in the chiral fitting procedure. In fact, we are going to fit M_π^2/m_q in the chiral analysis for $N_f = 8, 9, 12$ with

better controlled NLO loop corrections, but F_π will not be fitted. For larger N_f, a reliable simultaneous fit requires substantially larger volumes than are realistic with our current resources.

In summary, the $N_f = 4$ system passed both tests in the chirally broken phase and shows significant enhancement of the chiral condensate when measured in units of the electroweak symmetry breaking scale set by F. This is a relevant effect to monitor for fermion mass generation in extended technicolor applications as we begin to approach the conformal window [128].

4.4 P-regime Goldstone spectra at $N_f = 8$

As we move to the $N_f = 8$ p-regime simulations, we can clearly identify the p-regime of the chirally broken phase as summarized in Fig. 4.4. The same lattice action and algorithm was used for the $N_f = 8$ p-regime simulations as introduced earlier for $N_f = 4$. We can clearly identify the pseudo-Goldstone spectrum which is separated from the technicolor scale of the ρ-meson. Moving towards the continuum limit we observe at $\beta = 1.4$ the split pion spectrum collapsing toward the true Goldstone pion with a new distinct feature. The true Goldstone pion, whose mass will vanish in the $a \cdot m_q = 0$ limit at fixed lattice spacing, and two additional split pseudo-Goldstone states appear with considerably different slopes in Fig. 4.4 as m_q increases. For small $a \cdot m_q$ we find the pseudo-Goldstone spectrum collapsed at fixed gauge coupling. Apparently the NLO operators, the last two terms in Eq. (4.6), have a stronger effect on the spectra relative to leading-order taste breaking operators, the generalization of those from $N_f = 4$ to $N_f = 8$ as discussed in Section 2. This somewhat unexpected and unexplained trend is observed for $N_f > 8$ as well.

We analyzed the χSB pattern within staggered perturbation theory in its generalized form beyond four flavors [134, 135]. The simultaneous chiral fit of M_π^2/m_q and F_π based on Eqs. (4.8-4.11) cannot be done at $N_f = 8$ within the reach of the largest lattice sizes we deploy since the value of $F \cdot L_s$ is too small even at $L_s = 24$, for gauge couplings where taste breaking drops to an acceptable

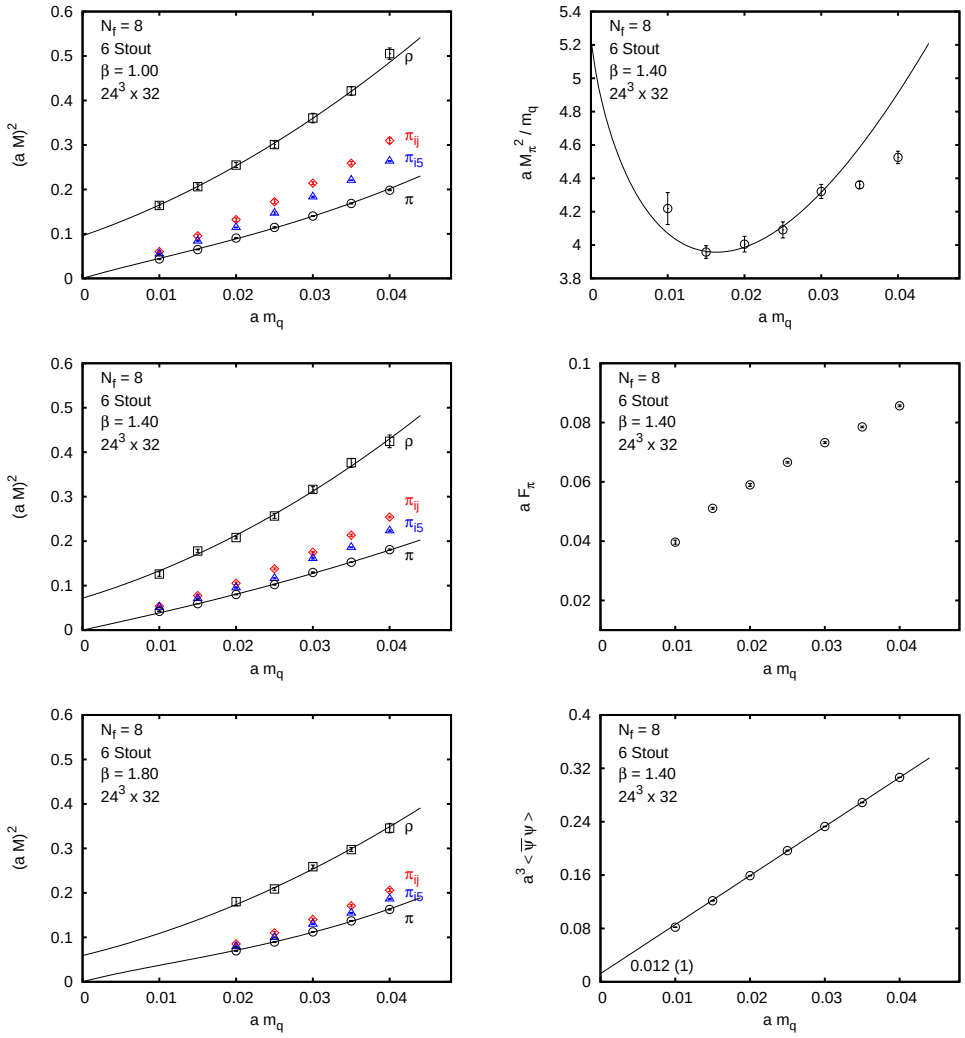

Figure 4.4: The Goldstone spectrum and chiral fits are shown for $N_f = 8$ simulations with lattice size $24^3 \times 32$. The left column shows the pseudo-Goldstone spectrum with decreasing taste breaking as the gauge coupling is varied from $\beta = 1.0$ to $\beta = 1.8$. The middle value at $\beta = 1.4$ was chosen in the top right figure with fitting range $a \cdot m_q = 0.015 - 0.03$ of the NLO chiral fit to M_π^2/m_q which approaches $2B$ in the chiral limit. The middle figure on the right shows the F_π data with no NLO fit far away from the chiral limit. The bottom right figure is the linear fit to the chiral condensate with fitting range $a \cdot m_q = 0.02 - 0.04$. The physical fit parameters B, F, Λ_3 are discussed in the text.

level. The chiral fit of B, F, Λ_3 to M_π^2/m_q, shown at the top right of Fig. 4.4, is based on Eq. (4.8) only since the F_π data points are outside the convergence range of the chiral expansion. Much larger lattices are required to drop down in m_q

to the region where the simultaneous fit could be made, while maintaining some control over finite volume and taste breaking effects. The finite volume corrections were negligible in the fitted $a \cdot m_q$ range and Eqs. (4.10,4.11) were not needed.

At $\beta = 1.4$ the fitted value of B is $a \cdot B = 2.6(3)$ in lattice units with $a \cdot F = 0.0166(9)$ and $a \cdot \Lambda_3 = 0.48(5)$ also fitted. The fitted ρ-mass in the chiral limit is $a \cdot M_\rho = 0.27(2)$ with $M_\rho/F = 17(1)$. The fitted value of $B/F = 158(17)$ is not very reliable but indicates significant enhancement of the chiral condensate from its $N_f = 4$ value without including renormalization scale effects. The chiral condensate $\langle\overline{\psi}\psi\rangle$ summed over all flavors is dominated by the linear term in m_q from UV contributions. The linear fit gives $\langle\overline{\psi}\psi\rangle = 0.012(1)$ in the chiral limit which differs from the GMOR relation of $\langle\overline{\psi}\psi\rangle = 8F^2B$ by about a factor of two with $8F^2B = 0.0058(8)$ fitted. There are several sources of this disagreement which were addressed for the $N_f = 4$ case earlier. The chiral log in $\langle\overline{\psi}\psi\rangle$ will bring further down the true fitted value in the chiral limit. Our volumes are not large enough yet to attempt a sensible chiral log fit to the condensate at small $a \cdot m_q$ values. Finite volume squeezing effects distort the consistency of the results in our limited range of simulation volumes. Similar observations should also be noted when the RMT analysis is applied in the ϵ-regime.

4.5 P-regime Goldstone spectra at $N_f = 9$

We had two motivations for the $N_f = 9$ simulation reported here. We wanted to see whether the rooting procedure (being applied in our project with two fermions in the sextet representation) will present some unexpected changes in the analysis and we were also looking for the continued trends in the χSB pattern. We could not find any noticeable effect from the rooting procedure and the symmetry breaking pattern was consistent with the $N_f = 8$ simulations.

As shown in Fig. 4.5 the Goldstone spectrum is still clearly separated from the technicolor scale of the ρ-meson. The true Goldstone pion and two additional split pseudo-Goldstone states are shown again with different slopes as $a \cdot m_q$ increases. The trends and the underlying explanation are similar to the $N_f = 8$

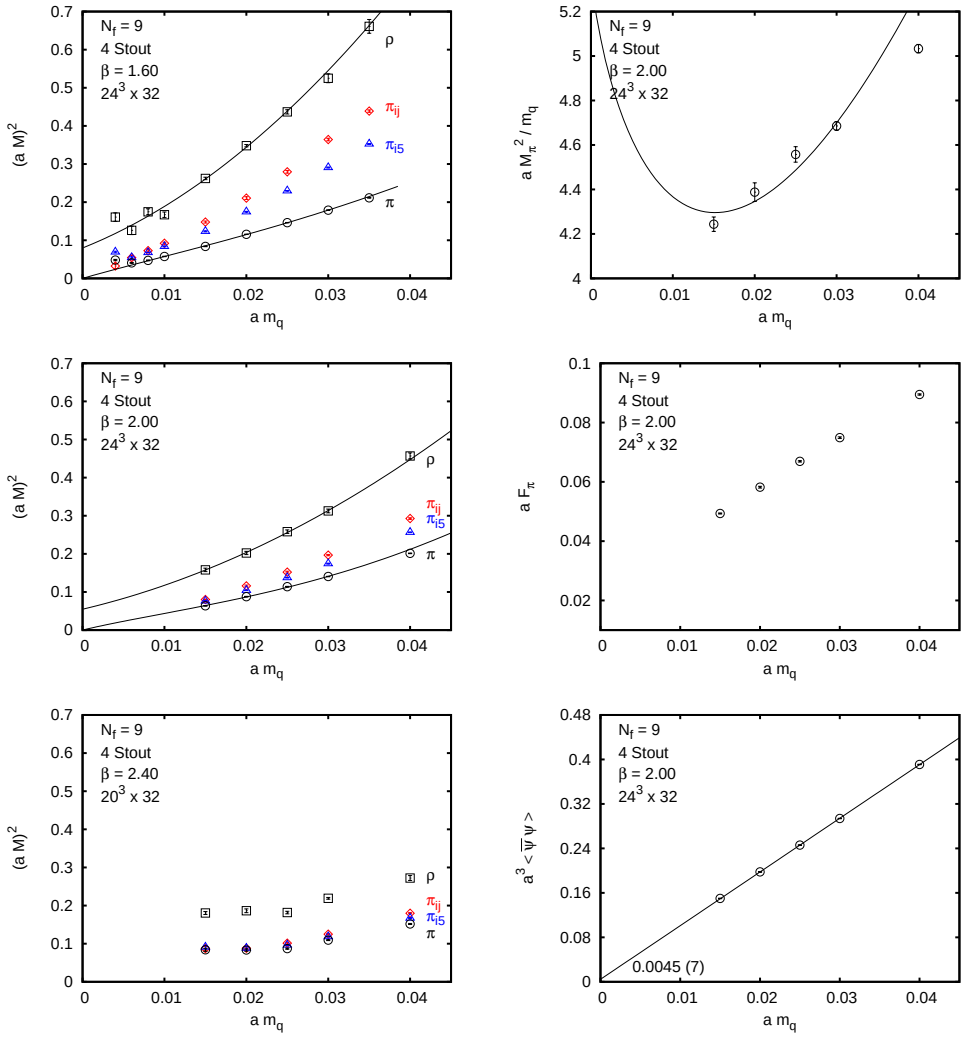

Figure 4.5: The pseudo-Goldstone spectrum and chiral fits are shown for $N_f = 9$ simulations with lattice size $24^3 \times 32$. The left column shows the pseudo-Goldstone spectrum with decreasing taste breaking as the gauge coupling is varied from $\beta = 1.6$ to $\beta = 2.4$. Although the bottom figure on the left at $\beta = 2.4$ illustrates the continued restoration of taste symmetry, the volume is too small for the Goldstone spectrum. The middle value at $\beta = 2.0$ was chosen in the top right figure with fitting range $a \cdot m_q = 0.015 - 0.03$ of the NLO chiral fit to M_π^2/m_q which approaches $2B$ in the chiral limit. The middle figure on the right shows the F_π data with no NLO fit far away from the chiral limit. The bottom right figure is the linear fit to the chiral condensate with fitting range $a \cdot m_q = 0.02 - 0.04$. The physical fit parameters B, F, Λ_3 are discussed in the text. Four stout steps were used in all $N_f = 9$ simulations.

case. The chiral fit to M_π^2/m_q is shown based on Eq. (4.8) only since the F_π data points are outside the convergence range of the chiral expansion. At $\beta = 2.0$ the fitted value of B is $a \cdot B = 2.8(4)$ in lattice units with $a \cdot F = 0.017(2)$ and $a \cdot \Lambda_3 = 0.48(9)$ also fitted. The fitted ρ-mass in the chiral limit is $a \cdot M_\rho = 0.233(3)$ with $M_\rho/F = 14(1)$. The fitted value of $B/F = 166(32)$ is not very reliable but comparable to the enhancement of the chiral condensate found at $N_f = 8$ without including renormalization scale effects. Again, at fixed lattice spacing, the small chiral condensate $\langle\overline{\psi}\psi\rangle$ summed over all flavors is dominated by the linear term in m_q from UV contributions. The linear fit gives $\langle\overline{\psi}\psi\rangle = 0.0045(7)$ in the chiral limit which differs from the GMOR relation of $\langle\overline{\psi}\psi\rangle = 9F^2B$ by about a factor of two with $9F^2B = 0.007(2)$ fitted. Open issues in the systematics are similar to the $N_f = 8$ case.

4.6 P-regime Goldstone spectra at $N_f = 12$

Finally we move to the controversial $N_f = 12$ case. We find here a similar chiral symmetry breaking pattern as we found in the $N_f = 8, 9$ cases with increased concerns about all the caveats presented before. The Goldstone spectrum remains separated from the technicolor scale of the ρ-meson. The true Goldstone pion and two additional split pseudo-Goldstone states are shown again in Fig. 4.6 with different slopes as $a \cdot m_q$ increases. The trends and the underlying explanation are similar to the $N_f = 8, 9$ cases. The chiral fit to M_π^2/m_q shown at the top right side of Fig. 4.6 is based on Eq. (4.8) only since the F_π data points are outside the convergence range of the chiral expansion. At $\beta = 2.2$ the fitted value of B is $a \cdot B = 2.7(2)$ in lattice units with $a \cdot F = 0.0120(1)$ and $a \cdot \Lambda_3 = 0.50(3)$ also fitted. The fitted ρ-mass in the chiral limit is $a \cdot M_\rho = 0.115(15)$ from $a \cdot m_q = 0.025 - 0.045$ with $M_\rho/F = 10(1)$. The fitted value of $B/F = 223(17)$ is not very reliable but consistent with the enhancement of the chiral condensate found at $N_f = 8, 9$ without including renormalization scale effects. Again, at fixed lattice spacing, the small chiral condensate $\langle\overline{\psi}\psi\rangle$ summed over all flavors is dominated by the linear term in m_q from UV contributions. The linear fit gives $\langle\overline{\psi}\psi\rangle = 0.0033(13)$ in the

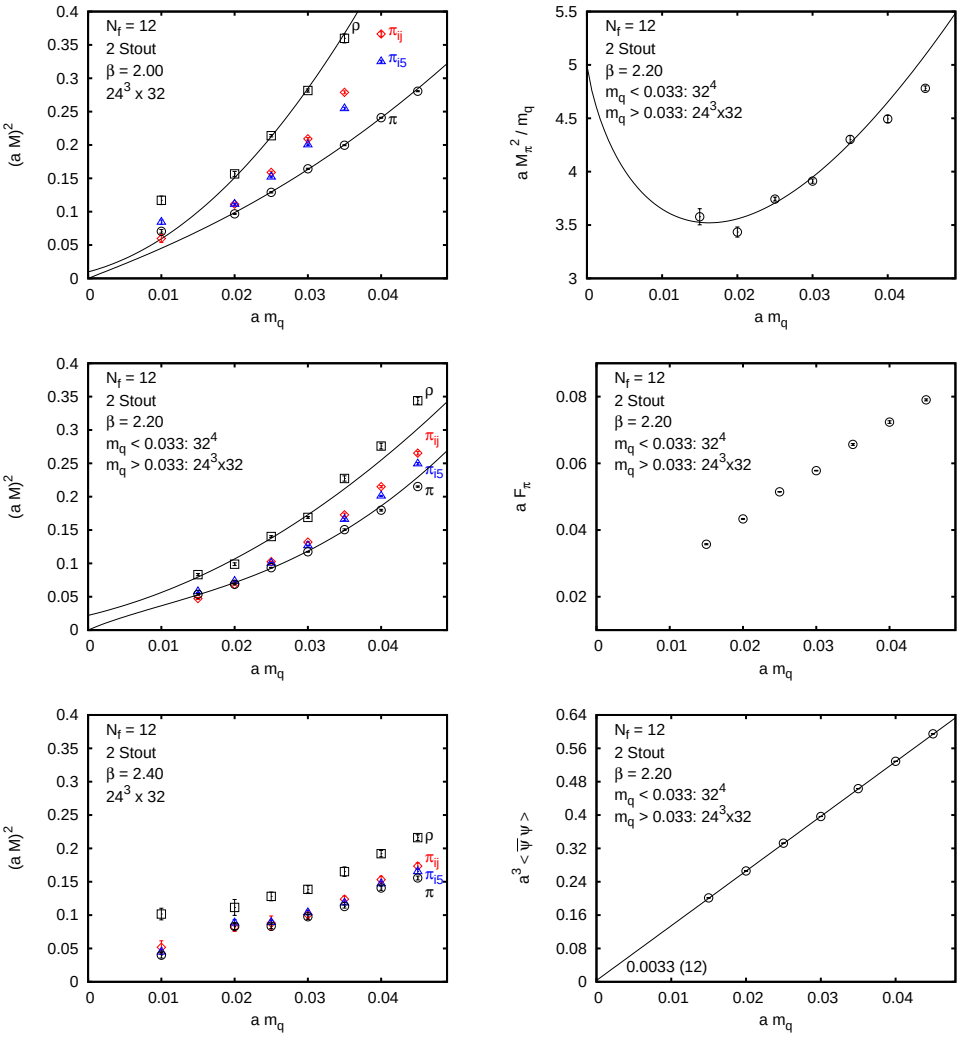

Figure 4.6: The pseudo-Goldstone spectrum and chiral fits are shown for $N_f = 12$ simulations with lattice size $24^3 \times 32$ and 32^4. The left column shows the pseudo-Goldstone spectrum with decreasing taste breaking as the gauge coupling is varied from $\beta = 2.0$ to $\beta = 2.4$. Although the bottom figure on the left at $\beta = 2.4$ illustrates the continued restoration of taste symmetry, the volume is too small for the Goldstone spectrum. The middle value at $\beta = 2.2$ was chosen in the top right figure with fitting range $a \cdot m_q = 0.015 - 0.035$ of the NLO chiral fit to M_π^2/m_q which approaches $2B$ in the chiral limit. The middle figure on the right shows the F_π data with no NLO fit far away from the chiral limit. The bottom right figure, with its additional features discussed in the text, is the linear fit to the chiral condensate with fitting range $a \cdot m_q = 0.02 - 0.04$. The physical fit parameters B, F, Λ_3 are discussed in the text. Two stout steps were used in all $N_f = 12$ simulations.

chiral limit which came out unexpectedly close the GMOR relation of $\langle\overline{\psi}\psi\rangle = 12F^2B$ with $12F^2B = 0.0046(4)$ fitted. Issues and concerns in the systematics are similar to the $N_f = 8, 9$ cases.

In summary, we have shown strong evidence that according to p-regime tests the $N_f = 4, 8, 9, 12$ systems all exhibit in the Goldstone and hadron spectra broken chiral symmetry close to the continuum limit. There are some important features of the $N_f = 12$ analysis which suggest that the model is not only in the χSB phase but also close to slow walking of the renormalized gauge coupling. The bottom right of Fig. 4.6 shows the crossover in the chiral condensate from strong coupling to the weak coupling regime in the relevant range of m_q. In combination with the nearly degenerate Goldstone spectrum we find it quite suggestive that around $\beta = 2.2$ we are close to continuum behavior. In addition, we observe that the fitted value of the ρ-mass in the chiral limit hardly changes in this region as the gauge coupling is varied (at $\beta = 2.0$ we fit $a \cdot M_\rho = 0.123(10)$). If confirmed on larger lattices, this could be a first hint of a slowly changing gauge coupling close to the conformal window. Currently we are investigating the important $N_f = 12$ model on larger lattices to probe the possible influence of unwanted squeezing effects on the spectra.

Our findings at $N_f = 12$ are in disagreement with [128]. Lessons from the Dirac spectra and RMT to complement p-regime tests are discussed in the next section.

4.7 Epsilon regime, Dirac spectrum and RMT

If the bare parameters of a gauge theory are tuned to the ϵ-regime in the chirally broken phase, the low-lying Dirac spectrum follows the predictions of random matrix theory. The corresponding random matrix model is only sensitive to the pattern of chiral symmetry breaking, the topological charge and the rescaled fermion mass once the eigenvalues are also rescaled by the same factor $\Sigma_{cond}V$. This idea has been confirmed in various settings both in quenched and fully dynamical simulations. The same method is applied here to nearly conformal gauge

models.

The connection between the eigenvalues λ of the Dirac operator and chiral symmetry breaking is given in the Banks-Casher relation [75],

$$\Sigma_{cond} = -\langle\overline{\Psi}\Psi\rangle = \lim_{\lambda\to 0}\lim_{m\to 0}\lim_{V\to\infty}\frac{\pi\rho(\lambda)}{V},$$

where Σ_{cond} designates the quark condensate normalized to a single flavor. To generate a non-zero density $\rho(0)$, the smallest eigenvalues must become densely packed as the volume increases, with an eigenvalue spacing $\Delta\lambda \approx 1/\rho(0) = \pi/(\Sigma_{cond}V)$. This allows a crude estimate of the quark condensate Σ_{cond}. One can do better by exploring the ϵ-regime: If chiral symmetry is spontaneously broken, tune the volume and quark mass such that $\frac{1}{F_\pi} \ll L \ll \frac{1}{M_\pi}$, so that the Goldstone pion is much lighter than the physical value, and finite volume effects are dominant as we discussed in Section 2. The chiral Lagrangian of Eq. (4.2) is dominated by the zero-momentum mode from the mass term and all kinetic terms are suppressed. In this limit, the distributions of the lowest eigenvalues are identical to those of random matrix theory, a theory of large matrices obeying certain symmetries [77, 145, 146]. To connect with RMT, the eigenvalues and quark mass are rescaled as $z = \lambda\Sigma_{cond}V$ and $\mu = m_q\Sigma_{cond}V$, and the eigenvalue distributions also depend on the topological charge ν and the number of quark flavors N_f. RMT is a very useful tool to calculate analytically all of the eigenvalue distributions [147]. The eigenvalue distributions in various topological sectors are measured via lattice simulations, and via comparison with RMT, the value of the condensate Σ_{cond} can be extracted.

After we generate large thermalized ensembles, we calculate the lowest twenty eigenvalues of the Dirac operator using the PRIMME package [84]. In the continuum limit, the staggered eigenvalues form degenerate quartets, with restored taste symmetry. The first column of Fig. 4.7 shows the change in the eigenvalue structure for $N_f = 4$ as the coupling constant is varied. At $\beta = 3.6$ grouping into quartets is not seen, the Goldstone pions are somewhat still split, and staggered perturbation theory is just beginning to kick in. At $\beta = 3.8$ doublet pairing appears and at $\beta = 4.0$ the quartets are nearly degenerate. The Dirac spectrum is collapsed as required by the Banks-Casher relation. In the second column we show

the integrated distributions of the two lowest eigenvalue quartet averages,

$$\int_0^{\lambda} p_k(\lambda')d\lambda', \quad k = 1, 2 \tag{4.12}$$

which is only justified close to quartet degeneracy. All low eigenvalues are selected with zero topology. To compare with RMT, we vary $\mu = m_q \Sigma_{cond} V$ until we satisfy

$$\frac{\langle \lambda_1 \rangle_{\rm sim}}{m} = \frac{\langle z_1 \rangle_{\rm RMT}}{\mu}, \tag{4.13}$$

where $\langle \lambda_1 \rangle_{\rm sim}$ is the lowest quartet average from simulations and the RMT average $\langle z \rangle_{\rm RMT}$ depends implicitly on μ and N_f. With this optimal value of μ, we can predict the shapes of $p_k(\lambda)$ and their integrated distributions, and compare to the simulations. The agreement with the two lowest integrated RMT eigenvalue shapes is excellent for the larger β values.

The main qualitative features of the RMT spectrum are very similar in our $N_f = 8$ simulations as shown in Fig. 4.8. One marked quantitative difference is a noticeable slowdown in response to change in the coupling constant. As β grows the recovery of the quartet degeneracy is considerably delayed in comparison with the onset of p-regime Goldstone dynamics. Overall, for the $N_f = 4, 8$ models we find consistency between the p-regime analysis and the RMT tests. Earlier, using Asqtad fermions at a particular β value, we found agreement with RMT even at $N_f = 12$ which indicated a chirally broken phase [105]. Strong taste breaking with Asqtad fermions leaves the quartet averaging in question and the bulk pronounced crossover of the Asqtad action as β grows is also an issue. Currently we are investigating the RMT picture for $N_f = 9, 10, 11, 12$ with our much improved action with stout smearing. This action shows no artifact transitions and handles taste breaking much more effectively. Firm conclusions on the $N_f = 12$ model to support our findings of χSB in the p-regime will require continued investigations.

4.8 Inside the conformal window

We start our investigation and simulations of the conformal window at $N_f = 16$ which is the most accessible for analytic methods. We are particularly interested

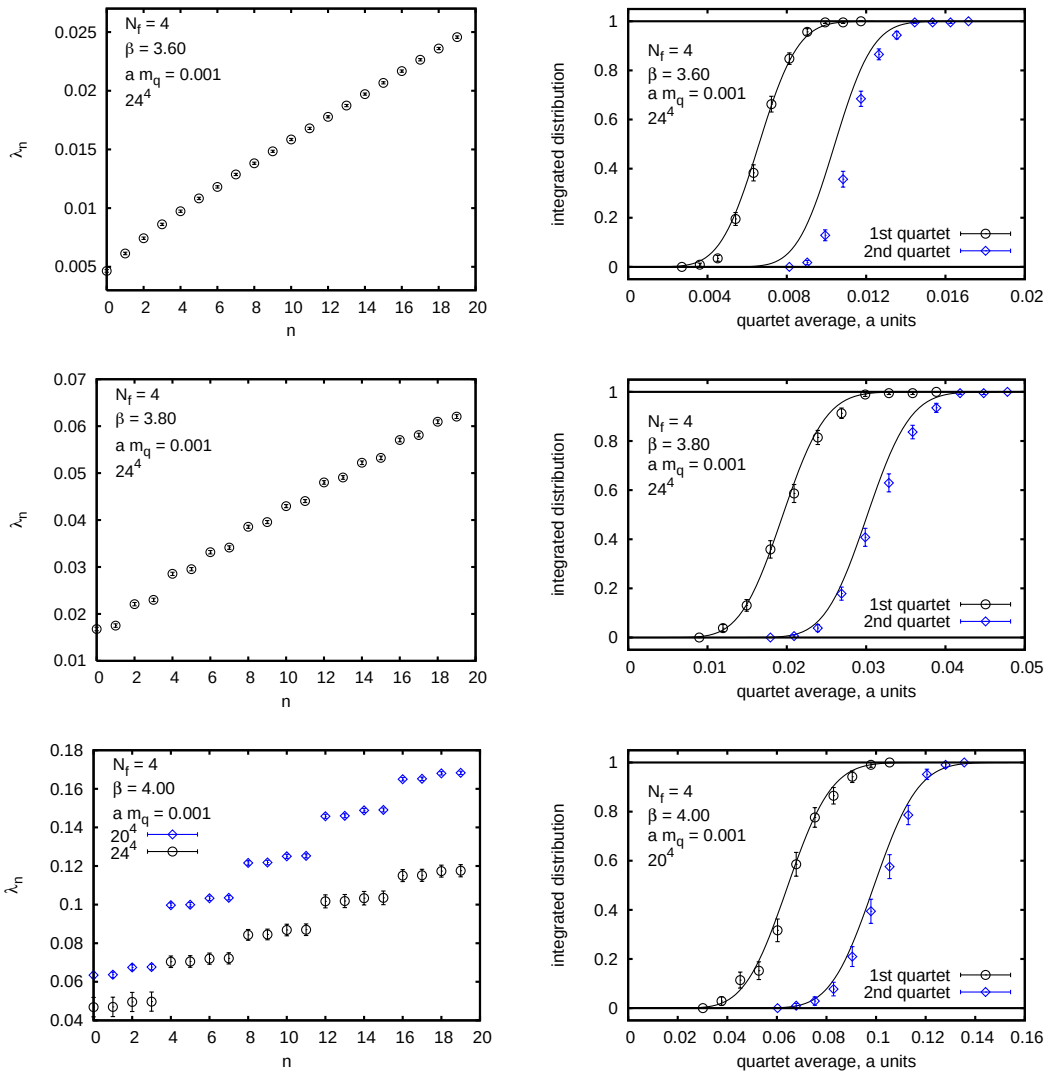

Figure 4.7: From simulations at $N_f = 4$ the first column shows the approach to quartet degeneracy of the spectrum as β increases. The second column shows the integrated distribution of the two lowest quartets averaged. The solid line compares this procedure to RMT with $N_f = 4$.

in the qualitative behavior of the finite volume spectrum of the model and the running coupling with its associated beta function which is expected to have a weak coupling fixed point around $g^{*2} \approx 0.5$, as estimated from the scheme-independent, two-loop beta function [148]. A distinguished feature of the $N_f = 16$ conformal model is how the renormalized coupling $g^2(L)$ runs with L, the linear size of the spatial volume in a Hamiltonian or Transfer Matrix description. On very small

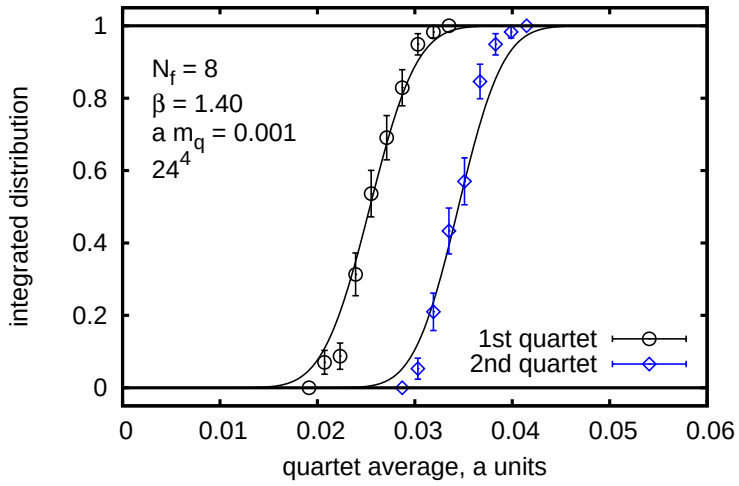

Figure 4.8: The solid lines compare the integrated distribution of the two lowest quartet averages to RMT predictions with $N_f = 8$.

scales the running coupling $g^2(L)$ grows with L as in any other asymptotically free theory. However, $g^2(L)$ will not grow large, and in the $L \to \infty$ limit it will converge to the fixed point g^{*2} which is rather weak, within the reach of perturbation theory. There is non-trivial, small-volume dynamics which is illustrated first in the pure gauge sector.

At small g^2, without fermions, the zero-momentum components of the gauge field are known to dominate the dynamics [149, 150, 151]. With $SU(3)$ gauge group, there are twenty-seven degenerate vacuum states, separated by energy barriers which are generated by the integrated effects of the non-zero momentum components of the gauge field in the Born-Oppenheimer approximation. The lowest-energy excitations of the gauge field Hamiltonian scale as $\sim g^{2/3}(L)/L$ evolving into glueball states and becoming independent of the volume as the coupling constant grows with L. Non-trivial dynamics evolves through three stages as L grows. In the first regime, in very small boxes, tunneling is suppressed between vacua which remain isolated. In the second regime, for larger L, tunneling sets in and electric flux states will not be exponentially suppressed. Both regimes represent small worlds with zero-momentum spectra separated from higher momentum modes of the theory with energies on the scale of $2\pi/L$. At large enough L the gauge dynamics overcomes the energy barrier, and wave functions spread over the vacuum

valley. This third regime is the crossover to confinement where the electric fluxes collapse into thin string states wrapping around the box.

It is likely that a conformal theory with a weak coupling fixed point at $N_f = 16$ will have only the first two regimes which are common with QCD. Now the calculations have to include fermion loops [152, 153]. The vacuum structure in small enough volumes, for which the wave functional is sufficiently localized around the vacuum configuration, remains calculable by adding in one-loop order the quantum effects of the fermion field fluctuations. The spatially constant abelian gauge fields parametrizing the vacuum valley are given by $A_i(\mathbf{x}) = T^a C_i^a/L$ where T_a are the (N-1) generators for the Cartan subalgebra of $SU(N)$. For $SU(3)$, $T_1 = \lambda_3/2$ and $T_2 = \lambda_8/2$. With N_f flavors of massless fermion fields the effective potential of the constant mode is given by

$$V_{\rm eff}^{\mathbf{k}}(\mathbf{C}^b) = \sum_{i>j} V(\mathbf{C}^b[\mu_b^{(i)} - \mu_b^{(j)}]) - N_f \sum_i V(\mathbf{C}^b \mu_b^{(i)} + \pi\mathbf{k}), \qquad (4.14)$$

with $\mathbf{k} = \mathbf{0}$ for periodic, or $\mathbf{k} = (1,1,1)$, for antiperiodic boundary conditions on the fermion fields. The function $V(\mathbf{C})$ is the one-loop effective potential for $N_f = 0$ and the weight vectors $\mu^{(i)}$ are determined by the eigenvalues of the abelian generators. For SU(3) $\mu^{(1)} = (1,1,-2)/\sqrt{12}$ and $\mu^{(2)} = \frac{1}{2}(1,-1,0)$. The correct quantum vacuum is found at the minimum of this effective potential which is dramatically changed by the fermion loop contributions. The Polyakov loop observables remain center elements at the new vacuum configurations with complex values; for $SU(N)$

$$P_j = \frac{1}{N}\,\mathrm{tr}\,\left(\exp(iC_j^b T_b)\right) = \frac{1}{N}\sum_n \exp(i\mu_b^{(n)} C_j^b) = \exp(2\pi i l_j/N). \qquad (4.15)$$

This implies $\mu_b^{(n)}\mathbf{C}^b = 2\pi\mathbf{l}/N \pmod{2\pi}$ and $V_{\rm eff}^{\mathbf{k}} = -N_f N V(2\pi\mathbf{l}/N + \pi\mathbf{k})$. In the case of antiperiodic boundary conditions, $\mathbf{k} = (1,1,1)$, this is minimal only when $\mathbf{l} = \mathbf{0} \pmod{2\pi}$. The quantum vacuum in this case is the naive one, $A = 0$ ($P_j = 1$). In the case of periodic boundary conditions, $\mathbf{k} = \mathbf{0}$, the vacua have $\mathbf{l} \neq \mathbf{0}$, so that P_j correspond to non-trivial center elements. For SU(3), there are now 8 degenerate vacua characterized by eight different Polyakov loops, $P_j = \exp(\pm 2\pi i/3)$. Since they are related by coordinate reflections, in a small volume parity (P) and charge conjugation (C) are spontaneously broken, although CP is still a good symmetry [152].

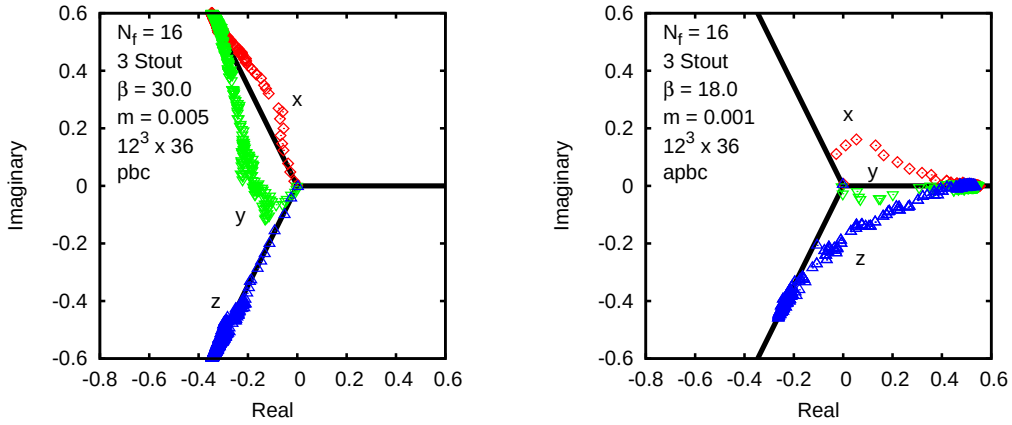

Figure 4.9: The time evolution of complex Polyakov loop distributions are shown from our $N_f = 16$ simulations with $12^3 \times 36$ lattice volume. Tree-level Symanzik-improved gauge action is used in the simulations and staggered fermions with three stout steps and very small fermion masses.

Our simulations of the $N_f = 16$ model below the conformal fixed point g^{*2} confirm the theoretical vacuum structure. Fig. 4.9 shows the time evolution of Polyakov loop distributions monitored along the three separate spatial directions. On the left side, with periodic spatial boundary conditions, the time evolution is shown starting from randomized gauge configuration with the Polyakov loop at the origin. The system evolves into one of the eight degenerate vacua selected by the positive imaginary part of the complex Polyakov loop along the x and y direction and negative imaginary part along the z direction. On the right, with antiperiodic spatial boundary conditions, the vacuum is unique and trivial with real Polyakov loop in all three directions. The time evolution is particularly interesting in the z direction with a swing first from the randomized gauge configuration to a complex metastable minimum first, and eventually tunneling back to the trivial vacuum and staying there, as expected. The measured fermion-antifermion spectra and the spectrum of the Dirac operator further confirm this vacuum structure. Our plans include the continued investigation of zero-mode gauge dynamics which should clarify many important aspects of conformal and nearly conformal gauge theories.

Acknowledgments

We are thankful to Claude Bernard and Steve Sharpe for help with staggered perturbation theory and to Ferenc Niedermayer for discussions on rotator dynamics. We are grateful to Sandor Katz and Kalman Szabo for the Wuppertal RHMC code, and for some calculations, we used the publicly available MILC code. We performed simulations on the Wuppertal GPU cluster, Fermilab clusters under the auspices of USQCD and SciDAC, and the Ranger cluster of the Teragrid organization. This work is supported by the NSF under grant 0704171, by the DOE under grants DOE-FG03-97ER40546, DOE-FG-02-97ER25308, by the DFG under grant FO 502/1 and by SFB-TR/55.

Chapter 4, in full, is currently being prepared for submission for publication in Proceedings of Science: Lattice 2009. The dissertation author was a principal investigator and co-author of this paper.

Bibliography

[1] M. E. Peskin and D. V. Schroeder, *Reading, USA: Addison-Wesley (1995).*

[2] S. F. Novaes, arXiv:hep-ph/0001283.

[3] K. Lane, arXiv:hep-ph/0202255.

[4] S. L. Glashow, Nucl. Phys. **22**, 579 (1961).

[5] L. Susskind, Phys. Rev. D **20**, 2610 (1979).

[6] E. Eichten and K. D. Lane, Phys. Lett. B **90**, 125 (1980).

[7] C. T. Hill, Phys. Lett. B **345**, 483 (1995).

[8] R. Barate *et al.* [LEP Working Group for Higgs boson searches], Phys. Lett. B **565**, 61 (2003).

[9] LEP Electroweak Working Group, `http://lepewwg.web.cern.ch/LEPEWWG/`.

[10] M. S. Chanowitz, Phys. Rev. D **66**, 073002 (2002).

[11] M. E. Peskin and J. D. Wells, Phys. Rev. D **64**, 093003 (2001).

[12] C. Grojean, W. Skiba and J. Terning, Phys. Rev. D **73**, 075008 (2006).

[13] K. Hagiwara *et al.* [Particle Data Group], Phys. Rev. D **66**, 010001 (2002).

[14] T. Hambye and K. Riesselmann, Phys. Rev. D **55**, 7255 (1997).

[15] J. A. Casas, J. R. Espinosa and M. Quiros, Phys. Lett. B **382**, 374 (1996).

[16] K. Holland and J. Kuti, Nucl. Phys. Proc. Suppl. **129**, 765 (2004).

[17] K. Holland, Nucl. Phys. Proc. Suppl. **140**, 155 (2005).

[18] K. Jansen, J. Kuti and C. Liu, Phys. Lett. B **309**, 119 (1993).

[19] K. Jansen, J. Kuti and C. Liu, Phys. Lett. B **309**, 127 (1993).

[20] B. Grinstein, D. O'Connell and M. B. Wise, `arXiv:0704.1845 [hep-ph]`.

[21] S. R. Coleman and E. Weinberg, Phys. Rev. D **7**, 1888 (1973).

[22] J. Kuti and Y. Shen, Phys. Rev. Lett. **60**, 85 (1988).

[23] R. Fukuda and E. Kyriakopoulos, Nucl. Phys. B **85**, 354 (1975).

[24] L. O'Raifeartaigh, A. Wipf and H. Yoneyama, Nucl. Phys. B **271**, 653 (1986).

[25] L. Susskind, Phys. Rev. D **16**, 3031 (1977).

[26] J. B. Kogut and L. Susskind, Phys. Rev. D **11**, 395 (1975).

[27] S. Duane, A. D. Kennedy, B. J. Pendleton and D. Roweth, Phys. Lett. B **195**, 216 (1987).

[28] K. G. Wilson and J. B. Kogut, Phys. Rept. **12**, 75 (1974).

[29] I. V. Krive and A. D. Linde, Nucl. Phys. B **117**, 265 (1976).

[30] A. D. Linde, Phys. Lett. B **70**, 306 (1977).

[31] H. D. Politzer and S. Wolfram, Phys. Lett. B **82**, 242 (1979) [Erratum-ibid. **83B**, 421 (1979)].

[32] N. Cabibbo, L. Maiani, G. Parisi and R. Petronzio, Nucl. Phys. B **158**, 295 (1979).

[33] P. Q. Hung, Phys. Rev. Lett. **42**, 873 (1979).

[34] R. A. Flores and M. Sher, Phys. Rev. D **27**, 1679 (1983).

[35] M. Lindner, Z. Phys. C **31**, 295 (1986).

[36] M. Sher, Phys. Rept. **179**, 273 (1989).

[37] M. Lindner, M. Sher and H. W. Zaglauer, Phys. Lett. B **228**, 139 (1989).

[38] C. Ford, D. R. T. Jones, P. W. Stephenson and M. B. Einhorn, Nucl. Phys. B **395**, 17 (1993).

[39] M. Sher, Phys. Lett. B **317**, 159 (1993) [Addendum-ibid. B **331**, 448 (1994)].

[40] J. A. Casas, J. R. Espinosa and M. Quiros, Phys. Lett. B **342**, 171 (1995).

[41] G. Altarelli and G. Isidori, Phys. Lett. B **337**, 141 (1994).

[42] D. Boyanovsky, W. Loinaz and R. S. Willey, Phys. Rev. D **57**, 100 (1998).

[43] M. B. Einhorn and D. R. T. Jones, JHEP **0704**, 051 (2007).

[44] P. B. Arnold, Phys. Rev. D **40**, 613 (1989).

[45] G. W. Anderson, Phys. Lett. B **243**, 265 (1990).

[46] P. Arnold and S. Vokos, Phys. Rev. D **44**, 3620 (1991).

[47] J. R. Espinosa and M. Quiros, Phys. Lett. B **353**, 257 (1995).

[48] G. Isidori, G. Ridolfi and A. Strumia, Nucl. Phys. B **609**, 387 (2001).

[49] P. Gerhold and K. Jansen, `arXiv:0707.3849 [hep-lat]`.

[50] P. Gerhold and K. Jansen, JHEP **0709**, 041 (2007).

[51] L. Lin, I. Montvay, H. Wittig and G. Munster, Nucl. Phys. B **355**, 511 (1991).

[52] W. Bock, A. K. De, K. Jansen, J. Jersak, T. Neuhaus and J. Smit, Nucl. Phys. B **344**, 207 (1990).

[53] I. H. Lee, J. Shigemitsu and R. E. Shrock, Nucl. Phys. B **334**, 265 (1990).

[54] Z. Fodor, S. D. Katz and K. K. Szabo, JHEP **0408**, 003 (2004).

[55] G. I. Egri, Z. Fodor, C. Hoelbling, S. D. Katz, D. Nogradi and K. K. Szabo, Comput. Phys. Commun. **177**, 631 (2007).

[56] J. Kuti, L. Lin and Y. Shen, Phys. Rev. Lett. **61**, 678 (1988).

[57] M. Luscher and P. Weisz, Phys. Lett. B **212**, 472 (1988).

[58] T. D. Lee and G. C. Wick, Phys. Rev. D **2**, 1033 (1970).

[59] T. D. Lee and G. C. Wick, Nucl. Phys. B **9**, 209 (1969).

[60] J. Kuti, *Unpublished.*

[61] T. D. Bakeyev and A. A. Slavnov, Mod. Phys. Lett. A **11**, 1539 (1996). *(this paper contains relevant earlier references).*

[62] C. Liu, `arXiv:0704.3999 [hep-ph]`.

[63] J. Kuti, Nucl. Phys. Proc. Suppl. **42**, 113 (1995).

[64] C. Liu, K. Jansen and J. Kuti, Nucl. Phys. Proc. Suppl. **42**, 630 (1995).

[65] R. S. Chivukula and E. H. Simmons, Phys. Lett. B **388**, 788 (1996).

[66] R. Barbieri, L. J. Hall and V. S. Rychkov, Phys. Rev. D **74**, 015007 (2006).

[67] S. Weinberg, Phys. Rev. D **19**, 1277 (1979).

[68] L. Susskind, Phys. Rev. D **20**, 2619 (1979).

[69] D. D. Dietrich and F. Sannino, Phys. Rev. D **75**, 085018 (2007).

[70] S. Catterall and F. Sannino, Phys. Rev. D **76**, 034504 (2007).

[71] T. Appelquist, G. T. Fleming and E. T. Neil, Phys. Rev. Lett. **100**, 171607 (2008).

[72] Y. Shamir, B. Svetitsky and T. DeGrand, Phys. Rev. D **78**, 031502 (2008).

[73] A. Deuzeman, M. P. Lombardo and E. Pallante, arXiv:0804.2905 [hep-lat].

[74] L. Del Debbio, A. Patella and C. Pica, arXiv:0805.2058 [hep-lat].

[75] T. Banks and A. Casher, Nucl. Phys. B **169**, 103 (1980).

[76] J. Gasser and H. Leutwyler, Phys. Lett. B **188**, 477 (1987).

[77] E. V. Shuryak and J. J. M. Verbaarschot, Nucl. Phys. A **560**, 306 (1993).

[78] H. Fukaya, S. Aoki, T. W. Chiu, S. Hashimoto, T. Kaneko, H. Matsufuru, J. Noaki, K. Ogawa, T. Onogi, N. Yamada, Phys. Rev. D **76**, 054503 (2007).

[79] Z. Fodor, K. Holland, J. Kuti, D. Nogradi and C. Schroeder, PoS **LAT2008**, 058 (2008).

[80] K. Orginos, D. Toussaint and R. L. Sugar [MILC Collaboration], Phys. Rev. D **60**, 054503 (1999).

[81] C. T. H. Davies *et al.* [HPQCD Collaboration and UKQCD Collaboration and MILC Collaboration and], Phys. Rev. Lett. **92**, 022001 (2004).

[82] E. Follana, A. Hart, C. T. H. Davies and Q. Mason [HPQCD Collaboration and UKQCD Collaboration], Phys. Rev. D **72**, 054501 (2005).

[83] S. A. Gottlieb, W. Liu, D. Toussaint, R. L. Renken and R. L. Sugar, Phys. Rev. D **35**, 2531 (1987).

[84] A. Stathopoulos and J. R. McCombs, SIAM J. Sci. Comput., Vol. **29, No. 5**, 2162 (2007).

[85] P. H. Damgaard, U. M. Heller, R. Niclasen and K. Rummukainen, Phys. Lett. B **495**, 263 (2000).

[86] A. Hasenfratz and F. Knechtli, Phys. Rev. D **64**, 034504 (2001).

[87] C. Morningstar and M. J. Peardon, Phys. Rev. D **69**, 054501 (2004).

[88] E. Follana *et al.* [HPQCD Collaboration and UKQCD Collaboration], Phys. Rev. D **75**, 054502 (2007).

[89] Z. Fodor, K. Holland, J. Kuti, D. Nogradi and C. Schroeder, Phys. Lett. B **681**, 353 (2009).

[90] Z. Fodor, K. Holland, J. Kuti, D. Nogradi and C. Schroeder, paper in preparation.

[91] E. Farhi and L. Susskind, Phys. Rept. **74**, 277 (1981).

[92] F. Sannino, arXiv:0902.3494 [hep-ph].

[93] T. A. Ryttov and F. Sannino, Phys. Rev. D **76**, 105004 (2007).

[94] D. K. Hong, S. D. H. Hsu and F. Sannino, Phys. Lett. B **597**, 89 (2004).

[95] W. E. Caswell, Phys. Rev. Lett. **33**, 244 (1974).

[96] T. Banks and A. Zaks, Nucl. Phys. B **196**, 189 (1982).

[97] T. Appelquist, K. D. Lane and U. Mahanta, Phys. Rev. Lett. **61**, 1553 (1988).

[98] A. G. Cohen and H. Georgi, Nucl. Phys. B **314**, 7 (1989).

[99] T. Appelquist, J. Terning and L. C. R. Wijewardhana, Phys. Rev. Lett. **77**, 1214 (1996).

[100] B. Holdom, Phys. Rev. D **24**, 1441 (1981).

[101] K. Yamawaki, M. Bando and K. I. Matumoto, Phys. Rev. Lett. **56**, 1335 (1986).

[102] T. W. Appelquist, D. Karabali and L. C. R. Wijewardhana, Phys. Rev. Lett. **57**, 957 (1986).

[103] V. A. Miransky and K. Yamawaki, Phys. Rev. D **55**, 5051 (1997).

[104] M. Kurachi and R. Shrock, JHEP **0612**, 034 (2006).

[105] Z. Fodor, K. Holland, J. Kuti, D. Nogradi and C. Schroeder, PoS **LATTICE2008**, 066 (2008).

[106] Z. Fodor, K. Holland, J. Kuti, D. Nogradi and C. Schroeder, PoS **LATTICE2008**, 058 (2008).

[107] Z. Fodor, K. Holland, J. Kuti, D. Nogradi and C. Schroeder, arXiv:0905.3586 [hep-lat].

[108] T. DeGrand, Y. Shamir and B. Svetitsky, Phys. Rev. D **79**, 034501 (2009).

[109] T. DeGrand, Y. Shamir and B. Svetitsky, arXiv:0809.2953 [hep-lat].

[110] B. Svetitsky, Y. Shamir and T. DeGrand, arXiv:0809.2885 [hep-lat].

[111] T. Appelquist, G. T. Fleming and E. T. Neil, arXiv:0901.3766 [hep-ph].

[112] G. T. Fleming, PoS **LATTICE2008**, 021 (2008).

[113] L. Del Debbio, A. Patella and C. Pica, arXiv:0812.0570 [hep-lat].

[114] L. Del Debbio, M. T. Frandsen, H. Panagopoulos and F. Sannino, JHEP **0806**, 007 (2008).

[115] A. J. Hietanen, K. Rummukainen and K. Tuominen, arXiv:0904.0864 [hep-lat].

[116] A. J. Hietanen, J. Rantaharju, K. Rummukainen and K. Tuominen, arXiv:0812.1467 [hep-lat].

[117] A. Hietanen, J. Rantaharju, K. Rummukainen and K. Tuominen, PoS **LATTICE2008**, 065 (2008).

[118] A. Deuzeman, M. P. Lombardo and E. Pallante, arXiv:0904.4662 [hep-ph].

[119] A. Deuzeman, M. P. Lombardo and E. Pallante, arXiv:0810.3117 [hep-lat].

[120] A. Deuzeman, M. P. Lombardo and E. Pallante, PoS **LATTICE2008**, 060 (2008).

[121] S. Catterall, J. Giedt, F. Sannino and J. Schneible, JHEP **0811**, 009 (2008).

[122] X. Y. Jin and R. D. Mawhinney, PoS **LATTICE2008**, 059 (2008).

[123] A. Hasenfratz, arXiv:0907.0919 [hep-lat].

[124] T. DeGrand and A. Hasenfratz, arXiv:0906.1976 [hep-lat].

[125] T. DeGrand, arXiv:0906.4543 [hep-lat].

[126] L. Del Debbio, B. Lucini, A. Patella, C. Pica and A. Rago, arXiv:0907.3896 [hep-lat].

[127] T. DeGrand, arXiv:0910.3072 [hep-lat].

[128] T. Appelquist *et al.* [LSD Collaboration], arXiv:0910.2224 [hep-ph].

[129] X. Y. Jin and R. D. Mawhinney, PoS **LAT2009**, 049 (2009).

[130] A. Hasenfratz, arXiv:0911.0646 [hep-lat].

[131] D. K. Sinclair and J. B. Kogut, arXiv:0909.2019 [hep-lat].

[132] Y. Aoki, Z. Fodor, S. D. Katz and K. K. Szabo, JHEP **0601**, 089 (2006); Phys. Lett. B **643**, 46 (2006).

[133] W. J. Lee and S. R. Sharpe, Phys. Rev. D **60**, 114503 (1999).

[134] C. Aubin and C. Bernard, Phys. Rev. D **68**, 034014 (2003).

[135] C. Aubin and C. Bernard, Phys. Rev. D **68**, 074011 (2003).

[136] J. Gasser and H. Leutwyler, Nucl. Phys. B **307**, 763 (1988).

[137] F. C. Hansen and H. Leutwyler, Nucl. Phys. B **350**, 201 (1991).

[138] J. Gasser and H. Leutwyler, Annals Phys. **158**, 142 (1984).

[139] M. Gell-Mann, R. J. Oakes and B. Renner, Phys. Rev. **175**, 2195 (1968).

[140] J. Bijnens and J. Lu, arXiv:0910.5424 [hep-ph].

[141] H. Leutwyler, Phys. Lett. B **189**, 197 (1987).

[142] J. Noaki *et al.* [JLQCD and TWQCD Collaborations], Phys. Rev. Lett. **101**, 202004 (2008).

[143] P. Hasenfratz and F. Niedermayer, Z. Phys. B **92**, 91 (1993), arXiv:hep-lat/9212022.

[144] P. Hasenfratz, arXiv:0909.3419 [hep-th].

[145] P. H. Damgaard, Nucl. Phys. Proc. Suppl. **128**, 47 (2004).

[146] J. J. M. Verbaarschot and T. Wettig, Ann. Rev. Nucl. Part. Sci. **50**, 343 (2000).

[147] P. H. Damgaard and S. M. Nishigaki, Phys. Rev. D **63**, 045012 (2001).

[148] U. M. Heller, Nucl. Phys. Proc. Suppl. **63**, 248 (1998).

[149] G. 't Hooft, Nucl. Phys. B **153**, 141 (1979).

[150] M. Luscher, Nucl. Phys. B **219**, 233 (1983).

[151] P. van Baal and J. Koller, Annals Phys. **174**, 299 (1987).

[152] P. van Baal, Nucl. Phys. B **307**, 274 (1988).

[153] J. Kripfganz and C. Michael, Nucl. Phys. B **314**, 25 (1989).